Impurity transport in plasma fusion and its impact over the global confinement

Kyungtak Lim

To cite this version:

Kyungtak Lim. Impurity transport in plasma fusion and its impact over the global confinement. Plasma Physics [physics.plasm-ph]. Université de Lorraine, 2021. English. NNT : 2021LORR0186 . tel-03632878

HAL Id: tel-03632878
https://hal.univ-lorraine.fr/tel-03632878

Submitted on 6 Apr 2022

Transport d'impuretés dans les plasmas de fusion et impact sur le confinement global

THÈSE

présentée et soutenue publiquement le 29 septembre 2021

pour l'obtention du titre de

Docteur de l'Université de Lorraine

Spécialité : Physique des plasmas

par

Kyungtak Lim

Composition du jury

Rapporteurs :	M. Yann Camenen	Chargé de recherches CNRS - HDR, PIIM, Aix-Marseille Université
	M. Clemente Angioni	Senior scientist, Max Planck Institute for Plasma Physics
Examinateurs :	M. Eric Serre	Directeur de recherches CNRS, M2P2, Aix-Marseille Université
	M. Xavier Garbet	Directeur de recherches CEA, IRFM - CEA Cadarache
	Mme. Laure Vermare	Chargé de recherches CNRS – HDR, LPP, Ecole polytechnique
	M. Thierry Belmonte	Directeur de recherches CNRS, IJL, Université de Lorraine
Directeur:	M. Etienne Gravier	Professeur des Universités, IJL, Université de Lorraine
Co-directeur :	M. Maxime Lesur	Maître de conférences HDR, IJL, Université de Lorraine

Institut Jean Lamour | UMR CNRS 7198, Nancy, France
Université de Lorraine

Sommaire

Acknowledgement

The work discussed in this manuscript is the result of my three years of a PhD program, during which I have had an opportunity to meet a lot of people who made me personally and professionally a better person. Without them, this work would have been incomplete, and for this, I would like to express my sincere gratitude.

First of all, I am deeply indebted to my supervisors Etienne and Maxime, without whom this work would not have been possible. Their thoughtfulness and support helped me enormously when I got discouraged about not being productive enough. By watching them, I learned what it really means to become a good mentor and it was a great pleasure to have worked with them during the past three years. I also deeply appreciate their guidance and careful revision of all my manuscripts and their trust in me, which encouraged me to get through this journey.

I am also very thankful to Virginie, Yanick, and Xavier, who accompanied me through my PhD course. Having a regular video meeting with them was a huge motivation and it always ended up with a fruitful discussion and constructive advice for my work. Thank you for sharing your knowledge and your expertise. It was a great honor and a privilege to have worked with you.

I would like to thank also all the other current and former colleagues of the group *plasma chauds* in IJL. Alejandro, Anil, Daniele, Dimitri, Erwan, Frédéric, Guillaume, Homam, Jérôme, Julien, Liliane, Luigi, Sarah, Stéphane, Thierry and all the others, with whom I shared many unforgettable moments. Thank you also for my friends whom I met outside my office. Spending time with you made me forget about physics for a moment and gave me a lot of energy to get back to work again.

A special thank goes to Marie for being with me during all these years, for having listened to all my complaints. I cannot even imagine where I would be without you. I often saw the world as black and white, but you were the color to me. The only color that I had.

Finally, I would like to thank my mom and sister who have supported me during my entire studies on the other side of the world. Especially, to my father, who sacrificed everything for our family. As you know, I am not good at expressing my innermost thoughts to you, but just remember that I am so proud of being your son and having a father like you. You mean a lot to me.

Résumé

L'énergie des étoiles, et du Soleil en particulier, provient de la fusion nucléaire. Au centre du Soleil, la température atteint 15 millions de degrés. À une telle température, les électrons se libèrent des noyaux, générant un plasma. Le comportement du plasma est particulièrement complexe puisque chaque particule est influencée par des interactions à longue portée avec toutes les autres particules. La physique des plasmas cherche à décrire l'évolution et le comportement de tels systèmes.

Au cours de la réaction de fusion entre les noyaux de deutérium et tritium, de l'énergie est libérée, de l'ordre de plusieurs MeV, sous forme d'énergie cinétique des noyaux formés (hélium, appelé également particule alpha, et neutron, voir Figure 1).

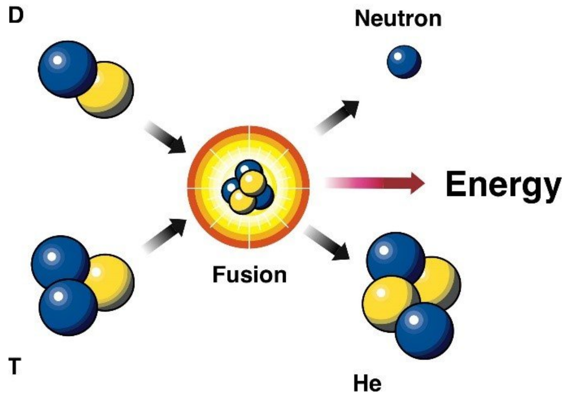

FIGURE 1 – Représentation de la réaction de fusion du deutérium (D) et du tritium (T), qui produit un noyau d'hélium (ou particule alpha) et un neutron de haute énergie [1].

Alors qu'un champ gravitationnel puissant fournit les conditions idéales pour que la fusion se produise dans le Soleil, une température et une gravité insuffisantes rendent difficile la réalisation de la fusion nucléaire sur Terre. Il faut donc trouver une autre méthode. L'application d'un champ magnétique a été proposée pour confiner le plasma, car un champ magnétique peut retenir les particules chargées pour les faire tourner hélicoïdalement autour des lignes de champ. Le rayon de cette hélice est appelé *rayon*

---

[1] https://www.energy.gov/science/doe-explainsnuclear-fusion-reactions

de Larmor. Si l'on parvient à concevoir une ligne de champ magnétique fermée en forme de tore, elle peut alors empêcher un plasma chaud de heurter la paroi. C'est dans les années 1960 que le réacteur à fusion magnétique, *tokamak*, est apparu. Actuellement, le tokamak ITER, qui sera le plus grand tokamak au monde, est en construction sur le site de Cadarache (Figure 2).

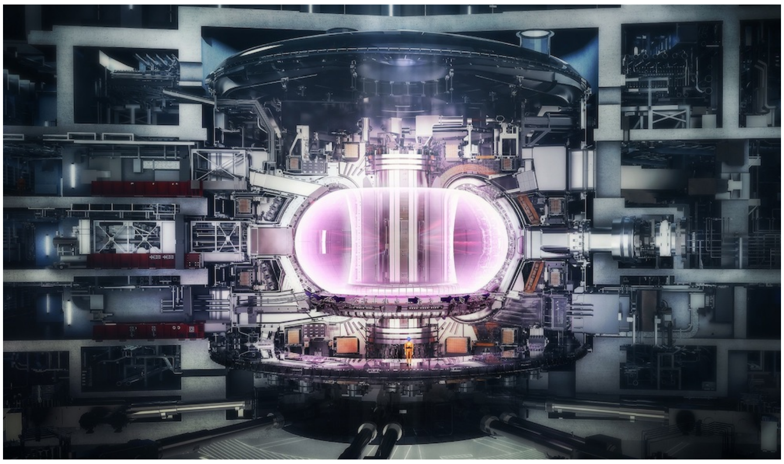

FIGURE 2 – Le tokamak ITER[2].

Dans la fusion nucléaire, la présence inévitable d'impuretés est étroitement liée à la réaction de fusion elle-même et à la présence de parois. Une compréhension approfondie du transport des impuretés est cruciale pour la réalisation du projet ITER. Au cours d'une décharge de plasma, diverses impuretés peuvent être présentes simultanément, par exemple, de l'hélium (He) en tant que réactif des réactions de fusion Deutérium (D)-Tritium (T), de l'argon (Ar) ou de l'azote (Ni) qui peuvent être injectés volontairement pour réduire le flux de chaleur sur le divertor, et des impuretés - carbone (C) et tungstène (W) - provenant des interactions plasma-paroi. Il a été montré par exemple, (i) que l'accumulation d'impuretés lourdes dans le coeur du plasma peut entraîner une chute des performances du réacteur en rayonnant l'énergie (ii) que l'augmentation d'impuretés légères dans le tokamak peut diluer le combustible principale DT.

Il existe trois mécanismes différents par lesquels le transport d'impuretés est généré : (i) la turbulence, (ii) les effets de collisions (transport néoclassique), et (iii) les instabilités MHD. Au cours de cette thèse, nous nous sommes limités au cas électrostatique, ainsi seuls les deux premiers mécanismes ont été étudiés numériquement et théoriquement.

Pour cela, deux codes gyrocinétiques—(i) GYSELA-5D développé au CEA-IRFM et (ii) TERESA-4D développé à l'IJL—ont été utilisés pour étudier le transport des impuretés. La théorie gyrocinétique repose sur l'élimination du mouvement rapide de gy-

---

[2] https://www.iter.org/

ration autour des lignes de champ pour réduire la dimension du modèle. Les équations gyrocinétiques décrivant la dynamique de la fonction distribution des centres-guides peuvent alors être résolues à l'aide de codes numériques complexes. Pourtant, malgré cette réduction, résoudre l'équation 5D dans une simulation non-linéaire avec de multiples espèces (ions, electrons, impuretés) reste très coûteux (par exemple, une simulation bien résolue a besoin de 3 millions d'heures de calcul). Pour cette raison, le code gyrocinétique TERESA a également été utilisé pour compléter les études. C'est un modèle réduit de GYSELA qui ne prend en compte qu'une réponse adiabatique des particules passantes et seule la dynamique des particules piégées est prise en compte. Cette dernière hypothèse permet en effet de réduire la dimension du problème 6D à 4D en réalisant une moyenne supplémentaire sur le rebond des particules piégées. La fonction de distribution est alors celle des centres-bananes. Il est donc possible d'étudier de manière approfondie les phénomènes liés aux particules piégées avec un temps de calcul beaucoup moins important.

a) Le transport turbulent convectif

Le transport turbulent des impuretés peut être divisé en deux parties : une partie diffusive et une partie convective. En général, dans les tokamaks, la partie diffusive conduit à un transport d'impuretés vers l'extérieur (vers les parois). À l'inverse, la partie convective, en fonction de la nature de la turbulence et du profil de la courbure magnétique, peut être dirigée vers l'intérieur et conduire à l'accumulation des impuretés au cœur du plasma. Une étude détaillée de la partie convective peut être réalisée grâce aux dépendances paramétriques de chaque terme, par exemple des termes dits de thermo-diffusion et de pincement de courbure. Dans ce but, le code gyrocinétique TERESA a été utilisé dans le cas d'une turbulence liée aux particules piégées, et une approche analytique, la théorie quasi-linéaire, a été comparée aux résultats numériques, donnant un bon accord qualitatif. Il a été constaté que le pincement de thermo-diffusion est dirigé vers l'intérieur lorsque la turbulence à mode d'électrons piégés (TEM) est dominante. De plus, un signe négatif du pincement de courbure a été constaté dans le cas d'un cisaillement magnétique négatif. Les résultats globaux obtenus à l'aide de TERESA suggèrent, tout d'abord, qu'une utilisation appropriée d'un système de chauffage, tel que l'ICRH, pourrait privilégier une turbulence ITG plutôt que TEM afin d'expulser les impuretés du cœur vers l'extérieur, et également que la formation d'un cisaillement magnétique négatif près de l'axe magnétique pourrait être bénéfique pour empêcher l'accumulation d'impuretés au cœur des tokamaks.

b) La modélisation gyrocinétique des impuretés légères à lourdes en relation avec l'asymétrie poloïdale

Le principal mécanisme de transport des diverses impuretés diffère d'une espèce à l'autre en fonction de leur masse et de leur charge. Pour les impuretés légères, comme l'hélium (He), les particules sont transportées principalement par la turbulence alors que le transport des impuretés lourdes, comme le tungstène (W), est souvent dominé par des effets néoclassiques. Le code gyrocinétique GYSELA, implémenté avec un opérateur de collision linéarisé, nous permet d'étudier le transport turbulent et néoclassique des impuretés de manière complète, en incluant les couplages entre les deux mécanismes. Les simulations non-linéaires réalisées dans ce manuscrit ont confirmé que GYSELA reproduit un fort flux turbulent pour l'hélium alors que le tungstène est principalement dominé par le flux néoclassique, ce qui correspond bien à nos prédictions analytiques. Récemment, il a été montré que l'asymétrie poloïdale de la densité des impuretés peut modifier substantiellement le transport néoclassique des impuretés. En l'absence de systèmes de chauffage externes, l'asymétrie poloïdale est principalement due à la turbulence. L'asymétrie poloïdale générée par la turbulence s'est avérée plus forte pour les impuretés lourdes, ce qui conduit à une forte modification du transport néoclassique, notamment dans le régime de Pfirsch-Schlüter (PS). Les résultats globaux sont en bon accord avec nos descriptions analytiques, nous permettant de retrouver le coefficient du facteur d'écran thermique $H_{\mathrm{GYS}} \sim -0.5$ proche de la prédiction théorique.

c) Les effets de la rotation toroïdale sur le transport d'impuretés

La rotation toroïdale du plasma est un mécanisme qui peut accentuer l'asymétrie poloïdale de la densité des impuretés. Pendant la décharge du tokamak, la rotation toroïdale peut être générée de manière intrinsèque ou externe par le chauffage par injection de faisceau neutre (NBI). La force centrifuge, en relation avec la rotation toroïdale, pousse les impuretés lourdes vers l'extérieur du tore, générant une forte asymétrie poloïdale *'in-out'*. D'un point de vue analytique, cette forte asymétrie poloïdale peut augmenter ou réduire le transport néoclassique d'un ordre de grandeur et même changer sa direction. Dans le cadre de simulations gyrocinétiques non-linéaires réalisées avec GYSELA, des termes sources ajustables ont été appliqués pour étudier les effets d'une forte rotation toroïdale. Les simulations non-linéaires réalisées avec une source de quantité de mouvement toroïdale supplémentaire ont montré que, dans le cas d'une forte rotation, le flux néoclassique vers le coeur a tendance à augmenter en raison d'une asymétrie poloïdale accrue, tandis que le flux turbulent est fortement affecté par la roto-diffusion, ce qui conduit à un flux vers l'extérieur dans le cas d'une turbulence à gradient de température ionique (ITG). Ce terme, proportionnel à A/Z où A, Z sont respectivement la masse et la charge de l'impureté, devient dominant surtout pour les impuretés lourdes.

Dans ce manuscrit, nous avons étudié le transport turbulent et néoclassique des impuretés dans différentes configurations. Les résultats globaux obtenus tout au long de ce manuscrit impliquent que les impuretés lourdes ont tendance à s'accumuler dans la région centrale et sont très sensibles aux conditions externes. Heureusement, il semble qu'une utilisation appropriée d'un système de chauffage par résonance cyclotronique ionique (ICRH) peut atténuer l'accumulation de tungstène au cœur en réduisant l'asymétrie poloïdale et en augmentant le flux turbulent vers l'extérieur. Il pourra être intéressant à l'avenir de prendre en compte le système de chauffage ICRH dans les simulations GYSELA.

Bien que les connaissances actuelles sur le transport des impuretés soient comparables à celles des ions principaux (deutérium et tritium), il reste encore beaucoup de questions ouvertes. Par exemple, dans le cadre de GYSELA, les effets du système de chauffage de l'ICRH, des électrons cinétiques et du transport d'impuretés dans un tokamak à géométrie allongée semblent pouvoir être étudiés dans un avenir relativement proche. D'autre part, l'étude du transport d'impuretés à travers une barrière de transport (piédestal, fort gradient) est en cours à l'aide de GYSELA (thèse de G. Lo-Cascio). Il est pour l'instant impossible pour un code premier principe de prendre en compte tous les processus physiques impliqués dans un plasma de tokamak, tels que le transport dans le plasma de cœur, la physique du plasma de bord, la stabilité MHD, les chauffages externes et la génération du courant. C'est pour cette raison qu'une modélisation intégrée tenant compte de modèles réduits établis grâce aux résultats donnés par les codes "premier principe" de type GYSELA, sera essentielle pour une prédiction fiable des performances des tokamaks.

Chapitre 1

Introduction

Contents

Fossil fuels started to fit into the scheme of human history since the industrialization in the 1800s, and might end up in less than 100 years from now due to the depletion of available resources. Excessive usage of fossil fuels causes a steady increase in greenhouse gases, which is believed to be responsible for the rise of global average temperature. In the report of Intergovernmental Panel on Climate Change (IPCC) (IPCC, 2007), one of the scenarios predicts a doubling of CO_2 emissions and an increase of global temperature about 3-4°C by 2100 (Figure 1.1).

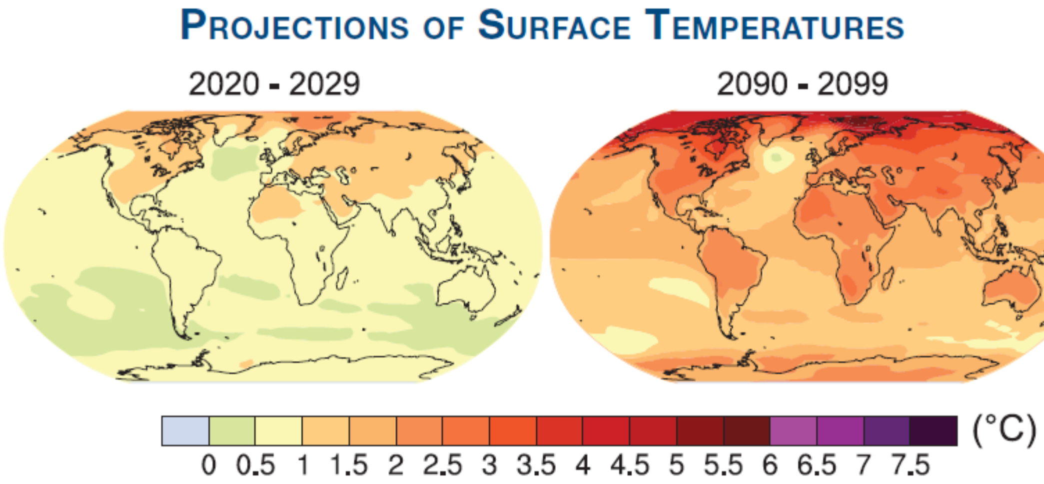

FIGURE 1.1 – Projected surface temperature changes for the early and late 21st century relative to the period 1980-1999 (IPCC, 2007).

It is an undeniable fact that global warming is *anthropogenic*, which means originating in human activity, and we are currently living in the transition era for energy application from fossil fuels to renewable energy. However, although they can be replenished, known forms of renewable energy (e.g., wind, solar, hydro) will not be enough to sustain our living standards. An alternative solution, therefore, is necessary to replace the primary source and to mitigate upcoming climate change in the lifetimes of our children and grandchildren.

Two energy sources can fulfill the requirements of sustainable energy : (i) *Nuclear fission* by splitting large nuclei into smaller ones, and (ii) *Nuclear fusion* by combining small nuclei into larger ones. Of these, nuclear fusion has been considered as the prospective green and safe energy.

1.1 Nuclear fusion : basic concepts

Nuclear fusion is the way the Sun and stars generate their energy. In the center of the Sun, the expected temperature amounts to 15 million degrees. At such temperature, electrons are in some sense detached from nuclei, forming a cloud of charged ions and electrons, the *plasma*. The behavior of plasma is extremely complicated since each particle is influenced by long-range interactions with other particles, and a new area of physics, namely *plasma physics*, was born from the effort to understand such behavior.

For fusion to occur, light nuclei must possess sufficient kinetic energy to overcome the electrostatic repulsion, the *Coulomb barrier*. In the case of deuterium ions, the necessary energy to overcome this barrier amounts to $0.4\mathrm{MeV}(\sim 4.6 \times 10^9\mathrm{K})$. However, such extreme temperature is not necessary due to *quantum tunneling effect* and significant rates of fusion can be achieved even within the tens-of-keV range.

During the fusion reaction, energy is released when light elements are transformed into heavy elements which have higher *binding energy*[3]. As a result, more tightly bounded nuclei emerge and the corresponding mass defect is transformed into tremendous energy, which is the order of MeV. If fusion starts with a light nucleus like hydrogen, two nuclei have to be fused to produce a higher atomic number element moving from left to right on Figure 1.2 while fission goes from right to left with a heavy nucleus being separated into a lighter element.

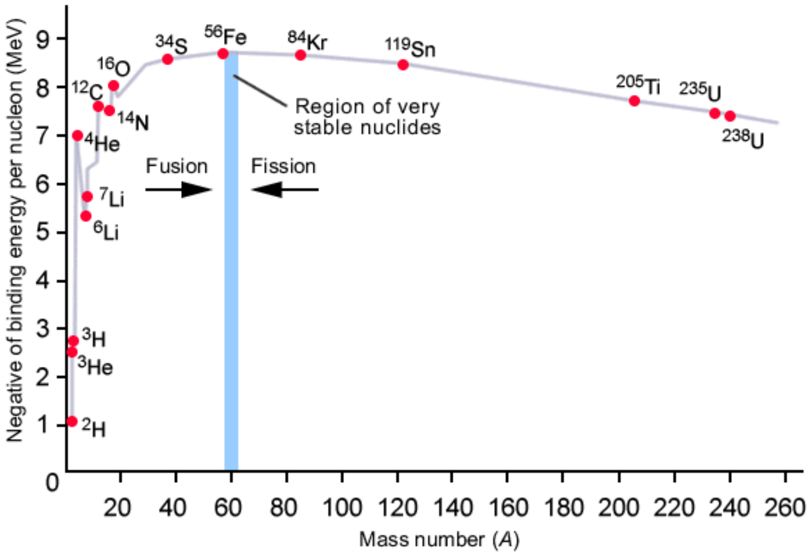

FIGURE 1.2 – The relationship between the nuclear binding energy of an isotope and its atomic mass. Taken from (https://www.dlt.ncssm.edu/tiger/).

The most accessible nuclear fusion happens by combining the hydrogen isotopes—deuterium (D) and tritium (T) —producing helium and a neutron. The neutron carries 80% of re-

---

[3] The atomic nucleus is composed of protons and neutrons. When these elements are assembled together, a nuclear force holds them together. This force is associated with a *binding energy* and this binding energy varies from element to element.

leased energy and it has to be captured in order to convert its energy into heat to run a power plant.

$$^2_1\mathrm{D} + ^3_1\mathrm{T} \longrightarrow ^4_2\mathrm{He}\,(3.5\,\mathrm{MeV}) + n\,(14.1\,\mathrm{MeV}) \tag{1.1}$$

For this reaction, the fuel is a mix of deuterium and tritium. There is 5×10^{16} kg deuterium in the oceans and if we consider the usual quantity consumed in reactors (around 100 kg per reactor per year), these will last for the foreseeable future. While an ample supply of deuterium can be extracted from the oceans, the total storage of tritium is relatively scarce, estimated at around 50 kg. A 1000 MW plant is expected to burn out 250 g of tritium daily, thus an alternative to breed tritium fuel is a paramount priority (Tanabe, 2017).

There is no material that can withstand temperatures of millions of degrees. While a strong gravitational field provides ideal conditions for fusion to occur in the sun, on Earth, an alternative method is necessary to shape the plasma and eventually confine it. Applying a magnetic field has been proposed to confine plasma. Indeed, a magnetic field can hold plasma particles in tight circular orbits around the magnetic field lines, called *Larmor orbits*, preventing them from moving across the magnetic field.

1.2 Magnetic confinement : Tokamaks

In order to obtain a closed set of magnetic field lines, a torus-shaped machine called *tokamak* was invented by a group of Soviet scientists. In a confined plasma, A toroidal surface covered by a contours of constant pressure is called *flux surface* which implies the magnetic field lines must lie on this surface (Figure 1.3). It is instructive to analyse the global geometry of the magnetic field since important issues, such as stability, transport, and particle trajectory, depend on it.

1.2.1 Magnetic field configuration

The general form of the magnetic field in an axisymmetric tokamak $\boldsymbol{B}$ can be expressed as (Hazeltine and Meiss, 2013)

$$\boldsymbol{B} = \boldsymbol{B}_\varphi \hat{e}_\varphi + B_\theta \hat{e}_\theta = I(\psi)\nabla\varphi + \nabla\varphi \times \nabla\psi \tag{1.2}$$

where ψ is the opposite of the poloidal magnetic flux, which is a label of flux surface, $I(\psi)$ is a flux label measuring the toroidal field and φ is the toroidal angle (Figure 1.3).

Some useful relations can be derived from Eq.(1.2) by using vectorial relations, which will be used extensively in this manuscript :

$$\frac{\boldsymbol{B} \times \nabla\psi}{B^2} = \frac{I}{B}\boldsymbol{b} - R\hat{\varphi} \tag{1.3}$$

$$\boldsymbol{B} \times R^2\nabla\varphi = \nabla\psi \tag{1.4}$$

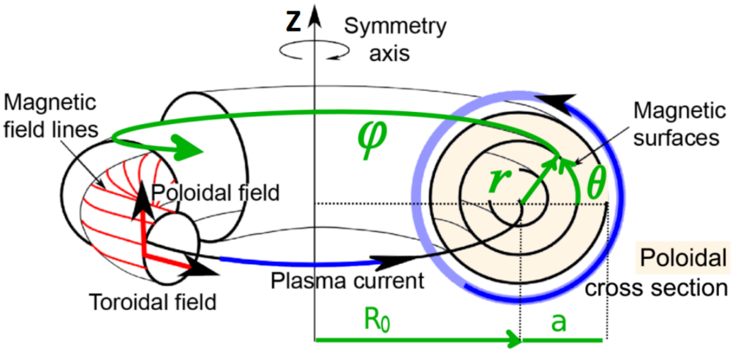

FIGURE 1.3 – The tokamak magnetic configuration and the toroidal coordinate system (r, θ, φ) (Grandgirard, 2016).

where we used the unit vector in the toroidal direction $\hat{\varphi} = R\nabla\varphi$ and $R^2B^2 = I^2 + |\nabla\psi|^2$.

Another very useful notation is the *flux surface average* (Helander and Sigmar, 2005). When a quantity is given $Q(\psi, \theta)$, its flux surface average $\langle Q \rangle$ is the volume average of Q between two neighbouring flux surfaces ψ and $\psi + d\psi$.

$$\langle Q \rangle(\psi) = \int Q(\psi, \theta) dV \Big/ \int dV = \int \frac{Q(\psi, \theta)}{\boldsymbol{B} \cdot \nabla\theta} d\theta \Big/ \int \frac{d\theta}{\boldsymbol{B} \cdot \nabla\theta} \tag{1.5}$$

and the volume element is defined as

$$dV = g^{1/2} d\theta d\varphi = d\theta d\varphi / |(\nabla\varphi \times \nabla\psi) \cdot \nabla\theta| \tag{1.6}$$

where $g^{1/2} = 1/|(\nabla\varphi \times \nabla\psi) \cdot \nabla\theta| = 1/|\boldsymbol{B} \cdot \nabla\theta|$ is the Jacobian [4].

Note that the flux surface average annihilates the operator $\boldsymbol{B} \cdot \nabla = g^{-1/2} \frac{\partial}{\partial\theta}$.

$$\langle \boldsymbol{B} \cdot \nabla Q(\psi, \theta) \rangle = 0 \tag{1.7}$$

Using the flux surface average, it is possible to introduce the *safety factor* as the average change in φ relative to the average change in θ along the magnetic field.

$$q(\psi) = \left\langle \frac{\boldsymbol{B} \cdot \nabla\varphi}{\boldsymbol{B} \cdot \nabla\theta} \right\rangle \tag{1.8}$$

In general, the value of q is usually larger than unity for stability reasons.

---

[4] When we switch to a new coordinate basis, also known as substitution of variables, we stretch things out by different amounts in different directions. The extent of this stretching is called the Jacobian. We use it so that when we integrate over our new coordinates, we can correct for the stretching and find the actual area from our old coordinates.

1.2.2 Circulating & trapped particles

In general, the magnetic field in tokamaks is composed of toroidal and poloidal magnetic fields respectively. A field line forms a helix wound on a toroidal surface. In a strong, axisymmetric magnetic field, the equilibrium motion of a charged particle can be characterized by three constants of motion (Noether, 1971).

$$\begin{aligned} E &= \frac{1}{2}mv_{\parallel}^2 + \mu B + e\phi_{eq} \\ \mu &= \frac{mv_{\perp}^2}{2B} \\ P_{\varphi} &= mRv_{\varphi} - Ze\psi \end{aligned} \tag{1.9}$$

where μ is the magnetic moment and P_{φ} is the toroidal canonical momentum.

Since the background magnetic field is spatially inhomogeneous (stronger near the vertical axis of the tokamak), particles undergo poloidal variations of the magnetic field while flowing along the field lines. As the magnetic field B changes in the particle frame, $v_{\perp}$ varies to conserve the magnetic moment μ, thus $v_{\parallel}$ changes accordingly to conserve energy. Due to this effect, particles are separated into '*passing*' and '*trapped*' particles. From the energy conservation Eq.(1.9), the parallel velocity of particles can be written

$$v_{\parallel} = \pm\sqrt{\frac{2}{m}(E - \mu B)} \tag{1.10}$$

When $E > \mu_s B$, the parallel velocity has always positive sign even in the strong magnetic field B_{max}, completing its orbit without any interruption. However, when $E < \mu_s B$, the parallel velocity approaches to zero and at a certain point $(\theta = \theta_b)$ particles bounce back. Since the energy is conserved regardless of angle $E|_{\theta=0} = E|_{\theta=\theta_b}$, it is possible to express $B = B_b|_{\theta=\theta_b}$ as follows :

$$B_b = B_{\text{min}(\theta=0)}\left(1 + \frac{v_{\parallel}^2}{v_{\perp}^2}\right) \tag{1.11}$$

Knowing that in the limit of circular concentric surfaces, the magnetic field is equal to

$$B(r,\theta) = \frac{B_0}{1 + \epsilon\cos\theta} \tag{1.12}$$

where B_0 denotes the field amplitude at the magnetic axis and $\epsilon = r/R_0$.

It is clear that the magnetic field for a bouncing point B_b must be smaller than B_{max} and this relation gives the trapping condition which separates each species into passing and trapped populations (Figure 1.4).

$$\frac{v_{\parallel}}{v_{\perp}} \simeq \sqrt{2\epsilon} \tag{1.13}$$

The trapped population, with insufficient parallel velocity to overcome the strong magnetic field, is confined to the low-field side with banana-shaped orbits and experiences toroidal precession, which is the average drift motion of the particles in the toroidal direction.

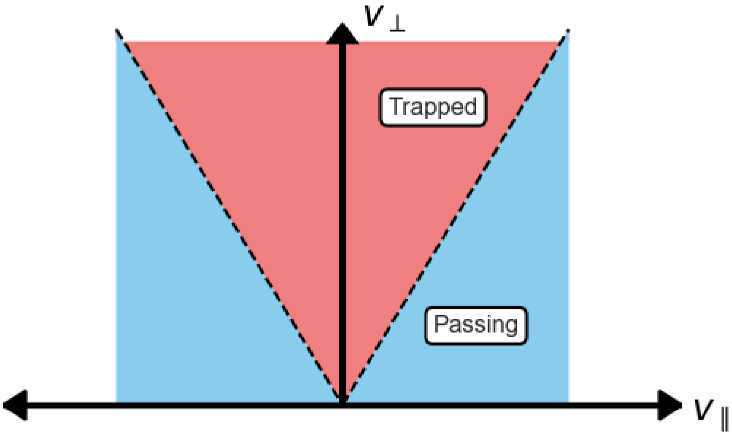

FIGURE 1.4 – Regions of trapped and circulating particles. Reconstructed from (Helander and Sigmar, 2005).

1.3 Particle transport in tokamaks

Understanding transport of matter, energy and momentum is one of the most important issues in the field of controlled nuclear fusion. Transport across the magnetic field which confines the high-temperature plasma threatens the efficiency of magnetic fusion.

During the early stages, the *classical* transport theory had gained a famous reputation by successfully predicting the transport coefficients of plasma, such as diffusion and heat conduction (Braginskii, 1965). However, such classical theory largely underestimates the transport coefficients when it comes to the high-temperature plasma in tokamaks, sometimes by several orders of magnitude.

To remedy this problem, special attention has been dedicated to the effect of the magnetic field in tokamaks, which is spatially inhomogeneous. It turns out that the toroidal magnetic configuration in tokamaks can exert a strong effect on the transport of plasma combined with the collisions. When these effects of the geometry were taken into account, one found transport coefficients closer to the experimental values than the classical ones. The birth of the so-called *neoclassical transport theory* has fascinated many other scientists and a complete and detailed analytical approach was elegantly established thanks to the pioneering works by (Galeev and Sagdeev, 1968; Hinton and Hazeltine, 1976; Hirshman and Sigmar, 1981).

However, as the technology of plasma diagnostics advances, it has been reported that even with the neoclassical theory, the transport coefficients are still underestimated by an order of magnitude. The reason for this discrepancy comes from the fact that plasma in tokamaks is never in a quiescent state due to the background density and temperature gradients. Coupled with the Coulomb forces, the collective nature of the plasma makes the particles behave as *waves*, *modes*, *vortices* and *streamers*, which might also interact between themselves. These fluctuations enhance the transport of matter and energy leading to the so-called *anomalous or turbulent transport* which largely dominates the classical and neoclassical transport.

The ultimate goal of transport theory is to figure out how the fluxes are generated by thermodynamical forces—related to the density, pressure, temperature, and electric potential—and how they are affected by the magnetic configuration and the tokamak geometry. Theoretically, the particle flux across the magnetic surfaces can be readily obtained from the continuity and momentum balance equation (Helander and Sigmar, 2005)

$$\frac{\partial N}{\partial t} + \nabla \cdot (N\boldsymbol{V}) = 0 \tag{1.14}$$

$$mN\frac{\partial \boldsymbol{V}}{\partial t} = -\nabla p + NZe(\boldsymbol{E} + \boldsymbol{V} \times \boldsymbol{B}) + \boldsymbol{\mathcal{F}} \tag{1.15}$$

where we neglected the viscosity term and $\boldsymbol{\mathcal{F}} = \int m\boldsymbol{v}\mathcal{C}(f)d^3\boldsymbol{v}$ is the frictional force and $\boldsymbol{V}$ is the macroscopic fluid velocity. Note that the velocity of a particular particle differs from this average velocity by $\boldsymbol{v}' = \boldsymbol{v} - \boldsymbol{V}$.

Applying Gauss's law to Eq.(1.14) gives

$$\begin{aligned} -\frac{\partial}{\partial t}\int_V N d^3\boldsymbol{r} &= \int_S N\boldsymbol{V} \cdot d\boldsymbol{S} \\ &= \langle \boldsymbol{\Gamma} \cdot \nabla\psi \rangle \int \frac{d\theta d\varphi}{\boldsymbol{B} \cdot \nabla\theta} \end{aligned} \tag{1.16}$$

where we used the surface element $d\boldsymbol{S} = \nabla\psi d\theta d\varphi / \boldsymbol{B} \cdot \nabla\theta$, particle flux $\boldsymbol{\Gamma} = N\boldsymbol{V}$ with the flux surfaces assumed to be frozen. The important term in the above equation is $\langle \boldsymbol{\Gamma} \cdot \nabla\psi \rangle$ which represents the particle flux across the flux surfaces. This term can be further simplified using the relation Eq.(1.4), which writes :

$$\langle \Gamma_s \cdot \nabla\psi \rangle = \langle \Gamma_s \cdot (\boldsymbol{B} \times R\hat{\varphi}) \rangle = \langle (\Gamma_s \times \boldsymbol{B}) \cdot R\hat{\varphi} \rangle = \langle R\hat{\varphi} \cdot (N_s \boldsymbol{V}_s \times \boldsymbol{B}) \rangle \tag{1.17}$$

where the subscript s denotes ion species. To relate this equation with the momentum balance equation, we project Eq.(1.15) on the toroidal direction. Using the flux surface averaged toroidal projection and by assuming the stationary state ($\partial_t = 0$) and an axisymmetric case ($\partial_\varphi = 0$), one can write

$$\begin{aligned} \langle e_s \boldsymbol{\Gamma}_s \cdot \nabla\psi \rangle &= -\langle R\hat{\varphi} \cdot N_s e_s \boldsymbol{E} \rangle - \langle R\hat{\varphi} \cdot \boldsymbol{\mathcal{F}} \rangle \\ &= -\langle N_s e_s R E_\varphi \rangle - \langle R\mathcal{F}_{s\varphi} \rangle \end{aligned} \tag{1.18}$$

After some calculations and using Eq.(1.3), the final form of particle flux can be recast as [5]

$$\langle e_s \Gamma_s \cdot \nabla\psi \rangle = \underbrace{\left\langle \frac{\boldsymbol{B} \times \nabla\psi}{B^2} \cdot \boldsymbol{\mathcal{F}} \right\rangle}_{\text{Classical}} - \underbrace{I\left\langle \frac{\mathcal{F}_{s\parallel} + N_s e_s E_\parallel}{B} \right\rangle}_{\text{Neoclassical}} + \underbrace{\left\langle N_s e_s \frac{\boldsymbol{E} \times \boldsymbol{B}}{B^2} \cdot \nabla\psi \right\rangle}_{\text{Turbulent}} \tag{1.19}$$

The classical flux is related to the perpendicular friction forces while the neoclassical flux is linked to the parallel component of it. This difference explains their underlying mechanism. Classical transport is generated by the frictional relaxation of the diamagnetic flow associated with gyromotion. On the other hand, neoclassical flux is generated through the friction force acting on the guiding center, which flows mainly along the magnetic field line. The last term is related to $\boldsymbol{E} \times \boldsymbol{B}$ drift, and is called turbulent particle flux.

1.3.1 Turbulent transport

Understanding turbulent transport is a challenging task due to the nonlinear features of turbulence. In a linear analysis, where the amplitudes of waves are assumed to be small, the problem can be solved in algebraic form with the help of Fourier transformation, i.e. $\phi_n(\boldsymbol{x}, t) = \phi_0 \exp(i\boldsymbol{k} \cdot \boldsymbol{x} - i\Omega t)$ where $\boldsymbol{k}$ is a wave vector and Ω is a complex frequency. In this simplest form, each mode is characterized by a *dispersion relation* $D(\Omega, \boldsymbol{k}) = 0$. Each solution of this relation defines an *eigenmode*. In the linear approximation, the evolution of each mode is treated independently, thus the nonlinear terms are neglected. An eigenvalue of the dispersion relation can be written as :

$$\Omega(\boldsymbol{k}) = \omega(\boldsymbol{k}) + i\gamma(\boldsymbol{k}) \tag{1.20}$$

---

[5] $\langle e_s \Gamma_s \cdot \nabla\psi \rangle = -\langle N_s e_s R E_\varphi \rangle - \langle R\mathcal{F}_{s\varphi} \rangle = -\langle R\hat{\varphi} \cdot N_s e_s \boldsymbol{E} \rangle - \langle R\hat{\varphi} \cdot \boldsymbol{\mathcal{F}}_s \rangle$
$= -\left\langle \left(\frac{I}{B}\boldsymbol{b} - \frac{\boldsymbol{B}\times\nabla\psi}{B^2} \right) \cdot (N_s e_s \boldsymbol{E}) \right\rangle - \left\langle \left(\frac{I}{B}\boldsymbol{b} - \frac{\boldsymbol{B}\times\nabla\psi}{B^2} \right) \cdot \boldsymbol{\mathcal{F}}_s \right\rangle$
$= -\left\langle I \frac{e_s N_s E_\parallel}{B} \right\rangle + \left\langle N_s e_s \frac{\boldsymbol{E}\times\boldsymbol{B}}{B^2} \cdot \nabla\psi \right\rangle - \left\langle \frac{I}{B}\mathcal{F}_{s\parallel} \right\rangle + \left\langle \frac{\boldsymbol{B}\times\nabla\psi}{B^2} \cdot \boldsymbol{\mathcal{F}}_s \right\rangle$
$= -I\left\langle \frac{\mathcal{F}_{a\parallel} + N_s e_s E_\parallel}{B} \right\rangle + \left\langle N_s e_s \frac{\boldsymbol{E}\times\boldsymbol{B}}{B^2} \cdot \nabla\psi \right\rangle + \left\langle \frac{\boldsymbol{B}\times\nabla\psi}{B^2} \cdot \boldsymbol{\mathcal{F}} \right\rangle$

where the real part $\omega(\boldsymbol{k})$ is the frequency and the imaginary part $\gamma(\boldsymbol{k})$ is the growth rate (and the mode is damped if $\gamma < 0$).

In fusion plasma, many modes are linearly unstable ($\gamma > 0$). For such a mode, the wave amplitude grows exponentially in time, increasing the nonlinear interaction among the waves and individual particles. Since the background density and temperature profiles are inhomogeneous, the radial pressure gradient plays a crucial role in driving unstable modes, which yield turbulent transport (Figure 1.5).

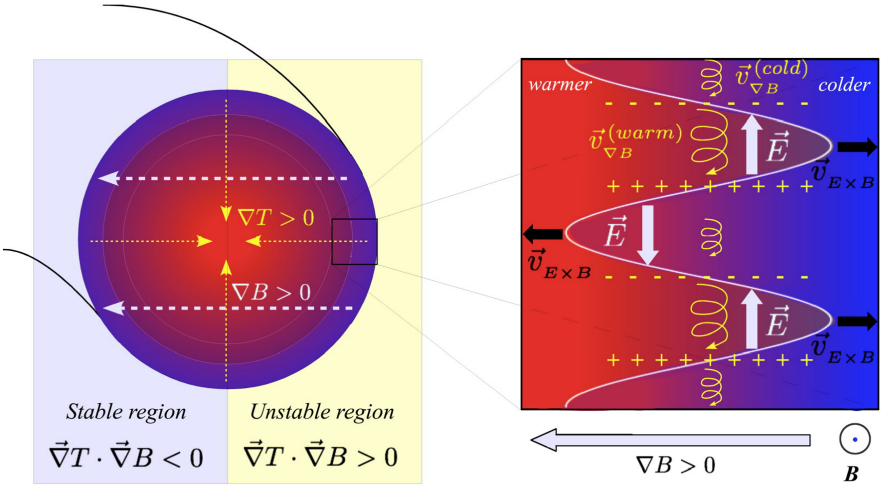

FIGURE 1.5 – (Left) Poloidal section of a tokamak (right) the basic mechanism of the drift kinetic type instability (Del Sarto and Ghizzo, 2017).

In general, two main electrostatic micro-instabilities play a crucial role in turbulent transport : (i) *ion temperature gradient* (ITG) modes and (ii) *trapped electron modes* (TEM). These modes are unstable in the limit of large wavelength such as $k_\perp \rho_i < 1$ where $k_\perp$ is the perpendicular wave and ρ_i is the ion Larmor radius. In tokamaks, these instabilities are induced by the magnetic drift $(v_{\nabla B})$ combined with background density and temperature gradients (Figure 1.5). The initial perturbation (white line) is enhanced since the unbalanced $\boldsymbol{v}_{E\times B}$ amplifies the fluctuations, given the temperature gradient. In non-linear regime, ITG/TEM modes produce particle, momentum, electron and ion heat transport. ITG-driven modes usually depend on the ion temperature logarithmic gradient and also on the ratio of electron to ion temperature T_e/T_i. This mode usually rotates in the ion diamagnetic rotation while TEMs, driven through a resonant interaction of the modes with trapped electrons at the precession frequency, rotates in the electron diamagnetic direction (Garbet et al., 2004).

1.3.2 Neoclassical transport

Neoclassical transport broadens classical transport to include the effects of magnetic field and collisions, which requires the following ordering to be satisfied :

1. The macroscopic scale length L is assumed to be large compared to the Larmor radius $\delta = \rho_c/L \ll 1$ which gives a homogeneous plasma over the gyro motion.
2. the gyrofrequency is much larger than the collision frequency $\nu/\Omega \ll 1$. So, the associated time derivative can often be neglected

$$\frac{\partial}{\partial t} \sim \frac{D}{L^2} \sim \delta^2 \nu \tag{1.21}$$

where ν is the collision frequency and $D \sim \nu\rho^2$ is the diffusion coefficient.

The dynamics of neoclassical transport depends on the relative magnitude of collisionality ν^* which is the ratio of the detrapping frequency $\nu_{\text{detrap}} = \nu/\epsilon$ and the bounce frequency $\omega_b \approx \epsilon^{1/2} v_T/(qR)$.

$$\nu^* = \frac{\nu_{\text{detrap}}}{\omega_b} \approx \frac{qR}{\epsilon^{3/2}} \frac{\nu}{v_T} \tag{1.22}$$

In the weak collisional regime ($\nu^* \ll 1$), also named *banana* regime, passing particles have sufficient time to complete their orbit without any interruption. The radial displacement mainly happens by collisions among trapped particles (the radial displacement due to collisions of passing particles is negligible). Therefore, the typical radial displacement is equal to the width of banana orbit $\Delta l = \delta_b$. Taking into account the fraction of trapped particles $f_t \simeq \sqrt{2\epsilon}$, one can find the perpendicular diffusion coefficient

$$D^{banana} = f_t \delta_b^2 \nu \simeq \frac{q^2}{\epsilon^{3/2}} \rho_c^2 \nu \tag{1.23}$$

In the intermediate collisional regime ($1 \ll \nu^* \ll \epsilon^{-3/2}$), named *plateau*, only a small fraction of trapped particles experience collisions before completing their orbit. Proportional to ω_b/ν, the perpendicular diffusion coefficient can be simply expressed as follows :

$$D^{\text{plateau}} = \frac{\omega_b}{\nu} D^{\text{banana}} \simeq \frac{q v_T}{R} \rho_c^2 \tag{1.24}$$

As the name *plateau* implies, the perpendicular diffusion coefficient of this regime is constant regardless of collisionality (Figure 1.6).

In the strong collisional regime ($\nu^* \gg \epsilon^{-3/2}$), so-called the *Pfirsch-Schlüter* (PS) regime, the orbit of passing / trapped particles is constantly interrupted by collisions. The main transport in this regime, therefore, is usually governed by parallel motion with the diffusion coefficient $D_\parallel \sim v_T^2/\nu$. The displacements of particles Δl due to collisions are caused by the curvature magnetic drift $\boldsymbol{v}_D$ during the time $\tau_\parallel$. Then, the perpendicular diffusion coefficient can be obtained readily

$$D^{\mathrm{PS}} = q^2 \rho_c^2 \nu \tag{1.25}$$

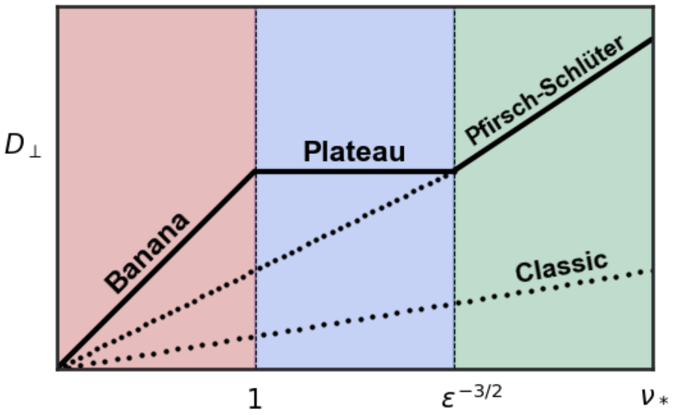

FIGURE 1.6 – Dependence of neoclassical perpendicular diffusion coefficient on collisionality. Reconstructed from (Helander and Sigmar, 2005).

According to the collisionality defined above, the neoclassical particle flux can be separated into different collisional regimes. Therefore, it is meaningful to decompose the neoclassical fluxes ($\Gamma^{\mathrm{neo}} = \Gamma^{\mathrm{BP}} + \Gamma^{\mathrm{PS}}$) from Eq.(1.19) as follows (Helander and Sigmar, 2005) :

$$\langle \Gamma_s \cdot \nabla\psi \rangle^{\mathrm{BP}} = -I \frac{\left\langle B(F_{s\parallel} + N_s e_s E_\parallel^{(A)}) \right\rangle}{e_s \langle B^2 \rangle} \tag{1.26}$$

$$\langle \Gamma_s \cdot \nabla\psi \rangle^{\mathrm{PS}} = -I \left\langle \frac{F_{\parallel s} + N_s e_s E_\parallel^{(A)}}{e_s B} \left(1 - \frac{B^2}{\langle B^2 \rangle} \right) \right\rangle \tag{1.27}$$

The first part relates to the banana-plateau flux which is mainly driven by the pressure anisotropy in the weakly collisional regime. The information of such anisotropy is contained in the frictional force term $F_{s\parallel}$. The second part, corresponding to the Pfirsch-Schlüter flux, results from the poloidal variation of B on the magnetic surfaces. In this regime, the pressure tends to be isotropic due to collisions and its effect is negligible.

Note that the above analytical derivation does not take into account the poloidal asymmetry of impurity density. In the following chapter, the effects of poloidal asymmetry on neoclassical transport will be addressed.

1.4 Impurities in tokamaks

Although an ideal fusion reaction requires only a pure mix of deuterium (D) and tritium (T), the generation of impurities is inevitable in a reactor. During a plasma discharge, different types of impurity can be produced :

1. Helium (He), as the ash of D-T burning plasma, is an inevitable impurity. The hot helium produced by the fusion reaction is often called as α-particle, which will be essential in future tokamak experiments for heating scenarios.
2. Tungsten (W) and carbon (C) are often used as plasma-facing components (PFC). Sputtering of these first wall components results in a substantial impurity source in a tokamak plasma, which yields radiation losses (Figure 1.7).
3. Low-Z or intermediate-Z impurities—argon (Ar), nitrogen (N), and neon (Ne)—are often injected, namely *impurity seeding*, in order to reduce direct heat loads on the divertor plates by radiating in the peripheral region.

In recent decades, a strong emphasis has been placed on the behavior and transport of impurities since even with a small tungsten concentration $\sim 10^{-5}$ (Pütterich et al., 2010), the hot plasma can be completely extinguished by radiation loss. Especially, tungsten is not totally ionized even at the high fusion temperatures and can experience further radiation. Also, increasing impurity concentration naturally decreases the concentration of the main fuel which will degrade the fusion power efficiency (Figure 1.8).

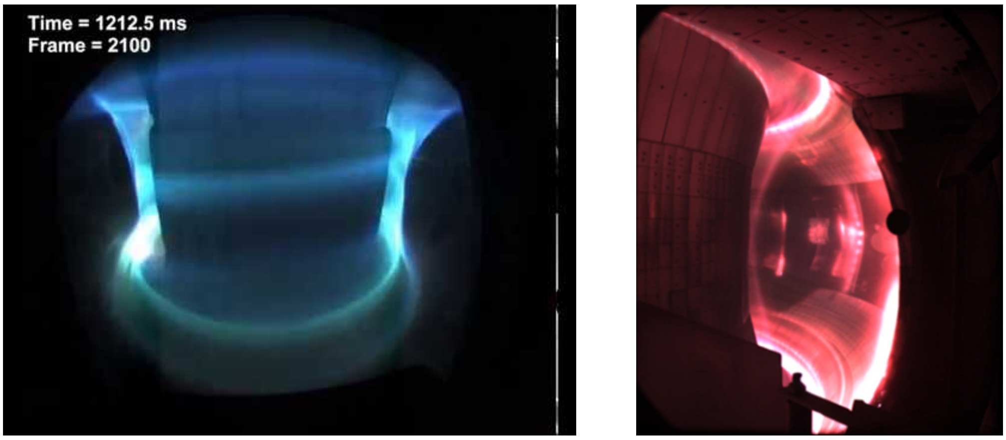

FIGURE 1.7 – (Left) Nitrogen impurity seeding in the COMPASS tokamak (Komm et al., 2019) (right) Tungsten erosion during plasma discharge in the EAST tokamak [6].

---

[6] https://ceramics.org/ceramic-tech-today/nuclear-2/understanding-tungsten-erosion-in-tokamak-walls

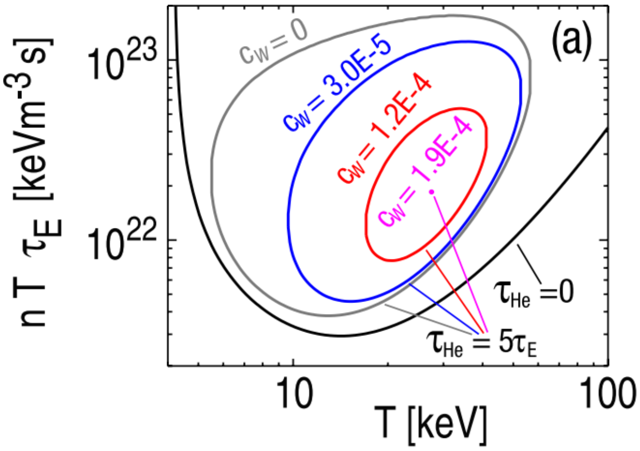

FIGURE 1.8 – Ignition curves in the presence of different W concentrations. When concentration goes high, the surface of achievable ignition condition diminishes (Pütterich et al., 2010).

1.4.1 Impurity accumulation

To achieve maximum fusion efficiency, it is mandatory to minimize and remove the impurities from the plasma. This can be achieved using impurity transport along the open magnetic field lines of the Scrape-Off Layer (SOL), which drives impurities to the divertor plate. It is therefore possible to remove impurities from the plasma while keeping good thermal insulation between the hot plasma and the cold boundary region. However, this task is far from easy to accomplish.

According to the standard neoclassical theory, which explains particle transport driven by collisional effects, impurity flux can be calculated for the case when impurities (main ions) are in the PS (banana) regime and ion-electron collisions are neglected (Hirshman and Sigmar, 1981) :

$$\mathbf{\Gamma}_{z,\mathrm{neo}} = -N_z D\left[\frac{\partial_r N_z}{N_z} - Z\frac{\partial_r N_i}{N_i} + \frac{Z}{2}\frac{\partial_r T_i}{T_i}\right] \tag{1.28}$$

where N_s is the density, T_s is the temperature, D is the diffusion coefficient, Z is the impurity charge and $i(z)$ refers to the main ions (impurity). In the stationary state ($\partial_t \Gamma = 0$), the final impurity density profile can be recast as :

$$\frac{N_z(r)}{N_z(r_0)} = \left(\frac{N_i(r)}{N_i(r_0)}\right)^{Z}\left(\frac{T_i(r_0)}{T_i(r)}\right)^{\frac{Z}{2}} \tag{1.29}$$

According to neoclassical theory, the impurity density depends on the relative peaking of the profiles of main ion density N_i and temperature T_i. Peaked or hollow impurity density profile at the magnetic axis r_0 becomes significant especially for high Z impurities. For example, the central accumulation of heavy impurities, dominated by neoclassical transport, has been frequently observed in many experiments (Ran et al., 1989; Ida et al., 1989; Fussmann et al., 1991; Pasini et al., 1992; Tokar et al., 1997). With a peaked temperature profile, the temperature gradient dependency in Eq.(1.29) would be advantageous, to avoid core accumulation by generating a *temperature screening*. Therefore, a proper use of an external heating system could make it possible to control advantageously impurity transport, and more details about this topic will be discussed below.

Effects of a high impurity concentration in plasma are twofold. When it comes to on-axis accumulation, high Z impurities will experience further ionization by emitting ultraviolet or X radiation, which cools the plasma and reduces the fusion yield (de Vries et al., 2014). When properly controlled, however, the presence of impurities can be beneficial to an improved confinement regime. It is now well known that a properly induced radiation by impurity seeding in the periphery and SOL improves the confinement by reducing localized overheating in the divertor (Schweinzer et al., 2011; Giroud et al., 2013; Kallenbach et al., 2013; Xu et al., 2020).

For these reasons, it is of paramount importance that impurity density profile and impurity concentration have to be controlled and predicted, which is the ultimate goal of the study of impurity transport.

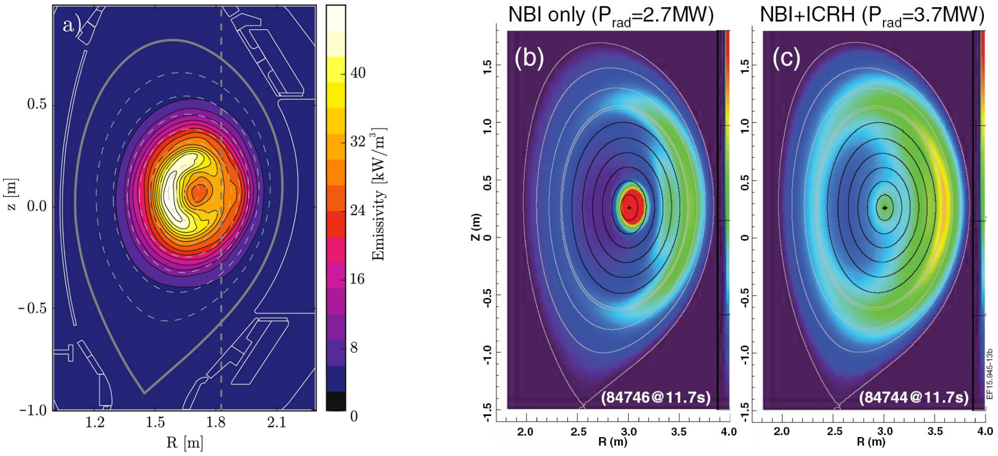

FIGURE 1.9 – (Left) SXR radiation profile from AUG discharge (Odstrcil et al., 2016). (right) ICRH control of impurity accumulation at the core in JET-ILW discharge (Lerche et al., 2016).

1.4.2 Poloidal asymmetry of impurity density

Neoclassical theory often applies the simplifying assumption of uniform density distribution of impurities over each flux surface (Hinton and Hazeltine, 1976). However, with the progress of diagnostics, such as soft X-ray (SXR) cameras and bolometry, this assumption proved to be wrong, and a poloidal asymmetric distribution has been observed repeatedly in many tokamaks. Since the first experimental observation (Terry et al., 1978), the non-uniform distribution of impurity density has received much attention because a strong poloidal asymmetry can modify considerably neoclassical particle flux and even change its direction (Angioni and Helander, 2014).

To determine the poloidal variation of the impurity density, the momentum balance equation can be projected onto the parallel direction to the magnetic field (Fülöp and Helander, 1999)

$$\frac{N_z m_z \omega^2}{2} \nabla_{\parallel} R^2 + Z N_z e \nabla_{\parallel} \phi + T_z \nabla_{\parallel} N_z = 0 \tag{1.30}$$

where $\nabla_{\parallel} = \hat{b} \cdot \nabla$ and ω is the toroidal rotation frequency and the parallel friction and viscosity have been neglected.

The first term in Eq.(1.30) represents the centrifugal force induced by toroidal rotation. It can induce poloidal asymmetry, enhancing its impact, particularly for heavy impurities. The effect of the centrifugal force was theoretically derived in (Wong, 1987), showing that in case of a strong rotation, impurities are pushed away toward the wall, generating *'in-out'* poloidal asymmetry. This situation often happens when neutral beam injection (NBI) is applied as plasma heating.

The second term is related to the parallel gradient of the electrostatic potential. In order to study its effect, it is necessary to solve a quasi-neutrality equation for $\phi(r, \theta)$. Although the poloidal variation will be small for electrons $e\tilde{\phi}/T_e \ll 1$, this effect will be strongly amplified for high Z impurities. External input of energy via waves—*Ion Cyclotron Resonance Heating* (ICRH)—is considered to be one of the main causes, as well as centrifugal effects, for the poloidal electric potential to be modified. For example, when the cyclotron heating is applied, the perpendicular velocity of particles is increased and the number of trapped particles increases, which impact the electric potential. Fortunately, recent experiments indicate that poloidal asymmetry driven by ICRH tends to expel impurities from the core and largely reduce the radiation cooling factor (Figure 1.9).

1.5 Outline

Throughout this introduction, basic notions of nuclear fusion, turbulent and neoclassical particle transport and the importance of studying impurities are addressed. The main goal of this manuscript is to address key aspects of the following general question

How to model impurity transport in the core of tokamaks?

A complete identification of main mechanisms for impurity transport is too broad to be discussed in this manuscript. Hence, only a restricted number of topics will be discussed in the following chapters :

1. **Impurity convection due to turbulence driven by trapped particles**
2. **Impurity neoclassical and turbulent transport of light to heavy impurities**
3. **Impact of the toroidal rotation on impurity transport**

Note that in this manuscript we restrict ourselves to the electrostatic case where the effects of MHD instabilities are neglected.

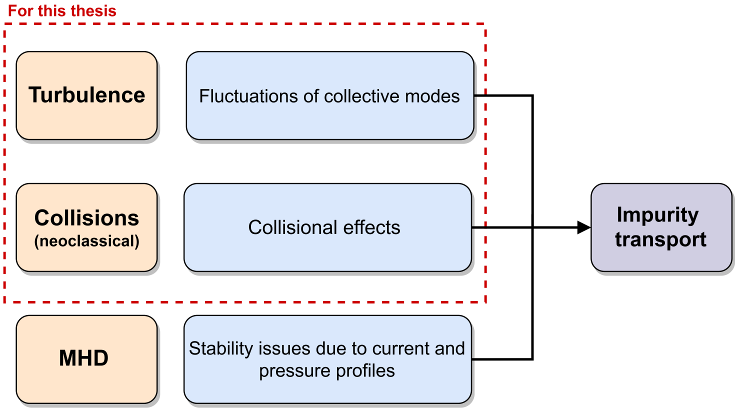

Figure 1.10 – The scope of this thesis. Two main transport channels : (i) turbulent transport (ii) neoclassical transport will be discussed in this manuscript.

Chapitre 2

Gyrokinetic model for impurity transport

Contents

The study of impurity transport requires the understanding of both turbulent and neoclassical transport. Due to the strong interplay between the complex trajectory of charged particles and the fluctuations of collective modes, a wide range of spatio-temporal scales needs to be considered and it necessitates an appropriate model which encompasses such multi-scale nature properly. According to various approaches, plasma models can be roughly classified into *kinetic* models and *fluid* models.

The ultimate goal of plasma modelling is to predict the plasma behavior by solving kinetic or fluid models coupled with Maxwell's equations. To this end, it is necessary to follow the time evolution of the global profiles, such as temperature, density and current, during the energy confinement time τ_E. Although we are fully equipped with the laws of physics which describe the evolution of the plasma, it is untractable to obtain solutions for three-dimensional complex geometry and nonlinear problems. For this reason, plasma research strongly benefits from progress in computational modelling and this aspect will be briefly discussed in this chapter.

2.1 Plasma models

A typical magnetic fusion plasma is composed of approximately $10^{20}\mathrm{m}^{-3}$ of ions and electrons. A complete description of all these particles require a solution of *Newton-Maxwell* equations for all individual particles. These equations consist of a set of $6N$ differential equations which determine the N-body description of the system. This approach of tracking all particles is untractable with the current high performance computing and even in the any foreseeable future. Therefore, the number of equations must be reduced with reasonable assumptions in order to lower the dimension of the system.

2.1.1 Kinetic model

Any physical properties of microscopic detail can be obtained by its position and velocity vectors in *phase space.* Therefore, instead of calculating the dynamics of single particles, it is useful to introduce a statistical approach with the *distribution function* $F(\boldsymbol{r}, \boldsymbol{v}, t)$, which is the density of particles in $(\boldsymbol{r}, \boldsymbol{v})$ space at time t. The evolution of the distribution function is described by the *kinetic theory.*

The *Vlasov* equation describes the evolution of the distribution function in a 6-dimensional phase space $(\boldsymbol{r}, \boldsymbol{v})$ under the effect of self-consistent electric and magnetic fields :

$$\frac{\partial F_s}{\partial t} + \boldsymbol{v} \cdot \frac{\partial F_s}{\partial \boldsymbol{r}} + \frac{q_s}{m_s}(\boldsymbol{E} + \boldsymbol{v} \times \boldsymbol{B}) \cdot \frac{\partial F_s}{\partial \boldsymbol{v}} = 0 \tag{2.1}$$

A great complexity to solve the Vlasov equation emerges from the third term of Eq.(2.1), which contains both the external fields and the self-consistent fields arising from the motion of all charged particles inside the plasma. These fields satisfy the Maxwell equations

$$\nabla \cdot \boldsymbol{E} = \rho/\epsilon_0 \tag{2.2}$$

$$\nabla \cdot \boldsymbol{B} = 0 \tag{2.3}$$

$$\nabla \times \boldsymbol{E} = -\frac{\partial \boldsymbol{B}}{\partial t} \tag{2.4}$$

$$\nabla \times \boldsymbol{B} = \mu_0 \boldsymbol{J} + \frac{1}{c^2}\frac{\partial \boldsymbol{E}}{\partial t} \tag{2.5}$$

where the plasma charge density ρ and the plasma current density **J** are obtained by taking the moments of F_s :

$$\rho(\boldsymbol{x}, t) = \sum_s q_s \int d\boldsymbol{v} F_s \tag{2.6}$$

$$\boldsymbol{J}(\boldsymbol{x}, t) = \sum_s q_s \int \boldsymbol{v} d\boldsymbol{v} F_s \tag{2.7}$$

The set of equations from Eq.(2.1) to Eq.(2.7) constitutes a complete and self-consistent equations which need to be solved simultaneously. The different processes to resolve these nonlinear equations in the *linear*, *quasi-linear* and *nonlinear* approximations form the basis of kinetic theory and one generally has to use numerical methods even for a linear analysis.

2.1.2 Fluid model

The main advantage in using a fluid model is to alleviate the complexities of kinetic equations. The fluid model is based on a set of equations which describes the macroscopic quantities such as density N, mean velocity $\boldsymbol{V}$ and temperature T. These quantities can be readily calculated from the distribution function by multiplying various power of $\boldsymbol{v}$ and then integrating over velocity space. The first three moments of the Vlasov equation, multiplying it by 1, $\boldsymbol{v}$ and $\boldsymbol{v}^2/2$ and integrating over the velocity space, give the equations of conservation of *mass, momentum* and *energy*.

$$\frac{\partial N}{\partial t} + \nabla \cdot (N\boldsymbol{V}) = 0 \tag{2.8}$$

$$\frac{\partial mN\boldsymbol{V}}{\partial t} + \nabla \cdot \boldsymbol{\Pi} = NZe(\boldsymbol{E} + \boldsymbol{V} \times \boldsymbol{B}) \tag{2.9}$$

$$\frac{\partial}{\partial t}\left(\frac{3NT}{2} + \frac{mN\boldsymbol{V}^2}{2}\right) + \nabla \cdot \boldsymbol{Q} = ZeN\boldsymbol{E} \cdot \boldsymbol{V} \tag{2.10}$$

where the following notations for the flux of momentum and energy are used :

$$\text{Pressure tensor : } \Pi_{jk} = \langle mnv_j v_k \rangle_f \tag{2.11}$$

$$\text{Heat flux : } \boldsymbol{Q} = \frac{mn\langle v^2 \boldsymbol{v} \rangle_f}{2} \tag{2.12}$$

The fluid model governs the space-time evolution of macroscopic variables $(N, T, \boldsymbol{V})$ for each species in a fusion plasma. However, each moment equation requires a higher moment equation. For example, the evolution of density N contains the flow velocity $\boldsymbol{V}$, the evolution of $\boldsymbol{V}$ contains the pressure Π and the evolution of temperature T contains the higher moment of heat flux Q. Therefore, it is necessary to truncate these consecutive equations at some point by introducing a simplifying assumption for the hierarchy.

2.1.3 Gyrokinetic model

Although the kinetic model is the most fundamental way to describe a plasma, a broad range of spatio-temporal scales makes it difficult to simulate micro-instabilities and collisional effects via the Vlasov equation. In order to overcome this scale limit, a reduced model called *gyrokinetic model* has been developed. Given the fact that characteristic frequencies of micro-turbulence ω are smaller than the cyclotron frequency ω_c, high frequency scales are averaged in gyrokinetic approach while keeping essential kinetic effects.

Gyrokinetic ordering

In fusion plasma, the presence of a strong magnetic field allows the separation on the dynamics between a gyromotion perpendicular to the magnetic field line with gyrofrequency ω_c and a parallel motion along the magnetic field line with parallel velocity $v_\parallel = \boldsymbol{v} \cdot \boldsymbol{b}$. Under an inhomogeneous magnetic field, charged particles exhibit three types of quasi-periodic motion ; (i) a rapid gyromotion around a magnetic field line with cyclotron frequency ω_c and the Larmor radius ρ_c ; (ii) an intermediate bounce motion with bounce frequency ω_b and the banana width δ_b ; (iii) a slow precession with precession frequency ω_d and the major tokamak radius R_0. The periodic time scales $\omega_d \ll \omega_b \ll \omega_c$ are usually well respected for magnetically confined plasma, allowing to decouple the fast gyromotion from the bounce motion and from the toroidal precession of charged particles.

For plasma turbulence, the characteristic frequencies ω are so much smaller than the cyclotron frequency that a reduction of the dimension can be performed via phase-space coordinate transformations. The modern gyrokinetic theory consists of the guiding-centre transform and a gyro-center transform based on the Hamiltonian or Lagrangian formalism with the Lie perturbation theory (Brizard and Hahm, 2007). In order to apply this approach, a certain ordering should be satisfied. From experimental observations, it has been reported that tokamak micro-turbulence in the core obeys the following gyrokinetic ordering

$$\frac{\omega}{\omega_c} \sim \frac{k_{\|}}{k_{\perp}} \sim \frac{q_s\phi}{T} \sim \frac{\delta N_s}{N_0} \sim \frac{\delta B}{B_0} \sim \frac{\rho_c}{L_N} \sim \mathcal{O}(\rho_s^*) \tag{2.13}$$

where ω is a characteristic frequency of microturbulence, $k_{\|}$ and $k_{\perp}$ are parallel and perpendicular components of the wave vector $\boldsymbol{k}$, δA represents the perturbed quantity A, $L_N = |\nabla \ln N_0|^{-1}$ is a characteristic scale length of N_0 and $\rho_* = \rho_c/a$ is the dimensionless parameter which corresponds to the ratio between the Larmor radius and the tokamak minor radius. Within this gyro-ordering, a gyrokinetic model can be derived by eliminating the high frequency ω_c.

In this framework, one can develop the gyrokinetic equation at an arbitrary order in ρ_* while keeping the Hamiltonian structure of the Vlasov equation. The gyro-averaged Hamiltonian $\bar{H}_s$ can be written as

$$\bar{H}_s = \frac{1}{2} m_s v_{G\|}^2 + \mu B + q_s \bar{\phi} \tag{2.14}$$

Note that gyro-averaging at this stage does not simply mean averaging out the cyclotron motion, but the the transform should retain the information of the fields at the Larmor radius scale.

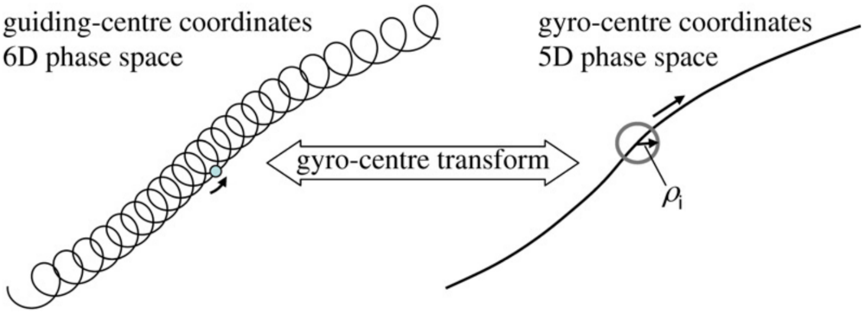

FIGURE 2.1 – Reproduced from (Garbet et al., 2010). By applying gyro-centre transform, the dimensionality is reduced by one and the high frequency motion is averaged. Here guiding-centre represents the point around which particles circle while gyro-centre signifies a new coordinate obtained from gyro-centre transformation.

2.2 Numerical features of gyrokinetic codes

In this manuscript, we use two different gyrokinetic models, implemented in two gyrokinetic codes :

1. GYSELA-5D (**GY**rokinetic **SE**mi-**LA**grangian) (see section 2.3)
2. TERESA-4D (**T**rapped **E**lement **RE**duction in **S**emi-lagrangian **A**pproach) (see section 2.4)

These codes are developed at IRFM (Institute for Magnetic Fusion Research) and IJL (Institut Jean Lamour) with strong collaborations at both national and international levels. Before we proceed to the theoretical derivation of the two models, let us discuss key numerical features of both codes.

Originated from the same Semi-Lagrangian family, GYSELA and TERESA share a lot of numerical common points, such as *global* geometry, *full-f* approach, *Semi-Lagrangian* numerical scheme and capability of treating *kinetic electrons*. The main differences between two codes arise from ; (i) the way in which they drive plasma out of equilibrium, *gradient driven* in TERESA and *flux driven* in GYSELA (ii) species of interest ; passing and trapped particles in GYSELA and only trapped particles in TERESA, which means TERESA can be considered as a reduced model when compared to GYSELA. A brief description of these salient features is given in Table 2.1. Regarding more detailed information on numerical features in gyrokinetic code, the reader is referred to (Garbet et al., 2010). A brief overview of numerical schemes for the Vlasov equation will be discussed in the following section.

Semi-Lagrangian method

Since the pioneering work by (Lee, 1983), known as a first gyrokinetic code, three different types of numerical schemes have become mainstream over the last few decades :

1. *Lagrangian* method uses a discrete description of macro-particles in phase space. Each macro-particle represents a large number of plasma particles. These macro particles follow the characteristics of the Vlasov equation, along which the distribution function is exactly conserved, while charge and current densities need to be calculated by extrapolation. The main drawback of the Lagrangian method is that not only the inherent numerical noise makes hard to describe the distribution function accurately, but it accumulates in time also.
2. *Eulerian* method uses a fixed grid in all directions of phase space in order to avoid numerical noise from Lagrangian method, and applying finite differences or spectral methods to model the Vlasov equation. Although it is noise free, the integro-differential equation imposes the Courant-Friedrichs-Lewy (CFL) stability condition, which constraints the maximum time step of numerical simulation.
3. To take advantage of both methods and avoid limitations, *Semi-Lagrangian* method has been applied in GYSELA & TERESA with an accurate description of the

phase space. The fixed grid point (Eulerian) is adopted in order to avoid numerical noise and the characteristics of the Vlasov equation are used for the time evolution of the distribution function. A more detailed information about Semi-Lagrangian method can be found in (Sonnendrücker et al., 1999).

TABLE 2.1 – Different types of gyrokinetic models

Electrostatic	**Electromagnetic**
· Magnetic field is prescribed externally	· Ampère's law and self-generated currents are taken into account

Global	**Local**
· The whole plasma in toroidal geometry is treated numerically	· Local region around the magnetic field, *i.e.* flux tube, is treated numerically.

Adiabatic electrons	**Kinetic electrons**
· Electrons are assumed to follow a Boltzmann response in a flux surface	· Electrons are treated kinetically in the same way as ions

Full-F	δF
· The whole distribution function $F = F_{\text{eq}} + \delta F$ is numerically treated without any scale separation · The back reaction of turbulent transport is accounted for in the time evolution of the equilibrium · The mean gradients are somewhat maintained or can be relaxing in time by a prescribed heat source (*flux driven*). · More appropriate within a global description	· Only the deviation part δF from the Maxwellian is numerically treated with the assumption ($\delta F \ll F_{\text{eq}}$) · Statistical noise is largely reduced due to the scale separation, contributing to the stability of numerical simulations · The mean gradients are naturally imposed in the assumed equilibrium (*gradient driven*) · More appropriate within a local (flux tube) description

2.3 GYSELA-5D : Gyrokinetic model

GYSELA (**GY**rokinetic **SE**mi-**LA**grangian) is a *global, full-F, flux driven, electrostatic* gyrokinetic code which treats *electrons adiabatically*[7] in a simplified concentric circular magnetic configuration. The time evolution of the full distribution function of each ion species (Deuterium + impurity) is governed self-consistently by a 5D non-linear gyrokinetic Vlasov equation coupled with 3D Poisson equation. In this section, the salient features of the code are presented in a concise manner. For a more detailed analytical derivation of GYSELA, the reader is referred to (Grandgirard et al., 2016).

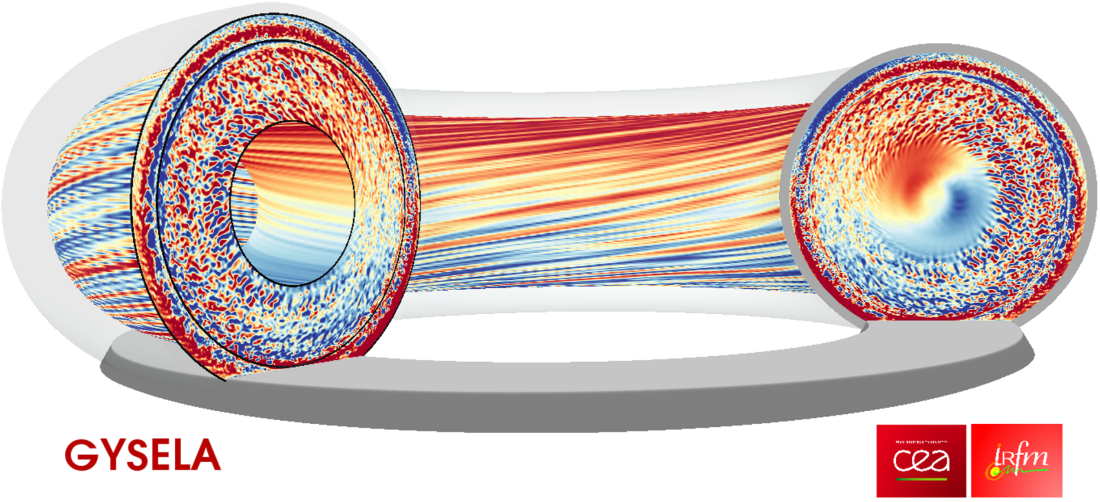

FIGURE 2.2 – 3D visualization of the turbulent fluctuations of the electric potential resulting from the GYSELA-5D simulations[8].

2.3.1 Gyrokinetic Vlasov equation

Unlike δF-algorithm, GYSELA deals with the evolution of 5D gyro-center distribution function $\bar{F}$ for each species without any segregation between equilibrium and perturbation. In the Hamiltonian formulation (Brizard and Hahm, 2007), the 5D colli-

---

[7] Although kinetic treatment of electrons was implemented in GYSELA, it hasn't been fully tested. Therefore, we restrict ourselves solely to adiabatic electrons in this manuscript.

[8] GYSELA-X git repository (https://gyselax.github.io/)

sional gyrokinetic equation can be recast as

$$\begin{aligned}\frac{d\bar{F}_s}{dt} &= \frac{\partial \bar{F}_s}{\partial t} + [\bar{F}_s, \bar{H}_s] \\ &= \frac{\partial \bar{F}_s}{\partial t} + \frac{d\mathbf{x}_G}{dt} \cdot \frac{\partial \bar{F}_s}{\partial \mathbf{x}_G} + \frac{dv_{G\|}}{dt}\frac{\partial \bar{F}_s}{\partial v_{G\|}} \\ &= \mathcal{C}(\bar{F}_s) + \mathcal{S}(\bar{F}_s)\end{aligned} \tag{2.15}$$

where $\mathcal{C}$ and $\mathcal{S}$ are respectively a collision operator and source terms and $[F, G]$ is the gyrokinetic Poisson bracket operator, defined as

$$\begin{aligned}[F, G] = \frac{\omega_s}{B^*_{\|,s}}\left(\frac{\partial F}{\partial \alpha}\frac{\partial G}{\partial \mu} - \frac{\partial F}{\partial \mu}\frac{\partial G}{\partial \alpha}\right) - \frac{\boldsymbol{b}}{q_s B^*_{\|,s}} \cdot \nabla F \times \nabla G \\ + \frac{\boldsymbol{B}^*_{\|,s}}{m_s B^*_{\|,s}} \cdot \left(\nabla F \frac{\partial G}{\partial v_{G\|}} - \frac{\partial F}{\partial v_{G\|}} \nabla G\right)\end{aligned} \tag{2.16}$$

where $\boldsymbol{B}^* = \boldsymbol{B} + (m_s v_{G\|}/q_s)\nabla \times \boldsymbol{b}$ and $B^*_{\|,s} = \boldsymbol{b} \cdot \boldsymbol{B}^*$ is the volume element in the guiding-center velocity space. Within the electrostatic limit, the evolution of gyro-center coordinates associated to Eq.(2.15) are described by

$$\frac{B^*_{\|,s}}{B}\frac{d\mathbf{x}_G}{dt} = v_{G\|}\boldsymbol{b} + \boldsymbol{v}_{E\times B} + \boldsymbol{v}_D \tag{2.17}$$

$$\frac{B^*_{\|,s}}{B} m_s \frac{dv_{G\|}}{dt} = -q_s \boldsymbol{b} \cdot \nabla \bar{\phi} - \mu \boldsymbol{b} \cdot \nabla \boldsymbol{B} + \frac{m_s v_{G\|}}{B} v_{E\times B} \cdot \nabla \boldsymbol{B} \tag{2.18}$$

$$\frac{B^*_{\|,s}}{B} m_s \frac{d\mu}{dt} = 0 \tag{2.19}$$

where the guiding center drifts are defined respectively

$$\boldsymbol{v}_{E\times B} = \frac{\boldsymbol{B} \times \nabla \bar{\phi}}{B^2} \tag{2.20}$$

$$\boldsymbol{v}_D = \frac{m_s v_\|^2 + \mu B}{q_s} \frac{\boldsymbol{B}}{B^2} \times \frac{\nabla B}{B} \tag{2.21}$$

Combining Eq.(2.17, 2.18) with Eq.(2.15) gives the non-linear Vlasov equation of the gyro-centers in the conservative form :

$$B^*_{\|,s}\frac{\partial \bar{F}_s}{\partial t} + \nabla \cdot \left(B^*_{\|,s}\frac{d\mathbf{x}_G}{dt}\bar{F}_s\right) + \frac{\partial}{\partial v_{G\|}}\left(B^*_{\|,s}\frac{dv_{G\|}}{dt}\bar{F}_s\right) = \mathcal{C}(\bar{F}_s) + \mathcal{S}(\bar{F}_s) \tag{2.22}$$

It can be readily seen from Eq.(2.22) that (i) the above equation doesn't contain any gyro-angle dependency, according to which the dimensionality is reduced by one and the high frequency motions are removed (ii) it doesn't have $\partial/\partial\mu$ due to the conservation of magnetic moment, thus μ enters as a parameter.

2.3.2 Quasi-neutrality equation

In the electrostatic case where the value of β—the ratio of the kinetic energy to the magnetic energy—is assumed to be small, the electric potential can be calculated from the Poisson equation.

$$\nabla^2\Phi = -\frac{1}{\epsilon_0}\sum_s N_s q_s \tag{2.23}$$

where ϵ_0 is the permittivity of vacuum. The above equation can be further simplified using the electron Debye length $\lambda_e = \sqrt{\epsilon_0 T_e/N_0 e^2}$ where N_0 stands for a typical plasma density, which leads to

$$\lambda_e^2\nabla^2\left(\frac{e\Phi}{T_e}\right) = -\frac{1}{N_0}\sum_s N_s q_s \tag{2.24}$$

Since the characteristic length of gyrokinetic model is much longer than the electron Debye length by several orders of magnitude, the term $\lambda_e^2\nabla^2$ in the above equation can be neglected. As a result, the plasma is considered to be in quasi-neutral state and the final form of the Poisson equation satisfies this condition as follows :

$$\tilde{N}_e = \sum_i \tilde{N}_i e_i \tag{2.25}$$

where the perturbed density is defined as $\tilde{N} = N - \langle N\rangle_{\text{FS}}$. Therefore, the quasi-neutrality equation can be closed if the perturbed density for each species is correctly obtained.

For ion species, a special attention has to be paid since the density in Poisson's equation is not the density of gyro-centers but the density of particles. Thus, one can show that the perturbed ion density is composed of the density of gyrocenter N_{Gs} and the polarization density $N_{pol,s}$

$$\tilde{N}_s = \underbrace{\int(\bar{F}_s - \bar{F}_{eq,s})d^3\boldsymbol{v}}_{\text{gyrocenter density}} + \underbrace{\nabla_\perp\cdot\left(\frac{m_s N_{eq,s}}{q_s B^2}\nabla_\perp\Phi\right)}_{\text{polarization density}} \tag{2.26}$$

where $N_{eq,s}$ is the equilibrium density of the species s and $\bar{F}_{eq,s}$ is the equilibrium distribution of gyro-centers which takes the following form

$$\bar{F}_{eq,s} = N_{eq,s}\left(\frac{m_s}{2\pi T_{eq,s}}\right)^{3/2}\exp\left\{-\frac{m_s\boldsymbol{v}_s^2}{2T_{eq,s}}\right\} \tag{2.27}$$

For electrons, the polarization density is often neglected due to their small mass ($m_e \ll m_i$). In this condition, the parallel dynamics of electrons are so fast that electrons can reach a Boltzmann equilibrium instantaneously leading to the so-called *adiabatic electron response*. In this approach, we assume $\tilde{N}_e = 0$ for the modes which remain constant on a flux surface. Then, the adiabatic electron density reads :

$$N_e = N_{eq,e} \exp\left\{ \frac{e}{T_e}(\phi - \langle\phi\rangle_{FS}) \right\} \tag{2.28}$$

Using small value of ϕ, a perturbed electron density can be obtained by a Taylor expansion of Eq.(2.28)

$$\tilde{N}_e = \frac{N_{eq,e}e}{T_e}(\phi - \langle\phi\rangle_{\mathrm{FS}}) \tag{2.29}$$

$$\tilde{N}_e(\mathbf{x}_G, t) = \sum_i q_i \tilde{N}_i(\mathbf{x}_G, t) \tag{2.30}$$

Inserting Eq.(2.26, 2.29) into Eq.(2.25) gives the final form of quasi-neutrality equation as follows :

$$\frac{N_{eq,e}e}{T_e}(\phi - \langle\phi\rangle_{\mathrm{FS}}) = \sum_i e_i \left[\nabla_\perp \cdot \left(\frac{N_{eq,i}m_i}{q_i B^2} \nabla_\perp \phi \right) + \int d^3\boldsymbol{v}(\bar{F}_i - \bar{F}_{eq,i}) \right] \tag{2.31}$$

With the Vlasov equation (2.22) and the quasi-neutrality equation (2.31), we now have a closed set of gyrokinetic equations in the electrostatic limit. Given the electric potential, the 5D gyro-center distribution function $\bar{F}$ is evolved by the Vlasov equation, which again can be used to calculate the electric potential by Poisson's equation.

Although the analytical derivations we have described seem rather short and simple, the theoretical formalism and its numerical implementations are sophisticated. For better understanding, the Hamiltonian and Lagrangian physics should be drawn from differential geometry and Lie-transform perturbation methods. An exhaustive and detailed derivation can be found in (Brizard and Hahm, 2007).

2.3.3 Collisional operator

Although the main transport channel in core fusion plasma is turbulent transport, adding a collision operator might be advantageous for several reasons. First of all, collisional damping of turbulence generated large flow, such as zonal flow, can enhance turbulent transport (Lin et al., 1999). Second, neoclassical transport can be dominant, especially for heavy impurities even in the core of fusion plasma and in certain regions where transport barriers are located, therefore synergy between turbulence and neoclassical effects might play an important role on impurity transport (Estève et al., 2018). Third, the stabilization of trapped electron mode (TEM) depends sensitively on collisional effects by which the resonance of trapped particles with the precession motion are weakened due to a modification of the perturbed distribution function (Manas et al., 2015). Finally, from the numerical point of view, the relaxation process toward Maxwellian due to collisions can smooth small scale structures in velocity space, which can contribute to the stability of gyrokinetic simulations (Abel et al., 2008).

For this purpose, a linearized model of collision operator has been implemented in GYSELA, satisfying the conservation of particles, momentum, energy and also Boltzmann's H-theorem (Donnel et al., 2019a). Furthermore, it has also been benchmarked against neoclassical theory by reproducing a good agreement. This operator was constantly employed in GYSELA simulations, so it is instructive to make a short description of the collision operator.

The linearized collision operator describing the collisions of species a colliding on species b can be expressed as :

$$\mathcal{C}_{ab}(F_a, F_b) = \mathcal{C}^0_{ab}(F_{M0a}, F_{M0b}) + \mathcal{C}^1_{ab}(F_a, F_b) \tag{2.32}$$

where $F_{M0s} = F_s - \delta F_s$ is the local unshifted Maxwellian distribution function and $\mathcal{C}^0_{ab}$ represents the exchange of energy between the unshifted Maxwellians and the second term $\mathcal{C}^1_{ab} = \mathcal{C}_{ab}(\delta F_a, F_{M0b}) + \mathcal{C}_{ab}(F_{M0a}, \delta F_b)$ consists of three terms

$$\mathcal{C}^1_{ab}(F_a, F_b) = \mathcal{C}_{\nu,ab}(F_a) + \mathcal{C}_{d,ab}(F_a) + \mathcal{C}_{\parallel,ab}(F_a, F_b) \tag{2.33}$$

The first term $\mathcal{C}_{\nu,ab}$ deals with the norm of the velocity $(v_\parallel, v_\perp)$ while the second term $\mathcal{C}_{d,ab}$ modifies the direction of the velocity vector. The last term $\mathcal{C}_{\parallel,ab}$ ensures momentum exchange between species and the total conservation of parallel momentum. Given their different roles, it is customary to separate the evolution of the distribution function at equilibrium and its perturbed part, which reads

$$\begin{aligned} \frac{\partial F_{M0a}}{\partial t} &= \sum_b \mathcal{C}^0_{ab}(F_{M0a}, F_{M0b}) \\ \frac{\partial \delta F_a}{\partial t} &= \sum_b \mathcal{C}^1_{ab}(F_a, F_b) \end{aligned} \tag{2.34}$$

Consequently, effects of collisions on the distribution function can be computed by Eq.(2.34) at each collisional time step Δt_{coll} and the modified distribution function evolves via the gyrokinetic Vlasov equation (2.15) by generating neoclassical transport of particles. A more detailed analytical derivation and numerical implementation can be found in (Donnel et al., 2019a).

2.3.4 External sources

In flux driven simulations, the equilibrium profiles should be maintained by a prescribed heat source in order to take into account the back reaction of turbulent transport. In the absence of heat source, the turbulent regime is evanescent by flattening the temperature profile and the system relaxes quickly towards a marginal state. Furthermore, in the context of the long time simulation, up to energy confinement time, the implementation of a heat source is essential. In GYSELA, a versatile source has been implemented by using projections of the velocity dependent part of the source onto the orthogonal basis of *Hermite* H_h and *Laguerre* L_l polynomials (Sarazin et al., 2011).

$$\mathcal{S}(r,\theta,v_{G\parallel},\mu) = \sum_{l=0}^{+\infty}\sum_{h=0}^{+\infty} c_{hl}(r,\theta)H_h(v_\parallel)L_l(\mu)e^{-\bar{v}_\parallel^2-\bar{\mu}} \tag{2.35}$$

where we used the normalized parallel velocity $\bar{v}_{G\parallel} = v_{G\parallel}/\sqrt{2T/m}$ and the normalized magnetic moment $\bar{\mu} = \mu B/T$. A separate injection of particles, heat and parallel momentum can be accomplished by choosing a proper coefficient c_{hl}. A more detailed analytical derivation of how to properly choose these coefficients can be found in (Sarazin et al., 2011). Here, we simply use the final form of heat and momentum source. First, the pure heating source can be written as :

$$S_{\text{heat}} = \frac{S_0 S_r}{\sqrt{2}\pi^{3/2}T^{5/2}}\left[\bar{v}_{G\parallel}^2 - \frac{1}{2} - \frac{J_{\parallel B}}{2 - J_{\parallel B}^2}(2-\bar{\mu})(2\bar{v}_{G\parallel} - J_{\parallel B})\right]e^{-\bar{v}_{G\parallel}^2-\bar{\mu}} \tag{2.36}$$

where $J_{\parallel B} = \sqrt{2T_{sce}}J_\parallel/B^2$ with the parallel current $J_\parallel$. The radial envelope profile S_r is composed of the sum of two hyperbolic tangents and the term S_0 corresponds to the amplitude of source that we can choose arbitrarily. In a similar manner, the pure source of parallel momentum can be expressed as

$$S_{\text{mom}} = \frac{S_0^{v_{G\parallel}} S_r}{4\pi^{3/2}T^2}[2\bar{v}_{G\parallel}(2-\bar{\mu}) - J_{\parallel B}(1 + 2\bar{v}_{G\parallel}^2 - \bar{\mu})]e^{-\bar{v}_{G\parallel}^2-\bar{\mu}} \tag{2.37}$$

Prescribing heat and parallel momentum sources has numerous advantages in terms of mimicking experimental additional heating system, such as ICRH (Ion Cyclotron Resonance Heating) and NBI (Neutral Beam Injection). As has been previously reported by several authors, different sources of external heating, which sustain the hot plasma in tokamaks, can have a significant impact on impurity transport (Hinton and Wong, 1985; Lerche et al., 2016; Angioni et al., 2017). Effects of adding a toroidal momentum source on impurity transport in GYSELA is addressed in Chapter 5.

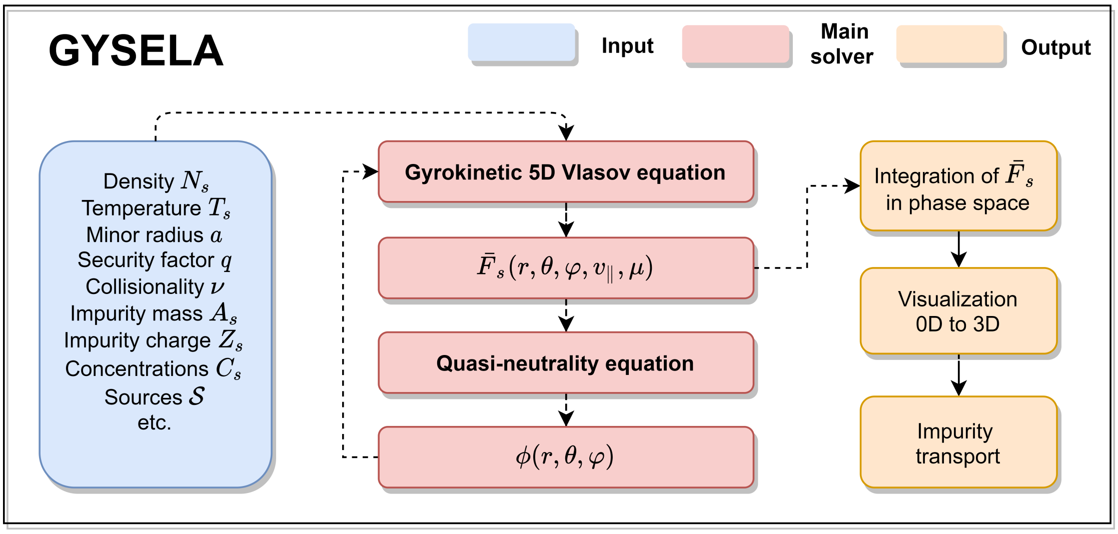

FIGURE 2.3 – Schematic view of GYSELA-5D code.

2.4 TERESA-4D : Gyro-bounce kinetic model

Low frequency turbulence driven by micro-instabilities is responsible for the anomalous heat and particle transport in magnetically confined fusion plasma. Among these instabilities, trapped electron modes (TEM) might play an important role in explaining the anomalous heat and particle transport observed in tokamaks. In this section, a bounce averaged gyrokinetic model, named TERESA (**T**rapped **E**lement **RE**duction in **S**emi-lagrangian **A**pproach) dedicated to instabilities driven by trapped particles will be presented. TERESA is a global, full-f gyro-bounce kinetic code which covers both TIM/TEM regimes simultaneously in 4D. Unlike GYSELA, the equilibrium profile is maintained by thermal baths and only trapped particles, both kinetic ions and kinetic electrons, are treated self-consistently. A detailed derivation is available in (Drouot, 2015).

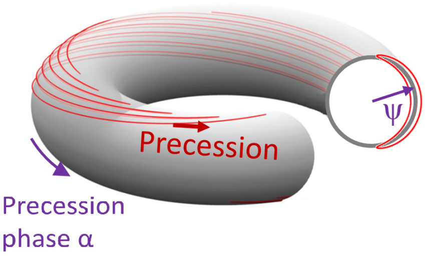

FIGURE 2.4 – By applying gyro-centre transform, the dimensionality is reduced by one and the high frequency motions are removed (Drouot et al., 2014).

2.4.1 Action and angle variables

In classical mechanics, *Hamiltonian-Jacobi* theory provides an useful framework by which dynamics of motion are solved with the help of a coordinate transformation. One powerful transformation often used is the transformation from a set of position-momentum $(\boldsymbol{p}, \boldsymbol{q})$ coordinates to the action-angle $(\boldsymbol{J}, \alpha)$ variables (Goldstein, 1980). A dynamical system which shows integrable and quasi-periodic particle motions, such as tokamaks, is an ideal framework to use action and angular variables. Under this transformation, frequencies of periodic motions are obtained without solving the equations of motion ; and the Hamiltonian becomes function of $\boldsymbol{J}$ only.

$$\frac{dJ}{dt} = -\frac{\partial H}{\partial \alpha} = 0 \qquad\qquad \frac{d\alpha}{dt} = \frac{\partial H}{\partial J} = \omega \tag{2.38}$$

For trapped particles, the motion of a charged particle can be separated into three parts : (i) the cyclotron motion with the Larmor radius ρ_c and the cyclotron frequency ω_c (ii) the bounce motion characterized by the banana width δ_b and the bounce frequency ω_b (iii) the toroidal precession by the major tokamak radius R_0 and the precession frequency ω_d. These periodic motions are related respectively to the action-angle variables $(\boldsymbol{J}, \alpha)$, which can be expressed as (Depret et al., 2000; Sarazin et al., 2005) :

$$\boldsymbol{J} = \begin{cases} J_1 = -\frac{m_s}{q_s}\mu \\ J_2 = \oint \frac{m_s v_{\parallel s}}{2\pi} ds \\ J_3 = q_s \psi_0 \end{cases} \quad \alpha = \begin{cases} \alpha_1 = \omega_c(J)t + \alpha_{10} \\ \alpha_2 = \omega_b(J)t + \alpha_{20} \\ \alpha_3 = \omega_d(J)t + \alpha_{30} \end{cases} \tag{2.39}$$

where ψ_0 is the poloidal magnetic flux at the bounce point. It should be noted that ψ is used as a radial coordinate in this manuscript since $d\psi = -R_0 B_\theta dr$ where B_θ is the poloidal magnetic field.

In a tokamak configuration, the above characteristic time-space scales satisfy the following order, $\omega_d \ll \omega_b \ll \omega_c$ and $\rho_c \ll \delta_b \ll R_0$. Given that the turbulence driven by trapped particles is characterized by the order of the precession frequency ω_d, the disparate time scale allows the removal of the fast cyclotron phase θ_c and the bounce angle θ_b ; the resulting bounce-averaged kinetic description preserves the invariance of the magnetic moment J_1 and the bounce action J_2.

The analytical derivation of the precession frequency ω_d can be found in (?). For a large aspect ratio tokamak, the toroidal precession frequency for species s can be expressed as :

$$\omega_d = \frac{q}{a}\frac{E}{eZB_{\min}R_0}\bar{\omega}_d \quad \text{with} \quad \bar{\omega}_d = \frac{2\mathcal{E}(\kappa^2)}{\mathcal{K}(\kappa^2)} - 1 + 4s_0\left(\frac{\mathcal{E}(\kappa^2)}{\mathcal{K}(\kappa^2)} + \kappa^2 - 1\right) \tag{2.40}$$

where q is the safety factor, E is the kinetic energy, $\kappa = \sqrt{\frac{1-\lambda}{2\epsilon\lambda}}$ is the pitch-angle parameter with $\lambda = \mu B_{\min}/E$, s_0 is the magnetic shear and $\mathcal{K}(\kappa^2)$ and $\mathcal{E}(\kappa^2)$ are the first and second kind elliptic functions respectively.

Note that the precession frequency does not depend on the mass of the particle but on its charge. Since the toroidal precession of ions and electrons are in opposite directions but have the same time scale, it enables the investigation of both TIM and TEM regimes with a minimum of numerical constraints.

2.4.2 Gyro-bounce Vlasov equation

As a result of the dimension reduction by averaging the kinetic equation over the bounce motion, our initial 6D model comes to 4D kinetic model. In order to obtain the final form of the equations, let us consider now the Vlasov equation :

$$\frac{\partial F_s}{\partial t} + [F_s, H_s] = 0 \tag{2.41}$$

where $[A, B]$ is the Poisson bracket defined in action-angle variables :

$$[A, B] = \frac{\partial A}{\partial \alpha_i}\frac{\partial B}{\partial J_i} - \frac{\partial A}{\partial J_i}\frac{\partial B}{\partial \alpha_i} \tag{2.42}$$

Using the fact that the equilibrium Hamiltonian depends only on the action variable $\boldsymbol{J}$ (Eq 2.38) and by gyro-averaging the cyclotron motion and the bounce motion, one can further simplify Eq.(2.41) as follows :

$$\frac{\partial \bar{F}_s}{\partial t} + \frac{1}{q_s}\frac{\partial \bar{H}}{\partial \psi_0}\frac{\partial \bar{F}_s}{\partial \alpha_3} = 0 \tag{2.43}$$

where we used $J_3 = q_s\psi_0$ and the bar notation represents an averaged quantity.

The Hamiltonian at the equilibrium leads to

$$\frac{1}{q_s}\frac{\partial \bar{H}}{\partial \psi_0} = \omega_{d,s} \qquad \rightarrow \qquad \bar{H} = E(1 + q_s\Omega_d\psi_0) \tag{2.44}$$

with $\Omega_d = \frac{\omega_d Z_s}{E}$ which does not depend on the radial direction.

$$\bar{H}_s = E(1 + q_s\Omega_d\psi_0) + eZ_s\bar{\phi}(\boldsymbol{J}, \alpha_3) \tag{2.45}$$

Applying the gyro-bounce average operator filters the fast frequencies ω_c and ω_b and the small radial scales ρ_c and δ_b by reducing the dimensionality of the model from 6D to 4D. The final form of the gyro-bounce average operator $\mathcal{J}_{0s}$ reads (Depret et al., 2000)

$$\mathcal{J}_{0s} = \left(1 - \frac{E}{T_{eq,s}}\frac{\delta_{b,s}^2}{4}\partial_\psi^2\right)^{-1}\left(1 - \frac{E}{T_{eq,s}}\frac{q_0^2\rho_{c,s}^2}{4a^2}\partial_\alpha^2\right)^{-1} \tag{2.46}$$

where $\rho_{c,s}$ and $\delta_{b,s}$ are the Larmor radius and the banana width respectively and $T_{eq,s}$ is the equilibrium temperature of the species s.

Finally, the bounce-averaged Vlasov equation for species s can be expressed as :

$$\frac{\partial F_s}{\partial t} - [\mathcal{J}_s\phi, F_s] + \frac{\Omega_d E}{Z_s}\frac{\partial F_s}{\partial \alpha_3} = 0 \tag{2.47}$$

where F_s is the distribution function of the banana centers. The overbar notation will be omitted hereafter for the readability of the equation. It is important to note that the final reduced model involves two parameters (E, κ) in energy space and two coordinates (ψ, α) (note that only $\alpha = \alpha_3$ is left at the end due to the gyro-bounce average operator) in real space.

2.4.3 Quasi-neutrality equation

As discussed in the previous section (2.3.2) where we assumed that the characteristic length of our numerical model is much longer than the electron Debye length λ_e, the quasi-neutrality equation can be simply expressed as a sum of the perturbed density for each species :

$$\sum_s \tilde{N}_s q_s = 0 \tag{2.48}$$

Consequently, it is essential to formulate properly the perturbed density, which consists of *adiabatic* passing particles and *kinetic* trapped particles.

$$\tilde{N}_s = N_{s,\text{passing}} + N_{s,\text{trapped}} - N_{eq,s} \tag{2.49}$$

For the trapped particles density, the bounce-averaged distribution function should be integrated over velocity in angle-action variables. A more rigorous derivation can be found in (Drouot, 2015), and here we use the final expression for the sake of simplicity. Then, the trapped particles density can be written as :

$$N_{s,trapped} = 4\pi\sqrt{2}m_s^{-3/2}\left(\int_1^{1-2\epsilon}\frac{d\lambda}{4\bar{\omega}_b}\int_0^{+\infty}\mathcal{J}_{0s}\bar{F}_s E^{1/2}dE\right) + \frac{q_s N_{eq,s} f_T}{T_s}\bar{\Delta}_s(\Phi) \tag{2.50}$$

where we introduced the trapped-particle fraction $f_T = 2\sqrt{2\epsilon}/\pi$ and the operator $\bar{\Delta}_s$ to describe the polarization density which arises from the difference between the bounce-averaged banana center and real trapped particle densities across a field line.

$$\bar{\Delta}_s(\Phi) = \left(\frac{q\rho_{c,s}}{a_\psi}\right)^2\partial_\alpha^2 + \delta_{b,s}^2\partial_\psi^2 \tag{2.51}$$

For the passing particle density, the analytical form can be expressed in a relatively simple manner due to its adiabatic response. The density has a linear dependence on Φ and an ad-hoc coefficient $\epsilon_{s,\phi}$ governs the response of adiabatic passing particles.

$$N_{s,passing} = -N_{eq,s}(1 - f_T)\left(\frac{q_s}{T_{eq,s}}(\Phi - \epsilon_{s,\phi}\langle\Phi\rangle_\alpha) - 1\right) \tag{2.52}$$

For $\epsilon_\phi = 1$, the passing particles do not react to the zonal potential $\langle\Phi\rangle$, which is constant on a flux surface. Therefore, the zonal flows $\langle\Phi\rangle = \Phi_{\text{ZF}}$ driven by trapped particles can freely grow without any interference of passing particles. In the opposite case $\epsilon_\phi = 0$, the passing particles can respond to the zonal potential according to which the amplitude of zonal flows are strongly suppressed. In the TERESA model, the value of ϵ_ϕ is not computed self-consistently, thus it will be used as a free parameter $0 \leq \epsilon_\phi \leq 1$.

Finally, by inserting Eq.(2.50, 2.52) into Eq.(2.49), one can obtain the final form in the normalized unit (Idouakass et al., 2018)

$$\frac{2}{\sqrt{\pi}}\frac{T_{eq,i}}{T_0}\sum_s\left(q_s\mathscr{C}_s\int_0^{+\infty}\mathcal{J}_{0,s}F_sE^{1/2}dE\right) = \mathcal{C}_{ad}(\Phi - \epsilon_{\phi,s}\langle\Phi\rangle_\alpha) - \mathcal{C}_{pol}\sum_s\mathscr{C}_s\tau_sZ_s^2\Delta_s\Phi \tag{2.53}$$

where $\mathscr{C}_s = N_s/N_{eq}$, $\tau_s = T_{eq,i}/T_s$, $\mathcal{C}_{ad} = \mathcal{C}_{pol}\frac{1-f_T}{f_T}\sum_s(Z_s^2\mathscr{C}_s\tau_s)$, $\int_1^{1-2\epsilon}\frac{d\lambda}{4\bar{\omega}_b} = f_T$, $\mathcal{C}_{pol} = e\omega_0L_\psi/T_0$ with the ion precession frequency $\omega_0 = T_0/(eR_0^2B_\theta)$ and the radial length of the simulation box $L_\psi = aR_0B_\theta$.

When compared to GYSELA, the major advantage of TERESA-4D is that an arbitrary number of particle species can be tackled with a reasonable computation time. Therefore, it is possible to deal with multiple impurities in a single simulation, which might be especially useful for the study of parametric dependencies.

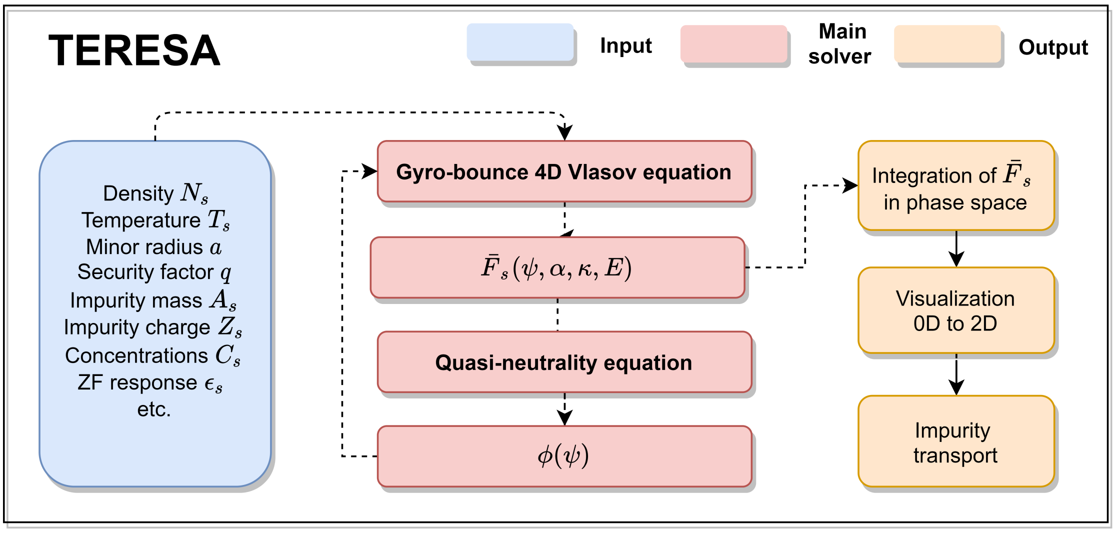

FIGURE 2.5 – Schematic view of TERESA-4D code.

Chapitre 3

Impurity pinch generated by trapped particle driven turbulence

Contents

3.1 Introduction

Central accumulation of heavy impurities in the past and present day devices has renewed interest for the study of neoclassical impurity transport (Ida et al., 1989; Pasini et al., 1992; Rice et al., 2000; Pütterich et al., 2013; Angioni et al., 2014; Loarte et al., 2015; Casson et al., 2015, 2020). It is now a well-known fact that poloidal asymmetry of impurity density driven by plasma rotation (Wong, 1987; Wesson, 1997; Romanelli and Ottaviani, 1998; Fülöp and Helander, 1999; Belli et al., 2014; Maget et al., 2020) or by temperature anisotropies (Ingesson et al., 2000; Reinke et al., 2012; Kazakov et al., 2012; Bilato et al., 2017; Goniche et al., 2017) generated by external heating system, such as ICRH, can enhance or reduce neoclassical impurity transport significantly (Angioni and Helander, 2014).

One of the possible objectives to avoid such core accumulation is to increase turbulent diffusion and reduce the neoclassical convection. Furthermore, in future fusion reactors like ITER, the fraction of NBI heating is expected to be low, and also the specificites of future reactors, such as high temperature and large machine size, will lead to a relatively weak neoclassical regime for impurities. Subsequently, over the last decades, the impact of the turbulent transport, particularly the turbulent convection, has attracted much attention, and some progress has been made in theoretical description (Frojdh et al., 1992; Estrada-Mila et al., 2005; Angioni and Peeters, 2006; Fülöp and Weiland, 2006; Guirlet et al., 2006; Angioni et al., 2007; Bourdelle et al., 2007; Dubuit et al., 2007; Nordman et al., 2008; Camenen et al., 2009; Fülöp et al., 2010; Fülöp and Moradi, 2012; Mollen et al., 2012; Angioni et al., 2012b,a; Skyman et al., 2014). In addition, centrifugal effects (Angioni et al., 2012a), poloidal asymmetry of impurity density (Fülöp and Mordai, 2006), electromagnetic effects (Hein and Angioni, 2010; Moradi et al., 2012) and dependence on the main ions mass (Pusztai et al., 2013), have been investigated both analytically and numerically.

A turbulent transport of impurities can be decomposed into multiple components, such as thermo-diffusion, roto-diffusion and curvature pinch, which can be characterized as off-diagonal transport components (Angioni et al., 2012b). Furthermore, the investigation of parametric dependencies of these terms is a formidable task due to the nonlinear nature of instabilities driven by turbulence. To overcome this, a *quasi-linear* model has been applied in case of ITG (Fülöp et al., 2010) and TEM (Mollen et al., 2013) instabilities. However, these models have been usually tested with their own assumptions for reduced models. Such assumptions sometimes preclude us from clearly apprehending characteristic features of convective velocity. Therefore, more integrated and/or complete models, such as full-F and global gyrokinetic model would be necessary to examine the impact of impurity pinch.

To this end, in this chapter, we investigate the parametric dependencies of impurity pinch driven by trapped particle turbulence using the code TERESA (Depret et al., 2000; Sarazin et al., 2005; Cartier-Michaud et al., 2014; Drouot et al., 2014). More accurately, effects of trapped particle driven mode on turbulent impurity particle flux is studied by means of global non-linear full-F bounce-averaged gyrokinetic code. To restrict our study solely to a turbulent case, only light impurities in collisionless regime will be studied actively. Throughout this chapter, even though each species is treated self-consistently, the concentration of impurity $\mathcal{C}_s$ will be kept at the trace limit, thereby the presence of impurities does not change the nature of the background plasma turbulence. The quasi-linear derivation of pinch terms from a non-linear full-F gyrokinetic model is also presented in this chapter. Especially, the thermo-diffusion and the curvature pinch in trapped ion/electron dominant mode (TIM/TEM) are studied in detail.

3.2 Impurity Pinch

In general, impurity flux can be decomposed into two different parts ; (i) diffusive part which depends on the density gradient and (ii) convective part :

$$\Gamma_z = -D_z \nabla N_z + N_z V_z \tag{3.1}$$

where D_z is a diffusion coefficient and V_z is a convective (pinch) velocity. This seemingly simple equation contains nonlinear turbulent effects in its coefficient D_z and pinch velocity V_z, which make them hard to analyze. One useful way to study such nonlinear evolution of turbulent impurity flux is a quasi-linear theory, in which one assumes a linear response for the transported particles to the fluctuating potential. Particular attention should be paid to the validity of the quasi-linear theory. For instance, the main assumption, the ordering of the characteristic times governing the plasma dynamics, should be verified. Within the framework of quasi-linear theory, an analytical expression of the pinch velocity V_z can be derived and will be presented in Section 3.2.1. In addition, a useful method has been designed in this chapter from nonlinear simulations for the study of the convective part and this method will be introduced in Section 3.2.3.

3.2.1 Quasi-linear impurity transport

Turbulent particle transport can be addressed by means of the quasi-linear model in the framework of weak turbulence. The quasi-linear theory has been already widely addressed by several authors for the purpose of studying turbulent impurity flux (Dubuit et al., 2007; Bourdelle et al., 2007; Futatani et al., 2010). Recently, TERESA code has also shown that particle/heat fluxes obtained from nonlinear simulations were found to be in good agreement with quasi linear predictions (Medina et al., 2018; Gravier et al., 2019). In this section, as an extension of previous work, the quasi linear framework will be applied for impurity flux, and an analytical formula of impurity particle flux will be presented in detail based on the kinetic approach (the fluid approach is also detailed in Appendix A).

First, we recall the Vlasov equation of the bounce-averaged distribution function F derived in Eq.(2.47) :

$$\frac{\partial F}{\partial t} - [\mathcal{J}\phi, F] + \frac{\Omega_d E}{Z}\frac{\partial F}{\partial \alpha} = 0 \tag{3.2}$$

Here, the distribution function F and the electric potential ϕ can be split into perturbed and unperturbed parts with the assumptions $\tilde{F} \ll F_{eq}$ and $\phi_{eq} = 0$.

$$\begin{aligned} F &= F_{eq}(\psi, E, t) + \tilde{F} \\ \phi &= \tilde{\phi} \end{aligned} \tag{3.3}$$

where the Maxwellian distribution function F_{eq} is defined as

$$F_{eq} = \frac{N_{eq}}{T_{eq}^{3/2}} \exp\left\{-\frac{H_{eq}}{T_{eq}}\right\} \tag{3.4}$$

where the equilibrium Hamiltonian $H_{eq} = E(1 + e\Omega_d\psi)$ with $\Omega_d = \omega_d Z_s/E$ and ψ is the dimensionless radial coordinate ($d\psi = -R_0 B_\theta dr$) is used (H_{eq} is differently used in (Gravier et al., 2019) as $H_{eq} = E$).

By assuming small amplitude ($\tilde{F} \ll F_{eq}$) according to which frequency and growth rates of the modes can be described by linear theory, Eq.(3.2) can be rewritten by keeping only first order terms of the perturbed part :

$$\frac{\partial \tilde{F}}{\partial t} - \frac{\partial \mathcal{J}\phi}{\partial \alpha}\frac{\partial F_{eq}}{\partial \psi} + \frac{\Omega_d E}{Z}\frac{\partial \tilde{F}}{\partial \alpha} = 0 \tag{3.5}$$

Now the above equation can be rewritten using the Fourier decomposition $\tilde{F}_s = \sum_n F_n e^{i(n\alpha - \omega t)}$ and $\tilde{\phi} = \sum_n \phi_n e^{i(n\alpha-\omega t)}$ where $\omega = \omega_r + i\gamma$ is composed of the real frequency and the growth rate. It is also important to note that in the framework of quasi-linear theory, the assumption of the distribution function close to the equilibrium Maxwellian is underlined for the validity of model. After some arrangement, we finally find the relationship between the perturbed distribution function and the perturbed potential as follows :

$$F_n = \frac{\kappa_N + \left(\frac{E}{T_{eq}} - \frac{3}{2}\right)\kappa_T - e\Omega_d\frac{E}{T_{eq}}}{\frac{\omega}{n} - \frac{\Omega_d}{Z}E} F_{eq}\mathcal{J}\phi_n \tag{3.6}$$

where $\kappa_N = -\frac{1}{N_{eq}}\frac{dN_{eq}}{d\psi}$, $\kappa_T = -\frac{1}{T_{eq}}\frac{dT_{eq}}{d\psi}$ are the logarithmic density and temperature profile respectively.

By applying spatial averages of Eq.(3.2) over the toroidal angle α ($< . >= \frac{1}{2\pi}\int d\alpha$) and combining it with Eq.(3.5), the above equation can be expressed as :

$$\frac{\partial F_{eq}}{\partial t} = \frac{\partial}{\partial \psi}\left\langle \tilde{F}\frac{\partial \mathcal{J}\phi}{\partial \alpha}\right\rangle \tag{3.7}$$

where we neglected high order terms above the second order. Then, Eq.(3.7) yields :

$$\frac{\partial < N >_{\alpha}}{\partial t} + \frac{\partial \Gamma_z}{\partial \psi} = 0 \tag{3.8}$$

where the final form of impurity transport Γ_z can be written as :

$$\Gamma = \sum_n \int (n\mathcal{J}\phi_n)^2 \frac{\gamma}{\left(\omega_r - n\frac{\Omega_d}{Z}E\right)^2 + \gamma^2}\left[\kappa_N + \left(\frac{E}{T_{eq}} - \frac{3}{2}\right)\kappa_T - e\Omega_d\frac{E}{T_{eq}}\right]F_{eq}\sqrt{E}dE \tag{3.9}$$

The above equation can be summarized into three terms :

$$\frac{\Gamma_z}{N_z} = D_z\kappa_{N_z} + C_T\kappa_{T_z} + C_P \tag{3.10}$$

The first term in Eq.(3.10), proportional to κ_{Nz}, is a diffusive part of the impurity flux. The second term is the thermo-diffusion $C_T\kappa_{Tz}$ which stems from the inherent temperature gradient in tokamak (Weiland et al., 1989; Frojdh et al., 1992). It should be noted that the temperature gradient in the thermo-diffusion term depends on the temperature gradient of the transported species, and not on the temperature gradient which drives the background turbulence. In addition, the sign of coefficient C_T in Eq.(3.10) depends on the phase velocity of the order of any turbulent modes. For example, the direction of thermo-diffusion is directed inwardly when turbulence is propagating in the electron magnetic drift direction while it is directed outwardly when turbulence is propagating in the ion magnetic drift direction (at high κ_{N_z}, TIM modes can reverse frequency). Usually, the magnitude of C_T tends to decrease for high-Z impurities (Angioni and Peeters, 2006; Guirlet et al., 2006; Dubuit et al., 2007). Thus in the case of high charge impurities such as tungsten (W), the effect of thermo-diffusion would decrease significantly.

The last term corresponds to the curvature pinch C_p which is proportional to magnetic field curvature. It originates from the perpendicular compression of $E \times B$ drift velocity. This term is proportional to $\nabla q/q$ (q is the safety factor) leading to an inward direction except for reversed shear plasma (Futatani et al., 2010). Usually, another pinch exists, the parallel compression pinch (Angioni and Peeters, 2006), which is proportional to Z/A where A is the impurity mass number, such that $m_z = Am_H$ and has a direction opposed to thermo-diffusion (Table 3.1). Thus it is inward for ion dominated turbulence and outward for electron dominated turbulence. This term cannot be accounted for in TERESA simulations because the parallel electric force is neglected.

TABLE 3.1 – Impurity pinch direction. Reproduced from (Bourdelle et al., 2007).

	Thermo-diffusion	Curvature pinch
Trapped Ion Mode (TIM)	Outward	Inward
Trapped Electron Mode (TEM)	Inward	(Outward if $s \ll 0$)

3.2.2 Validity of the quasi-linear approximations

Before we move to the main results obtained by nonlinear simulations, it is crucial to discuss the validity of the quasi-linear theory. The two main approximations—(i) a weak fluctuation level ($\delta F \ll F$) and (ii) no trapped particles in the saturated potential field—are often used to justify the validity. The first approximation which is equivalent to the condition where the distribution function F is close to the Maxwellian equilibrium is well satisfied in the core of tokamaks. As a result, the second approximation is often tested for verification.

To demonstrate the second approximation, we introduce a dimensionless number, named the Kubo number $\mathcal{K}$ defined as follows (Kubo, 1963) :

$$\mathcal{K} = \frac{\tau_{ac}}{\tau_f} \tag{3.11}$$

Here, τ_{ac} represents the turbulence auto-correlation time, as experienced from the point-of-view of particles with zero energy. It is defined as $\tau_{ac} = \int \langle \phi(t)\phi(t+\tau)\rangle d\tau / \langle \phi^2(t)\rangle$ where $\langle \phi(t)\phi(t+\tau)\rangle$ is the auto-correlation function of the potential. It is calculated at the location of the maximum saturated potential ϕ_{max} of the simulation box (Figure 3.1). And τ_f is the flight time of a particle along the electric potential structure. The ratio between these two times should be lower than 1 ($\mathcal{K} < 1$) in order that the particles are not trapped in the potential well. In this thesis, an analytical approach to obtain τ_f has been applied by assuming that particles follow a circle trajectory around the maximal electric potential ϕ_{max}.

The flight time τ_f for a particle to travel along the circle can be obtained using the Hamiltonian relation in the angle-action variables $\frac{dJ_3}{dt} = -\frac{\partial H}{\partial \alpha}$ and $\frac{d\alpha}{dt} = \frac{\partial H}{\partial J_3}$ and a simple form of electric potential $\phi = \phi_0 \cos{(n\alpha)} \cos{(k\psi)}$ where each n, k represents the mode number in α, ψ direction and ϕ_0 is the maximal electric potential.

$$\tau_f = \int dt = \int \left(\frac{d\theta}{dt}\right)^{-1} d\theta = \frac{2\pi}{nk\phi_0} \tag{3.12}$$

In Figure 3.2, the Kubo number $\mathcal{K}$ is calculated from TERESA simulations by varying $\kappa_{T_i}, \kappa_{T_e}$ simultaneously and using the most unstable modes n and k obtained in the linear phase. For given plasma parameters ($\kappa_n = 0.1$ and $\kappa_T = 0.05, 0.1, 0.2$ and 0.3),

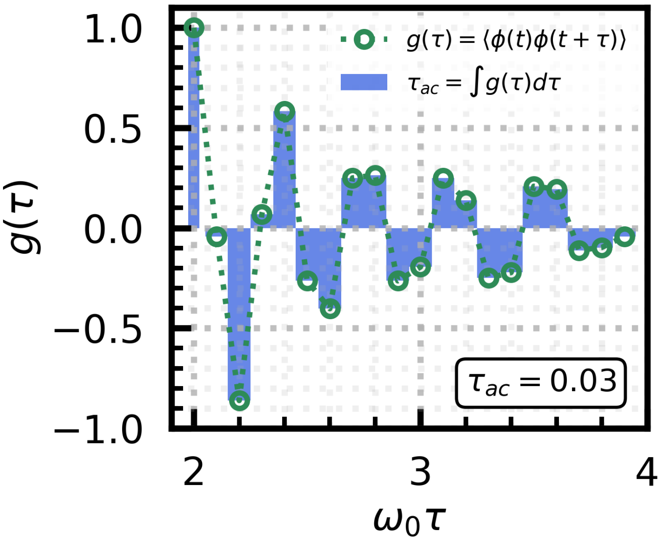

FIGURE 3.1 – Wave-particle interaction time τ_{ac} obtained by an auto-correlation function $g(\tau)$ (normalized to $g(\tau = 2)$) of the electric potential at a location (ψ, α) where $\phi_{\max}$ is obtained during the relaxation state ($2\omega_0^{-1} < t < 4\omega_0^{-1}$). For input parameters, plasma density $\kappa_n = 0.1$ and temperature $\kappa_T = 0.05$ profiles with numerical grids $(N_\alpha, N_\psi, N_\kappa, N_E) = (1024, 256, 1, 96)$ are used. Here, τ_{ac} is equivalent to the surface integral of $g(\tau)$.

the Kubo number $\mathcal{K}$ satisfies the quasi-linear ordering of the characteristic turbulence time. The auto-correlation time τ_{ac} is found to be smaller than the flight time along the turbulence eddy τ_f, which means the particles are not trapped in the saturated potential. The Kubo number tends to increase in case of high temperature gradient κ_T. Note that the method used in (Lim et al., 2020) to calculate the Kubo number was evidenced to overestimate it, sometimes by an order of magnitude (Guillevic et al., prep) . Note also that more work needs to be done to estimate the Kubo number from the point-of-view of resonant particles (with $E \neq 0$).

3.2.3 Pinch velocity from nonlinear numerical simulations

To clarify effects of impurity pinch in the particle flux, it is necessary to separate our numerical impurity flux into diffusive and convective part. Accordingly, it is useful to express Eq.(3.1) as a linear equation of the logarithmic density gradient $\kappa_{Nz} = -\nabla N_z / N_z$ as follows :

$$\frac{\Gamma_z}{N_z} = -D_z \frac{\nabla N_z}{N_z} + V_z = D_z \kappa_{Nz} + V_z \tag{3.13}$$

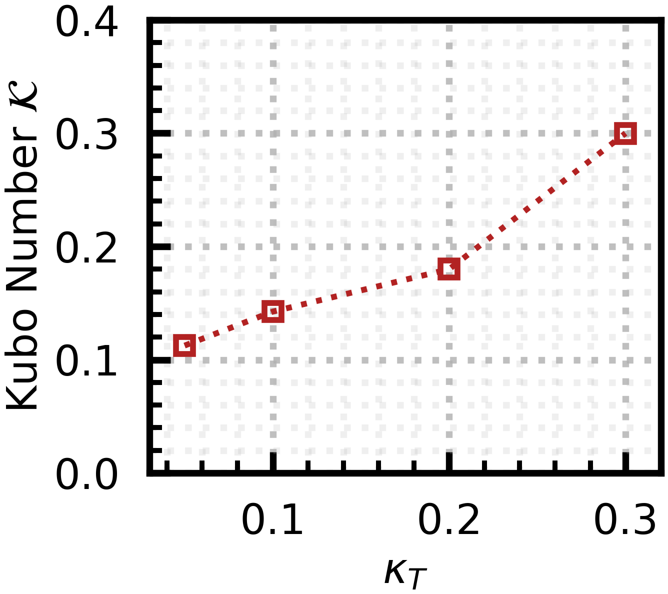

FIGURE 3.2 – The kubo number $\mathcal{K}$ is calculated at a location (ψ, α) where $\phi_{\max}$ is obtained for different background temperature profiles κ_T while density profile is fixed at $\kappa_N = 0.1$.

Given that the impurity particle flux Γ_z and the density gradient κ_{Nz} can be measured from nonlinear numerical simulations, it is possible, if multiple simulations with different values of κ_{N_z} are performed, to calculate an accurate value of V_z from Eq.(3.13).

The shaded part of Figure 3.3 represents the beginning of the turbulent state from nonlinear simulation TERESA, and this region has been selected to extract a steady state value of ∇N_z. In Figure 3.3(a), the time evolution of the 10 most unstable modes ϕ_n is represented. In the first period $0 < t < 2\omega_0^{-1}$ is, the background turbulence is not entirely developed. The following shaded zone $2\omega_0^{-1} < t < 4\omega_0^{-1}$ indicates where turbulence is close to a stationary state. Since we focus mainly on the region where turbulence is already set up, the shaded region will be appropriate to compute the steady state value of ∇N_z. It can be seen in Figure 3.3(b) that the time cumulative Γ_z increases linearly, which means Γ_z has a constant value after $2\omega_0^{-1}$, and this value will be used in Eq.(3.13) to find impurity pinch velocity.

At this stage, special attention needs to be paid when determining the value of $\kappa_{Nz} = -\nabla N_z / N_z$ since the background plasma turbulence can alter the given initial impurity density profile in time. It is described in Figure 3.4 that the value of the impurity density gradient $\kappa_{Nz}^{\text{final}}$ $(t = 2\omega_0^{-1})$ in turbulent regime is no longer identical to the initial impurity density gradient $\kappa_{Nz}^{\text{init}}$ $(t = 0)$. It is therefore necessary to compute the modified $\kappa_{Nz}^{\text{final}}$ value in the turbulent regime. Note that the early turbulent stage

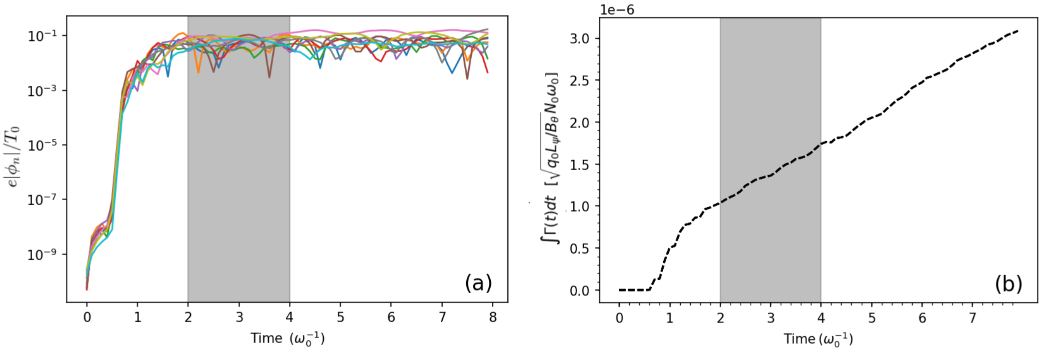

FIGURE 3.3 – (a) Time evolution of the 10 most unstable ϕ_n modes. (b) Cumulative impurity particle flux Γ_z as a function of time. The shaded region represents the beginning of the turbulent regime and this region is chosen for the study of impurity pinch.

$(2\omega_0^{-1} < t < 4\omega_0^{-1})$ was chosen on purpose with the validity of quasi-linear approach in mind. In this stage, the impurity density profile does not reach its saturated shape. In our nonlinear simulations, numerical buffer regions are implemented for the purpose of numerical stability at both edge sides $0 < \psi < 0.15$ and $0.85 < \psi < 1.0$. Consequently, only the core region $0.2 < \psi < 0.8$ will be taken into account for the computation of $\kappa_{Nz}^{\text{final}}$. It should be noted that $\psi = 0$ stands for the core plasma, and $\psi = 1$ for the plasma edge, whereas the opposite convention was sometimes used in previous papers using the same TERESA model for impurity study (Drouot, 2015; Idouakass et al., 2018; Gravier et al., 2019).

By using the value of $\kappa_{Nz}^{\text{final}}$ and the corresponding Γ_z value from the nonlinear simulation, we can plot Γ_z/N_z against $\kappa_{Nz}^{\text{final}}$ and draw a straight line by means of linear regression method. As an example of the method, Figure 3.5 shows that a straight line is drawn using 6 different values of $\kappa_{Nz}^{\text{final}}$ with the corresponding Γ_z impurity flux. The slope of the line is equal to the diffusion coefficient D_z and its x-intercept/y-intercept signifies respectively the peaking factor (PF) $-RV_z/D_z$ and the pinch velocity V_z. According to our notations, positive (negative) peaking factor represents a peaked (hollow) impurity density profile and positive (negative) pinch velocity means particles moving towards the edge (the core).

Finding V_z values using a linear regression method with a restricted number of points $(\kappa_{Nz}, \Gamma_z/N_z)$ provides only an approximate value. It is therefore necessary to run several simulations with various values of κ_{Nz} to increase accuracy of our results.

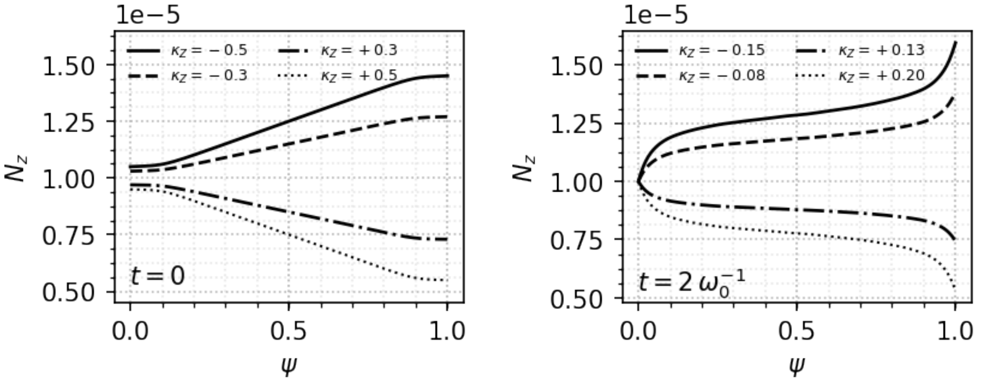

FIGURE 3.4 – Impurity density profiles N_z with different initial values $\kappa_{Nz}^{\text{init}} = \pm 0.3, \pm 0.5$. Initial density profiles at $t = 0$ (left) and measured density profiles at $t = 2\omega_0^{-1}$ (right) are shown. Both radial profiles are measured between $\psi = 0.2$ and $\psi = 0.8$, and normalized with a reference density N_0 at $\psi = 0$.

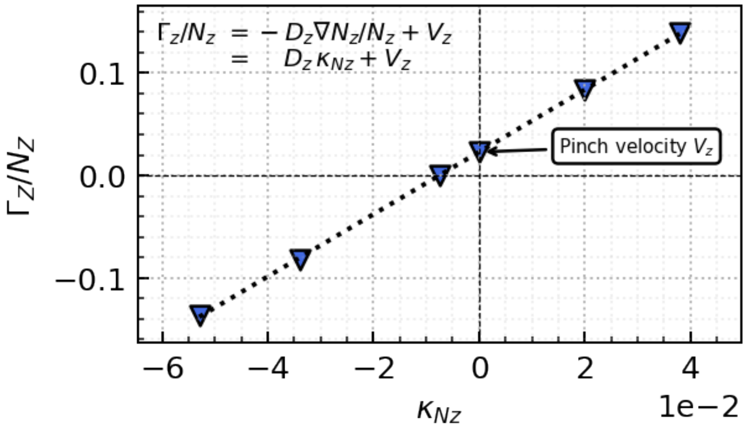

FIGURE 3.5 – Example of linear relationship between density gradient and impurity particle flux. The value of y-interception corresponds to pinch velocity V_z.

3.3 Parametric dependencies of impurity pinch

Determining the complete parametric dependencies of impurity flux by nonlinear gyrokinetic simulations is a formidable task. However, the reduced approach of the bounce-averaged TERESA model by considering only trapped particle species enables us to carry out an in-depth study for local parametric dependencies of convective terms. Among various pinch terms, thermo-diffusion and curvature pinch terms will be covered in detail and their parametric dependencies will be presented in the following section. Note that the parallel compressible pinch plays also an important role in impurity convection (Angioni and Peeters, 2006). However, our approach based on the trapped particle species precludes us from studying the parallel compressible pinch due to the lack of passing particles.

For the results shown in this thesis, the following parameters shown in Table 3.2—the numerical grids $(N_\alpha, N_\psi, N_\kappa, N_E)$, the impurity concentration $\mathcal{C}_z$ and the zonal flows control parameter ϵ_ϕ —are fixed during the entire chapter. The number of grid $N_\kappa = 1$ with $\kappa = 0$ means that we consider strongly trapped particles only.

TABLE 3.2 – Plasma parameters

N_α	N_ψ	N_κ	N_E	$\mathcal{C}_z$	ϵ_ϕ
1024	256	1	96	10^{-5}	0.3

It should be noted that the impurity concentration $\mathcal{C}_z = 10^{-5}$ is kept in the trace limit ($N_z Z^2/N_i \ll 1$), so the presence of impurities doesn't have any impact on the background turbulence. Effects of impurity concentration on impurity transport is also one of the main issues in this field, and recent works regarding the influence on the background turbulence have been recently performed using the TERESA code (Idouakass et al., 2018; Lesur et al., 2020).

3.3.1 Thermo-diffusion

First of all, the thermo-diffusion term $C_T \kappa_{Tz}$ in Eq.(3.10) is studied with respect to impurity charge. In order to study the thermo-diffusion exclusively, the curvature pinch C_p term has been suppressed artificially by putting the modified Hamiltonian $H_{eq,z} = E$ for impurities corresponding to $\Omega_d = 0$ in the distribution function $F_{eq,z}$ as used in (Gravier et al., 2019). The impurity mass number $A = 20$ is chosen while different charge numbers $Z = 2, 4, 8$ and 10 are tested. Initial density and temperature profiles used for TIM/TEM instability are listed in Table 3.3.

For impurity density profiles, 8 different values of $\kappa_{Nz}^{\text{init}} = \pm 0.05, \pm 0.1, \pm 0.3, \pm 0.5$ were chosen and their modified $\kappa_{Nz}^{\text{final}}$ value in turbulent region was used to calculate V_z as we explained in the previous section. To trigger TIM and TEM instabilities independently, different temperature gradients for ions/electrons have been used. With fluid model, it has been already reported in (Dubuit et al., 2007) that the sign of the coefficient C_T depends on the phase velocity of turbulence. It is described in Figure 3.6 that the direction of thermo-diffusion is outward (positive velocity V_z) in the case of TIM

TABLE 3.3 – Initial density/temperature profiles

	κ_{Ni}	κ_{Ne}	κ_{Ti}	κ_{Te}	κ_{Tz}
TIM	0.1	0.1	0.2	0.05	0.05
TEM	0.1	0.1	0.05	0.2	0.05

whereas it is directed inwardly (negative velocity V_z) for TEM dominant case. This direction change can be understood according to the nature of the TIM/TEM. When TIM dominates, the most unstable mode resonates with the H_{eq}/T_{eq} larger than $3/2$ while it is lower than $3/2$ for TEM. According to Eq.(3.9), this different resonant location of the most unstable mode leads to a different direction of V_z. Furthermore, C_T tends to decrease with the charge number Z, which signifies that the effect of thermo-diffusion will be less significant in a high-Z impurity case such as tungsten (W).

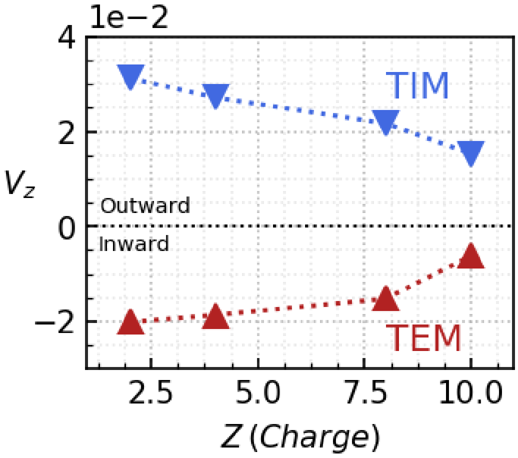

FIGURE 3.6 – Direction of thermo-diffusion and its charge dependency in TIM/TEM dominated plasma for a fixed impurity mass number $A = 20$. The coefficient C_T decreases when the impurity charge Z increases. For TEM, the thermo-diffusion pinch is found to be inward, whereas it is outward in TIM turbulence.

Moreover, it has already been highlighted using fluid model that the direction of impurity particle flux depends directly on the sign of impurity temperature profile κ_{Tz} (Dubuit et al., 2007). To verify this local parametric dependence, the following density/temperature profiles are tested (Table 3.4) :

Five different values of impurity temperature profiles $\kappa_{Tz} = 0.0, \pm 0.1, \pm 0.25$ in the

TABLE 3.4 – Initial density/temperature profiles

	κ_{Ni}	κ_{Ne}	κ_{Ti}	κ_{Te}	κ_{Tz}
TIM	0.1	0.1	0.2	0.05	0.0, ±0.1, ±0.25
TEM	0.1	0.1	0.05	0.2	0.0, ±0.1, ±0.25

TIM/TEM modes have been tested to verify the direction change of thermo-diffusion. According to Eq.(3.10), the impurity particle flux Γ_z is expected to be perfectly diffusive when the impurity temperature profile is flat ($\kappa_{Tz} = 0$) if the curvature pinch is neglected ($C_P = 0$). Figure 3.7(a) shows the relation between the pinch velocity V_z and κ_{Tz} in the TIM/TEM modes. As we outlined before, the pinch velocity disappears when $\kappa_{Tz} = 0$, which signifies that the impurity particle flux is now perfectly diffusive and the direction of V_z is closely related to the sign of κ_{Tz}. A positive value of κ_{Tz} means that the plasma core is hotter than the edge which corresponds to a realistic temperature profile for a future fusion scenario. In this case, the impurity pinch moves inward $(V_z < 0)$ in the TEM mode whereas it moves outward $(V_z > 0)$ in the TIM mode. This direction change according to TIM/TEM instabilities can be explained from Eq.(3.9). A detailed explanation of the thermo-diffusion transport can also be found in (Angioni et al., 2012b).

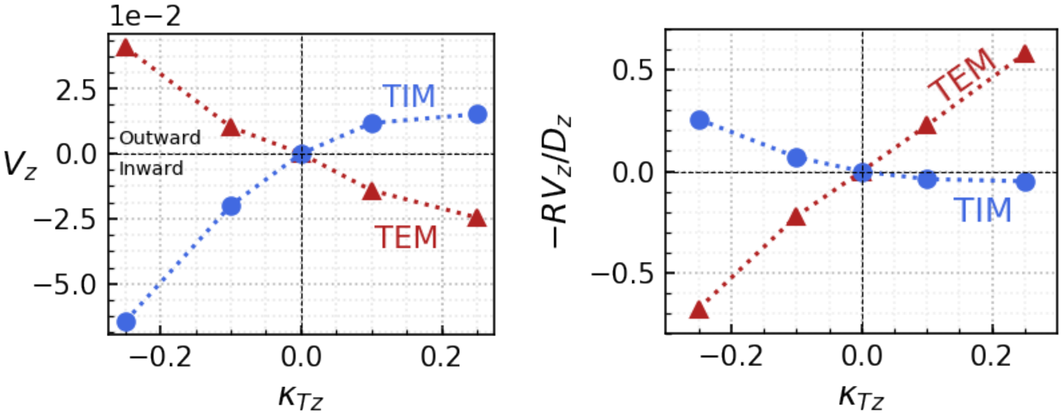

FIGURE 3.7 – Thermo-diffusion V_z (left) and normalized peaking factor $(-RV_z/D_z)$ (right) plotted against κ_{Tz}, for both TEM and TIM turbulent cases.

By introducing a new function $g_n(Z,E)$ from Eq.(3.9),

$$g_n(Z,E) = \frac{\gamma}{\left(\omega_r - n\frac{\Omega_d}{Z}E\right)^2 + \gamma^2}\left(\frac{E}{T_{eq}} - \frac{3}{2}\right)\exp\left\{-\frac{E}{T_{eq}}\right\}\sqrt{E} \tag{3.14}$$

we can rewrite the thermo-diffusion as follows :

$$\sum_n \int_0^\infty (n\mathcal{J}\phi_n)^2 g_n(Z,E)dE \tag{3.15}$$

To see how this term varies with impurity charge Z, we define a new function $X_n(Z) \equiv \int_0^\infty g_n(Z,E)dE$ which integrates g_n over the whole range of energy ; and we will verify how its derivative behaves when impurity charge gets higher.

$$\frac{dX_n(Z)}{dZ} = -\int_0^\infty \frac{2\gamma n\Omega_d\frac{E}{Z^2}\left(\omega_r - n\Omega_d\frac{E}{Z}\right)}{[(\omega_r - n\Omega_d\frac{E}{Z})^2 + \gamma^2]^2}\left(\frac{E}{T_{eq}} - \frac{3}{2}\right)\exp\left\{-\frac{E}{T_{eq}}\right\}\sqrt{E}dE \tag{3.16}$$

Assuming $T_{eq} = 1$ and $\omega_r \gg n\Omega_d$, we can further simplify Eq.(3.16) into

$$\frac{dX_n(Z)}{dZ} = -1.33\frac{2\gamma n\Omega_d\omega_r\frac{1}{Z^2}}{(\omega_r^2 + \gamma^2)^2} \tag{3.17}$$

From the above equation, we can readily see that the absolute value of $X_n(Z)$ decreases with Z in both cases TIM ($\omega_r > 0$) and TEM ($\omega_r < 0$). Note that this relation may fail to apply if the condition $\omega_r \gg n\Omega_d$ is not satisfied. To verify this limit in the case of our numerical simulations, linear analysis has been performed to find the most unstable mode number n and the corresponding values of ω_r, γ according to the plasma parameters.

In Figure 3.9, $X_n(Z)$ is calculated with different impurity charges. The background profiles from Table 3.3 have been used to obtain n, ω_r, γ in linear analysis and $\Omega_d = 1$ is used due to normalization. The values of n, ω_r and γ are displayed in Figure 3.9, and we can clearly see that Eq.(3.17) produces satisfying results in both TIM/TEM cases even though $\omega_r \gg n\Omega_d$ is roughly assured (factor $\simeq 2$). Therefore, the magnitude of thermo-diffusion is found to be decreasing with increasing impurity charge.

Here, the same order of magnitude for TIM/TEM convection is found in Figure 3.7(a). Although the TIM instability plays a minor role in impurity transport compared with other main instabilities, such as ITG and TEM, our investigations must be taken as a qualitative analysis of transition between ion-driven and electron-driven instabilities in general. Furthermore, our model considers only trapped particles where ITG cannot be investigated.

In Figure 3.7(b), the normalized peaking factors (PF) $-RV_z/D_z$ are depicted as a function of κ_{Tz}. Since the PF sign inversely depends on the sign of V_z, PF exhibits the

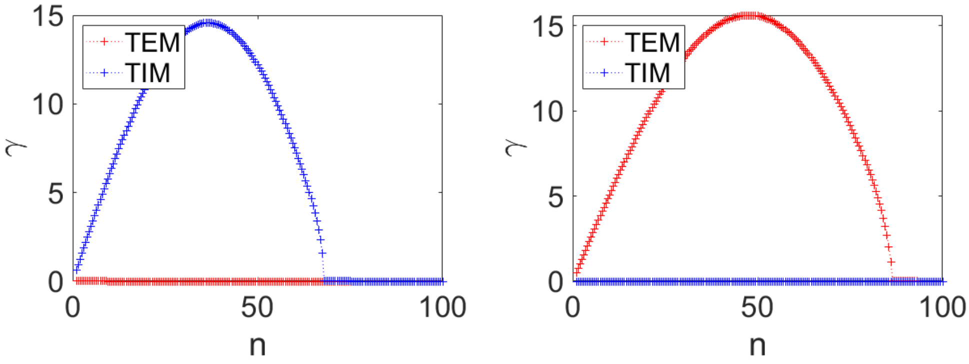

FIGURE 3.8 – Linear analysis in case of TIM/TEM. Linear instability growth rate plotted against the mode n. From these calculations, the values of n, ω_r, γ in TIM/TEM-cases can be found.

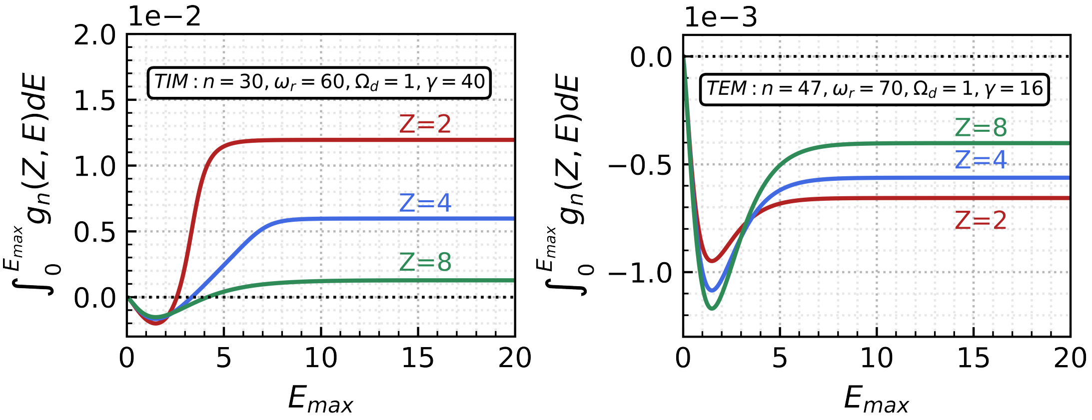

FIGURE 3.9 – Thermo-diffusion contribution $X_n(Z)$ from Eq.(3.17) in case of TIM (left) and TEM (right) using n, ω_r, γ obtained by linear analysis. The thermo-diffusion contribution $X_n(Z)$ decreases with increasing impurity charge.

opposite behavior from V_z. Here, a negative PF signifies hollow impurity density profile and positive PF means peaked impurity density profile, which needs to be avoided for the efficiency of fusion. Consequently, in the general plasma fusion scenario where the core is hotter than the edge (positive $\kappa_{T,z}$ in Figure 3.7), the ion dominant mode would be favorable to mitigate core accumulation in light of turbulent convection, especially by the effect of thermo-diffusion.

Now, we aim to determine the magnitude of the C_T coefficient with respect to the intensity of the background plasma turbulence. Since we are only interested in the absolute value of V_z in connection with to turbulence intensity, ion and electron temperature profiles have been chosen arbitrarily without considering TIM or TEM dominance. Detailed density/temperature profiles are listed below in Table 3.5.

TABLE 3.5 – Initial density/temperature profiles

κ_{ni}, κ_{ne}	κ_{Ti}	κ_{Te}	κ_{Tz}
0.1, 0.15, 0.2, 0.25	0.25	0.25	0.25

While keeping the temperature gradient constant for all species, main ion and electron density gradients have been gradually increased from $\kappa_{Ni} = \kappa_{Ne} = 0.1$ to 0.25. It is shown in Figure 3.10 that the absolute value of V_z increases with the growth rate γ of the most linear unstable mode. The more turbulent is the plasma (larger growth rate γ), the stronger is the pinch velocity. This result corresponds well with our expectation. Because the electric potential ϕ is directly linked to the growth rate γ, a strong background turbulence will enhance both diffusion and convection terms according to Eq.(3.9).

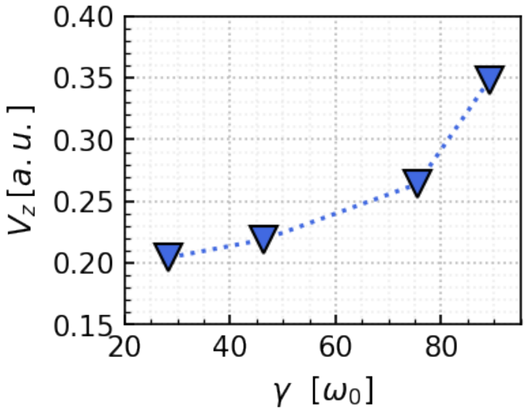

FIGURE 3.10 – Pinch velocity V_z plotted against the linear growth rate γ.

3.3.2 Curvature pinch

In the previous section, the parametric dependencies of the thermo-diffusion term were studied by artificially deactivating the magnetic curvature effects in the Hamiltonian $H_{eq} = E$ of the distribution function. To do likewise for the curvature pinch term, effects of magnetic curvature are now included by employing the entire Hamiltonian $H_{eq} = E(1 + e\Omega_d\psi)$ in the distribution function F_{eq}, while the thermo-diffusion term is artificially suppressed in this section by putting a flat impurity temperature profile $\kappa_{Tz} = 0$.

According to Eq.(2.40), it should be noticed that the precession frequency ω_d is expressed as a function of the trapping parameter κ and the magnetic shear s_0. In general, the sign of ω_d for trapped impurities is mostly positive except for strong negative magnetic shear $(s_0 < 0)$ (Kadomtsev and Pogutse, 1970). This means that, in other words, the effect of curvature pinch term can be readily demonstrated by simply varying the sign of the normalized precession frequency $\Omega_d = \frac{Z_s\omega_{d,s}}{E}$ in Eq.(3.9). In this framework, we introduce an ad-hoc coefficient α in the Hamiltonian, in order to control both the sign and magnitude of the normalized precession frequency Ω_d. The equilibrium Hamiltonian then reads $H_{eq} = E(1 + \alpha e\Omega_d\psi)$. Note that $\alpha > 0$ corresponds to the usual sign of Ω_d for trapped particles, while $\alpha < 0$ represents a strong negative magnetic shear. Then, we use the same linear approach as in Figure 3.5 in order to obtain the pinch velocity. The following density and temperature profiles are tested for numerical simulations with different values of α (Table 3.6) :

TABLE 3.6 – Initial density/temperature profiles

κ_{Ni}	κ_{Ne}	κ_{Ti}	κ_{Te}	κ_{Tz}	α
0.1	0.1	0.2	0.2	0	0, ±0.5

The direction of the curvature pinch velocity V_z with different values of α is depicted on Figure 3.11. As we expected from Eq.(3.9), for the usual sign of precession frequency (positive α), the curvature pinch velocity V_z is directed inward. On the other hand, the strong negative magnetic shear s_0 (negative α) can switch the sign of V_z by pushing the impurity particles toward the edge. The $\alpha = 0$ case corresponds to no magnetic curvature, hence the impurity flux becomes purely diffusive and the linear line Γ_z/N_z passes exactly through the origin point ($V_z = 0$).

Finally, to investigate the impact of α on the magnitude of V_z, we run multiple simulations while keeping α positive. The magnitude of V_z as a function of Ω_d is shown on Figure 3.12. The enhancement of V_z with respect to Ω_d is consistent with our quasi-linear model (Eq.3.9). It should be also noted that the curvature pinch term sometimes prevails over the thermo-diffusion term. But in this work, we focused on the parametric tendency of impurity pinch terms when compared to the thermo-diffusion.

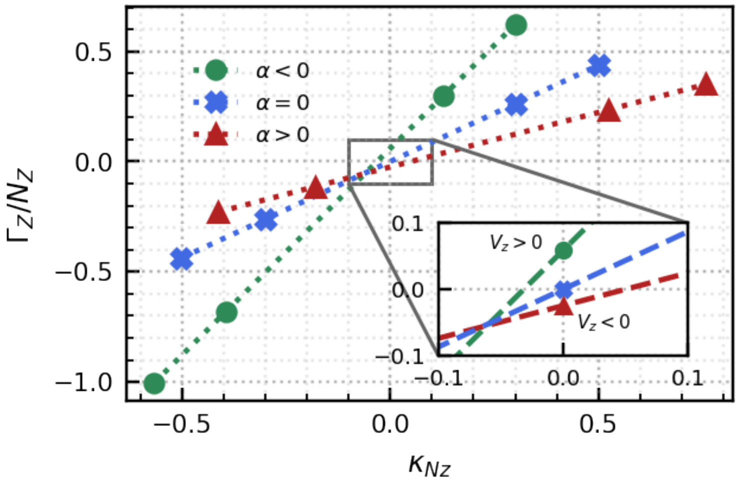

FIGURE 3.11 – Γ_z/N_z plotted against κ_{Nz}, with different values of the ad-hoc coefficient α in $H_{eq} = E(1 + \alpha e\Omega_d\psi)$. The negative value of α represents the strong negative magnetic shear, which drives curvature pinch outwardly. It should be noted that the thermo-diffusion term is artificially suppressed by imposing $\kappa_{Tz} = 0$.

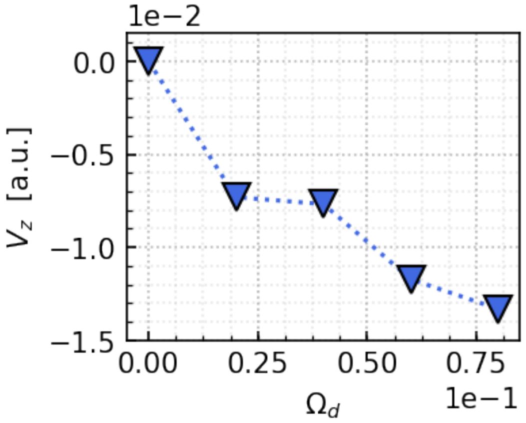

FIGURE 3.12 – Pinch velocity V_z plotted against Ω_d. With α positive, the curvature pinch is directed inward and proportional to Ω_d as we expected from Eq.(3.9).

3.4 Conclusion

In this chapter, the parametric dependencies of impurity pinch—caused by trapped particle driven turbulence—were studied using the bounce-averaged gyrokinetic code

TERESA. Among various terms, the thermo-diffusion and the curvature pinch were treated in detail, and their qualitative behavior was compared with the quasi-linear (QL) model. In order to justify the validity of our approach, the Kubo number was computed, and the quasi-linear approximation is found to be valid in case of a weakly turbulent plasma. The parametric dependencies of convective terms were studied with respect to various parameters such as $\nabla N_{i,e}/N_{i,e}$, $\nabla T_{i,e}/T_{i,e}$, $\nabla T_z/T_z$, impurity charge Z and magnetic shear s_0. For all simulations, light impurities in the trace limit have been kept without assuming any further impurity recombination and ionization.

First of all, the sign of thermo-diffusion coefficient C_T was investigated in TIM/TEM turbulence separately. The results obtained from nonlinear simulations TERESA were in agreement with the previous studies (Guirlet et al., 2006; Dubuit et al., 2007). Furthermore, the QL theory explained that impurities move inward in TEM and outward when TIM is dominant. This can be explained by different energy resonance positions in the case of TIM/TEM. It is also found that the magnitude of C_T tends to decrease with impurity charge Z while the growth rate γ enhances the coefficient C_T.

A more comprehensive understanding of impurity dynamics for further work would require more sophisticated model, including a collision operator, realistic tokamak geometry, magnetic perturbation etc. However, the limited computing performance of the current machine precludes us from reaching this level. In this context, the bounce-averaged gyrokinetic TERESA code allows us more detailed studies about impurity dynamics with a reasonable computation time, and most importantly, these results are in qualitative agreement with our quasi-linear model.

Part of this chapter can also be found in (Lim et al., 2020)

Chapitre 4

Gyrokinetic modelling of light to heavy impurity transport

Contents

4.1 Introduction

Impurity transport is mainly composed of turbulent and neoclassical transport (in the electrostatic limit). And it has been often assumed that the approach of adding two different channels independently provides a reliable framework to compute impurity particle flux. However, recent works have emphasized that the synergy effect between turbulent and neoclassical transport might be non-negligible when background plasma turbulence impacts on the plasma state, which in turn modifies neoclassical transport (Vernay et al., 2012; Estève et al., 2018; Donnel et al., 2019b).

Since the first evidences of central accumulation by neoclassical transport (Connor, 1973; Rutherford, 1973), numerous studies have been conducted to identify the source of such deleterious core accumulation, particularly in connection with the impact of poloidal asymmetries of impurity density (Helander, 1998; Fülöp and Helander, 1999; Angioni and Helander, 2014; Maget et al., 2020). Unlike conventional neoclassical prediction which assumes almost uniform impurity distribution over the flux surface (Hirshman and Sigmar, 1981), a strong poloidal asymmetry has been repeatedly observed in various tokamaks (Lerche et al., 2016; Odstrcil et al., 2016; Goniche et al., 2017) and mounting evidence suggests that accounting for such asymmetry is a crucial key for a predictive model (Casson et al., 2020).

In order to assess these effects coming from both turbulent and neoclassical transport, nonlinear gyrokinetic simulations have been performed with the full-F gyrokinetic code GYSELA (Grandgirard et al., 2016). To this end, a linearized collision operator has been successfully implemented with numerical improvements in terms of energy conservation giving a better agreement with theoretical predictions (Donnel et al., 2019a). Therefore, in this chapter, as an extension of previous work (Donnel et al., 2019a), GYSELA numerical simulations are extended to investigate the impurity transport of various impurities in different collisional regimes—especially, helium (He), argon (Ar) and tungsten (W) representing low, intermediate, high collisional regimes respectively. To achieve this end, turbulent and neoclassical transports in presence of a poloidal asymmetry driven by turbulence are compared with an analytical model in each case and also the effects of poloidal asymmetry on neoclassical transport are investigated.

4.2 Neoclassical impurity flux

In this section, two different analytical descriptions of neoclassical impurity flux are derived with different assumptions. First, neoclassical fluxes are expressed as a function of the CGL-pressure tensor (Chew et al., 1956) assuming weak poloidal asymmetries of the impurity density. The purpose of such derivation is to clarify the main driving terms of neoclassical fluxes i.e. Banana-Plateau (BP) and Pfirsch-Schlüter (PS). Second, a more detailed form of impurity flux is given including the impact of poloidal asymmetries of the density analytically, the effect of which is significant over neoclassical particle fluxes, changing an order of magnitude or even its sign (Angioni and Helander, 2014). This analytical formula will be used for comparison with numerical simulations afterward in Section 4.3. A more detailed derivation of the latter can be found in (Donnel et al., 2019b).

4.2.1 Impurity flux with uniform density distribution

The analytical form of neoclassical impurity flux can be derived from the gyrokinetic equation,

$$\frac{\partial \bar{F}_z}{\partial t} + \frac{1}{B_\parallel^*}\nabla_{\mathbf{z}} \cdot (\dot{\mathbf{z}} B_\parallel^* \bar{F}_z) = \mathcal{C}(\bar{F}_z) \tag{4.1}$$

where $\bar{F}_z$ is the distribution function of impurity and $B_\parallel^* = B + \frac{m_z}{eZ} v_\parallel \mathbf{b} \cdot (\nabla \times \mathbf{b})$ is involved in the volume element in gyrokinetic velocity space and $\mathcal{C}$ is the collision operator.

In steady state, the conservative form of particle flux $\nabla \cdot \mathbf{\Gamma} = 0$ can be obtained by taking the first moment of Eq.(4.1). Splitting the flux as $\mathbf{\Gamma} = \Gamma_\parallel \mathbf{b} + \mathbf{\Gamma}_\perp$, the perpendicular flow can be recast as :

$$\mathbf{\Gamma}_{\perp z} = \mathbf{\Gamma}_{\mathrm{E}} + \mathbf{\Gamma}_{\mathrm{D}} + \mathbf{\Gamma}_{\mathrm{mag}} = N_z \boldsymbol{v}_{\mathrm{E}} + N_z \langle \boldsymbol{v}_{Dz} \rangle - \nabla \times \left[N_z \left\langle \frac{\mu}{Ze} \mathbf{b} \right\rangle \right] \tag{4.2}$$

where $\boldsymbol{v}_E$ is the E × B drift, $\boldsymbol{v}_D$ is the magnetic drift and the magnetization flux $\Gamma_{\mathrm{mag}} = \nabla \times \mathcal{M}_z$ with $\mathcal{M}_z = -\int d^3 v \bar{F}_z \mu \boldsymbol{b}$ is added to account for the correction associated with the cyclotron motion of the particles around its guiding-centre (Brizard and Hahm, 2007) and the bracket is an average over the distribution function.

$$\langle ... \rangle = \frac{1}{N} \int d_3 \boldsymbol{v} \bar{F}_z ... \tag{4.3}$$

Applying an average of the distribution function over the magnetic drift $\boldsymbol{v}_D$ leads to the impurity flux as a function of CGL-pressure tensor. After properly arranging all the terms in Eq.(4.2), one finds an analytical expression of neoclassical particle BP and

PS fluxes (Appendix.B),

$$\langle \mathbf{\Gamma}_{\mathrm{BP}} \cdot \nabla \psi \rangle_\psi = -\frac{I}{Ze} \frac{\langle \boldsymbol{B} \cdot \nabla \cdot \mathbf{\Pi} \rangle_\psi}{\langle B^2 \rangle_\psi} \tag{4.4}$$

$$\langle \mathbf{\Gamma}_{\mathrm{PS}} \cdot \nabla \psi \rangle_\psi = -\frac{I}{Ze} \left\langle (Ne\mathbf{b} \cdot \nabla \phi + \mathbf{b} \cdot \nabla \cdot \mathbf{\Pi}) \left(\frac{1}{B} - \frac{B}{\langle B^2 \rangle_\psi} \right) \right\rangle_\psi \tag{4.5}$$

where $I = RB_\varphi$ is related to the poloidal current that flows through a magnetic surface, $\mathbf{\Pi}$ is the CGL-pressure tensor and the bracket $\langle ... \rangle_\psi$ corresponds to a flux surface average.

The BP flux which is dominant in the long mean free path regime is mainly driven by the pressure anisotropy. The origin of pressure anisotropy is usually due to the magnetic drift driven by non-uniform magnetic field. Since the effect of collisions is less strong than that of the advection in this regime, pressure is not completely isotropized leading to perpendicular flux (Hirshman and Sigmar, 1981). The main driving source of PS flux, conversely, arises from the poloidal variation of the friction force (Hirshman and Sigmar, 1981). In this regime, the contribution of pressure anisotropy vanishes because of strong collisions.

4.2.2 Impurity flux with poloidal asymmetries

Determination of the poloidal variation of impurity flux Γ_z

In what follows, neoclassical impurity flux in presence of poloidal density asymmetry is derived. As it is already treated in the previous section, the total impurity flux from gyrokinetic equation can be written

$$\mathbf{\Gamma}_z = \Gamma_{\parallel z} \mathbf{b} + N_z \frac{\boldsymbol{B}}{B^2} \times \nabla \phi + \frac{\boldsymbol{B}}{ZeB^2} \times \nabla \cdot \mathbf{\Pi} \tag{4.6}$$

Using an axisymmetric notation

$$\begin{aligned} \nabla \phi &= \frac{\partial \phi}{\partial \psi} \nabla \psi + \frac{\partial \phi}{\partial \theta} \nabla \theta \\ \nabla P_{\perp z} &= \frac{\partial P_{\perp z}}{\partial \psi} \nabla \psi + \frac{\nabla P_{\perp z}}{\partial \theta} \nabla \theta \end{aligned} \tag{4.7}$$

Eq.(4.6) can be reformulated as follows :

$$\mathbf{\Gamma}_z = \mathrm{K}_z \boldsymbol{B} - N_z \Omega_z R^2 \nabla \varphi + \frac{\Pi_{\parallel z}}{ZeB} (\mathbf{b} \times \boldsymbol{\kappa}) + \left(N_z \frac{\partial \phi}{\partial \theta} + \frac{1}{Ze} \frac{\partial P_{\perp,z}}{\partial \theta} \right) \frac{\mathbf{b}}{B} \times \nabla \theta \tag{4.8}$$

where $\Pi_{\parallel z} = P_{\parallel z} - P_{\perp z}$ is the pressure anisotropy, $\boldsymbol{\kappa} = -\boldsymbol{b} \times (\nabla \times \boldsymbol{b})$ is the magnetic curvature and we have introduced the following relations :

$$\begin{aligned} \Omega_z &= \frac{\partial \phi}{\partial \psi} + \frac{1}{N_z Z e}\frac{\partial P_{\perp z}}{\partial \psi} \\ \mathrm{K}_z &= \frac{\Gamma_{\parallel z}}{B} + \frac{I}{B^2} N_z \Omega_z \end{aligned} \tag{4.9}$$

In the above equation, $K_z(\psi, \theta)$ is a function of the poloidal angle and a more precise form of it can be obtained from the incompressibility of impurity flow $\nabla \cdot \Gamma_z = 0$. The detailed derivation to find $K_z(\psi, \theta)$ is described in (Donnel et al., 2019b). Here we use the value of $K_z = K_{z0}(\psi) + K_{z1}(\psi, \theta)$ directly from the aforementioned paper.

$$\begin{aligned} K_{z0}(\psi) &= \langle K_z \rangle_\psi \\ K_{z1}(\psi, \theta) &= -\frac{1}{B}\frac{\partial}{\partial \psi}\left(\frac{I \Pi_{\parallel z}}{ZeB}\right) + \left\langle \frac{1}{B}\frac{\partial}{\partial \psi}\left(\frac{I \Pi_{\parallel z}}{ZeB}\right)\right\rangle \end{aligned} \tag{4.10}$$

Link between the friction force $\mathcal{F}$ and K_z

Another analytical form of the neoclassical impurity flux can be derived from the momentum equation by taking its toroidal projection.

$$mN\frac{\partial \boldsymbol{V}}{\partial t} + \nabla \cdot \boldsymbol{\Pi} - eN(\boldsymbol{E} + \boldsymbol{V} \times \boldsymbol{B}) = \boldsymbol{\mathcal{F}} \tag{4.11}$$

where the stress tensor $\boldsymbol{\Pi} = \boldsymbol{P} + mN\boldsymbol{V}\boldsymbol{V}$ and $\boldsymbol{\mathcal{F}} = \int mv\mathcal{C}(f) d^3v$ is the frictional force.

By projecting the above equation in the $R\hat{\varphi}$-direction and applying flux surface average, we can rewrite the above equation as follows :

$$\left\langle R\hat{\varphi} \cdot \frac{\partial (m_z N_z \boldsymbol{V}_z)}{\partial t}\right\rangle + \langle R\hat{\varphi} \cdot \nabla \cdot \boldsymbol{\Pi}\rangle - \langle N_z Z e R\hat{\varphi} \cdot (\boldsymbol{E} + \boldsymbol{V} \times \boldsymbol{B})\rangle = \langle R\mathcal{F}_{\parallel zi}\rangle \tag{4.12}$$

Neoclassical theory for tokamaks usually assumes a steady state ($\partial_t = 0$) and a toroidal axisymmetry ($\partial_\varphi = 0$). Also, the stress tensor $\boldsymbol{\Pi}$ is a small term in neoclassical ordering compared to other components in case of strong collisions, thus it is often neglected. Using the relation $\boldsymbol{B} = I(\psi)\nabla\varphi + \nabla\varphi \times \nabla\psi$ where I is related to the poloidal current inside a magnetic surface and $\hat{\varphi} = R\nabla\varphi$, the particle flux across magnetic surfaces can be derived as follows (Helander and Sigmar, 2005) (the detailed expression of $\mathcal{F}_{\parallel zi}$ is explained in Appendix B.2) :

$$\langle \Gamma_z \cdot \nabla\psi \rangle^{\text{neo}} = -\left\langle \frac{I\mathcal{F}_{\parallel zi}}{ZeB}\right\rangle \tag{4.13}$$

Impurity flux with poloidal asymmetries

Finally, one can find the analytical form of the impurity flux with poloidal asymmetry by properly arranging Eq.(4.10, B.19) and Eq.(4.13). As already done in the previous section, one can divide the total impurity flux into two different channels $\Gamma^{\psi}_{\text{neo}} = \Gamma^{\psi}_{\text{BP}} + \Gamma^{\psi}_{\text{PS}}$.

$$\Gamma_{BP} = -\frac{I}{Ze}\left\langle\frac{B^2}{N_z}\right\rangle_{\psi}^{-1}\left\langle\frac{\boldsymbol{B}\cdot\nabla\theta}{N_z}\left[\frac{\partial P_{\perp z}}{\partial\theta} + B\frac{\partial}{\partial\theta}\left(\frac{\Pi_{\parallel z}}{B}\right)\right]\right\rangle_{\psi} \tag{4.14}$$

$$\begin{aligned}\Gamma_{PS} = \frac{I}{Ze}m_z\nu_{zi}\Bigg\{&\frac{T_i}{e}\frac{I}{L_{\psi,i}}\left(\left\langle\frac{N_z}{B^2}\right\rangle_{\psi} - \left\langle\frac{B^2}{N_z}\right\rangle_{\psi}^{-1}\right) - u\left(\langle N_z\rangle_{\psi} - \frac{\langle B^2\rangle_{\psi}}{\left\langle\frac{B^2}{N_z}\right\rangle_{\psi}}\right)\\ &+\frac{T_iI}{e}\left(\left\langle\frac{N_z}{B^2L_{\psi,z}}\right\rangle_{\psi} - \left\langle\frac{1}{L_{\psi,z}}\right\rangle_{\psi}\left\langle\frac{B^2}{N_z}\right\rangle_{\psi}^{-1}\right) - \left\langle\frac{1}{B}\frac{\partial}{\partial\psi}\left(\frac{I\Pi_{\parallel z}}{ZeB}\right)\right\rangle_{\psi} + \frac{\left\langle\frac{B}{N_z}\frac{\partial}{\partial\psi}\left(\frac{I\Pi_{\parallel z}}{ZeB}\right)\right\rangle_{\psi}}{\left\langle\frac{B_z^2}{N_z}\right\rangle_{\psi}}\Bigg\}\end{aligned} \tag{4.15}$$

where $1/L_{\psi} = 1/L_{\psi,i} + 1/L_{\psi,z}$ with $1/L_{\psi,i} = \partial_{\psi}\ln P_i - \frac{3}{2}\partial_{\psi}\ln T_i$ and $1/L_{\psi,z} = -\frac{1}{T_iZN_z}\partial_{\psi}P_{\perp z}$ and u is the value related to the poloidal velocity of the main ion. In the trace limit of impurities $(N_zZ^2/N_i) << 1$, u can be expressed as

$$u = \left(k_{\text{neo}} - \frac{3}{2}\right)\frac{If_c}{e\langle B^2\rangle_{\psi}} \tag{4.16}$$

where the value of $k_{\text{neo}} \approx 1.17$ is obtained in the limit of large aspect ratio $\epsilon \ll 1$ with the main ion in the banana regime (Fülöp and Helander, 1999). Thus, the following formula $u \approx -0.33\frac{If_c}{e\langle B^2\rangle_{\psi}}$ will be used for further analysis. Here, f_c represents the fraction of circulating particles and can be obtained in a large aspect ratio with circular cross section

$$f_c = 1 - f_t = \frac{3\langle B^2\rangle_{\psi}}{4}\int_0^{\lambda_c}\frac{d\lambda}{\langle\sqrt{1-\lambda B}\rangle_{\psi}} \approx 1 - 1.46\sqrt{\epsilon} \tag{4.17}$$

where $\lambda = \mu/E$ is the pitch angle and $\lambda_c = B_{\text{max}}^{-1}$ is the critical λ for trapping.

Comparing Eq.(4.4, 4.5) with Eq.(4.14, 4.15) shows how an uneven distribution of impurities yields a considerable effect on their flux. Note that the main driving sources for BP/PS fluxes—pressure anisotropy for BP flux and poloidal variation of frictional force for PS flux—are unchanged while additional terms have been added in Eq.(4.15) arisen from the poloidal dependency of $K_{z1}(\psi,\theta)$ in Eq.(4.10). The presence of $\Pi_{\parallel z}$ term in Eq.(4.15) may seem odd at first sight since pressure tends to be isotropic in a highly collisional regime. However, it has been pointed out that even in a high collisional regime, pressure anisotropy can still have an influence on PS flux (Donnel et al., 2019b).

4.3 Numerical results

Various impurities coexist during tokamak discharge, and consequently the main transport channel can be different—turbulent or neoclassical—according to their mass (A) and charge (Z). Thus, the purpose of this section is, first of all, to provide impurity flux of different species in presence of poloidal asymmetries generated by turbulence and to compare them with the analytical models discussed previously. Second, the effect of poloidal asymmetries on impurity transport is investigated in detail. To achieve this end, we selected 3 impurities—helium (Z=2, A=4), argon (Z=18, A=40) and tungsten (Z=40, A=184)—each representing different collisional regimes according to the normalized collisionality ν_a^* (Hirshman and Sigmar, 1981) :

$$\nu_a^* = \frac{\nu_{\text{detrap},a}}{\omega_{b,a}} \approx \frac{qR_0}{\epsilon^{3/2}}\frac{\nu_a}{v_{Ta}} \tag{4.18}$$

$$= \frac{qR_0}{\epsilon^{3/2}}\frac{4\sqrt{\pi}}{3}\frac{e^4 \ln\Lambda}{(4\pi\epsilon_0)^2}\frac{Z_a^2}{T_a^2}\left[n_a Z_a^2 + \sum_{b\neq a}\sqrt{2}n_b Z_b^2 \frac{\left(1+\frac{m_a}{m_b}\right)}{\left(1+\frac{v_{Tb}^2}{v_{Ta}^2}\right)^{3/2}}\right] \tag{4.19}$$

While the main ions are in the banana regime with $\nu_D^* = 0.1$ at mid radius, the relative ratio of the detrapping frequency $\nu_{\text{detrap},a} = \nu_a/2\epsilon$ over the bounce frequency $\omega_{b,a} = \frac{v_{Ta}\sqrt{\epsilon}}{\sqrt{2}\pi qR}$ determines three collisional regimes $-\nu^* \ll 1$ for the banana regime, $1 \ll \nu^* \ll \epsilon^{-3/2}$ for the plateau regime and $\nu^* \gg \epsilon^{-3/2}$ for the Pfirsch-Schlüter regime (Figure 4.1).

For numerical simulations, the parameters on Table 4.1 are chosen for impurities as well as for main ions. With given density and temperature profile for main ions ($R/L_{ni} = 2.2$ and $R/L_{Ti} = 6$), the main instability is the ion temperature gradient (ITG) instability and electrons are treated adiabatically. An isotropic heat source is added close to the inner boundary of simulations (Sarazin et al., 2011), allowing the convergence toward the steady state. Also a Krook operator is applied at the outer boundary region for an artificial damping of the heat flux. Without any further assumptions of ionization or recombination, the impurity concentration was kept in the trace limit ($\mathcal{C}_z = 10^{-6}$) so that the background turbulence is not affected by the presence of impurities. Also, all numerical simulations have been performed in the axisymmetric geometry with concentric magnetic surfaces. The magnetic field is defined as $\boldsymbol{B} = (B_0R_0/R)[\frac{r}{q(r)R_0}\boldsymbol{e}_\theta + \boldsymbol{e}_\varphi]$ where B_0 is the magnetic field on the axis and the safety profile is given as $q(r) = 1.5 + 1.3\left(\frac{r}{a}\right)^{2.5}$. Even though electrons are treated adiabati-

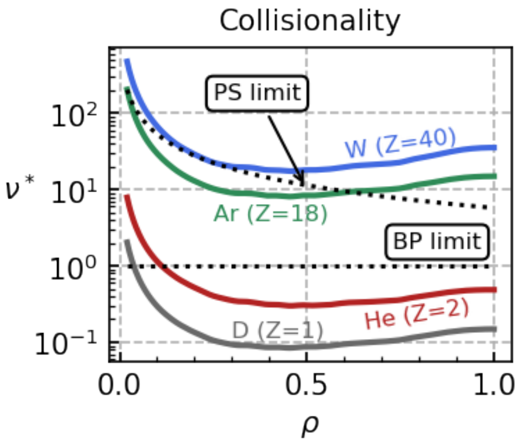

FIGURE 4.1 – Radial profile of collisionality for D, He, Ar and W.

cally, running a simulation with impurity requires considerable computation time since higher resolution is necessary for the impurity Larmor radius ($\rho_z = \frac{1}{Z}\sqrt{\frac{m_z}{m_i}}\rho_i$). To overcome this issue, the same strategy as in (Donnel et al., 2019b) has been applied : (i) the first simulation runs without impurity until turbulence is well developed and steady. At this stage, the numerical grid $(N_r, N_\theta, N_\varphi, N_{v_\parallel}, N_\mu) = (256,\ 512,\ 32,\ 127,\ 64)$ is used for main ions. (ii) once the main ions get to a steady state, the highly resolved numerical grid $(N_r, N_\theta, N_\varphi, N_{v_\parallel}, N_\mu) = (512,\ 1024,\ 32,\ 127,\ 64)$ is used without impurity in order to reorganize the system before adding impurity. (iii) after the reorganization, impurity is put into the simulation with the same numerical grid like previous step.

The physical duration of each simulation lasted sufficiently long for the background turbulence to be well developed and the final stage (iii) of each impurities lasted for sufficiently long time. However, according to the scaling law (ITER Physics Expert Group et al., 1999), the confinement time for impurities to reach the steady state is much longer than the ion confinement time, hence the radial plasma profile of impurities, such as density and temperature, are not completely steady.

4.3.1 Impurity flux with poloidal asymmetry driven by turbulence

By convention, the total impurity flux can be expressed as a sum of two different contributions $\Gamma_{\text{tot}} = \Gamma_{\text{turb}} + \Gamma_{\text{neo}}$. Various approaches have been suggested to define such fluxes properly (Estève et al., 2018). In this work, we adopt the following definitions :

$$< \Gamma_z^{\text{turb}} \cdot \nabla\psi >_\psi = \left\langle \int d^3v \bar{F}_z \bar{v}_E^{n\neq 0} \cdot \nabla\psi \right\rangle_\psi \tag{4.20}$$

TABLE 4.1 – Numerical simulations parameters

Parameters	Normalization
Time step	$\Delta t\omega_{ci} = 16$
Normalized gyroradius	$\rho_* = \rho_i/a = 1/190$
Impurity concentration	$\mathcal{C}_z = 10^{-6}$
Inverse aspect ratio	$\epsilon = a/R_0 = 1/4.4$
Density	$R/L_n = 2.2$
Temperature	$R/L_T = 6$
Magnetic field	$\boldsymbol{B} = \left(\frac{B_0R_0}{R}\right)\left[\frac{r}{q(r)R_0}\boldsymbol{e}_\theta + \boldsymbol{e}_\varphi\right]$
Safety factor	$q(r) = 1.5 + 1.3\exp\{[2.5\log(r/a)]\}$

$$< \Gamma_z^{\text{neo}} \cdot \nabla\psi >_\psi = \left\langle \int d^3v \bar{F}_z(v_{D,s} + \bar{v}_E^{n=0}) \cdot \nabla\psi \right\rangle_\psi \tag{4.21}$$

where n is the toroidal mode number.

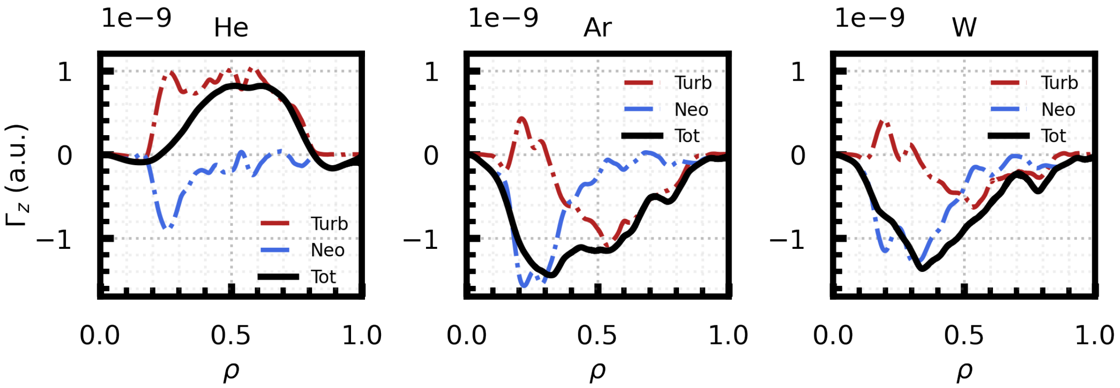

FIGURE 4.2 – Impurity fluxes of different impurities in presence of poloidal asymmetries obtained by numerical simulations GYSELA. Total impurity flux (black solid line) is separated into a turbulent part (red dashed line) and a neoclassical part (blue dashed line).

The impurity fluxes, averaged out over $4000\omega_{ci}$, are shown respectively on Figure 4.2 where the black solid line stands for the GYSELA numerical flux which is the sum of the turbulent flux (red dashed) and the neoclassical flux (blue dashed).

Qualitative differences between species are clearly observed on Figure 4.2. For Helium, the dominant flux is mainly coming from turbulent transport flowing outward from the core (positive Γ_z) except in the region $\rho \sim 0.3$ where the peak of neoclassical flux is presumably produced by poloidal density asymmetry. These results fit well with our prior expectation that helium, as a light impurity, is in the banana regime (Figure 4.1) where collisional effects are small when compared to turbulent fluxes. Also, the outward flow of impurity usually gives rise to a hollow density profile in Figure 4.3, in which He impurity density keeps decreasing along the time at $\rho = 0.3$. In recent works (Bonanomi et al., 2018; Kappatou et al., 2019; Manas et al., 2020), it was experimentally and numerically observed that light impurities, such as helium and boron, are less dangerous than heavy impurities for core accumulation since, particularly in the conditions of ITG dominated regime and high NBI fraction, the outward thermo-diffusion and roto-diffusion terms are dominant.

The neoclassical contribution to the total impurity flux becomes larger when considering higher Z impurities : in the simulations we have performed, it is significant for argon and tungsten. Argon, whose collisionality is extended mostly over the Plateau region (Figure 4.1), shows two distinct regions where the total flux (black solid line) is roughly aligned (i) with neoclassical flux ($\rho < 0.3$) and (ii) with turbulent flux ($\rho > 0.5$). In terms of magnitude, turbulent flux is comparable to neoclassical flux giving nearly equal contributions to the total flux. Unlike helium, argon generates an inward flux (Γ_z negative) leading to accumulation in the core in Figure 4.3, in which Ar impurity density keeps increasing at $\rho = 0.3$.

For tungsten, the heaviest of the analyzed impurities, turbulent flux is reduced by a factor of 2 while neoclassical transport still exerts an important effect in the core. The overall impurity flux is directed inward driving its core accumulation due to neoclassical convection (Figure 4.3). A large number of experimental cases have already confirmed the core accumulation (Meyer et al., 2019; Joffrin et al., 2019; Park et al., 2019) and recent studies have proposed that a proper use of additional heating system might mitigate such accumulation by reducing the neoclassical convection and increasing the turbulent diffusion (Angioni and Helander, 2014; Casson et al., 2020). In this work, no additional heating systems are used except for the heat source on the main ion species.

A comparison of the neoclassical contribution between numerical flux (blue dashed) and semi-analytical model (grey solid) from Eq.(4.14, 4.15) is depicted on Figure 4.4. A special attention has to be paid at this point with respect to how our analytical formula is applied numerically. Unlike other works which use a solution of drift-kinetic equation (NEO (Belli et al., 2012)) or a moment approach (NCLASS (Hirshman and Sigmar, 1981; Houlberg et al., 1997)), here we make direct use of GYSELA numerical data to estimate the neoclassical flux, which means every term in Eq.(4.14, 4.15) is substituted at each time step to obtain neoclassical transport. The goal is to provide direct test of the analytical formula

It is clearly shown on Figure 4.4 that for all impurities, the analytical expressions including poloidal asymmetry of impurity density reproduce satisfying results with

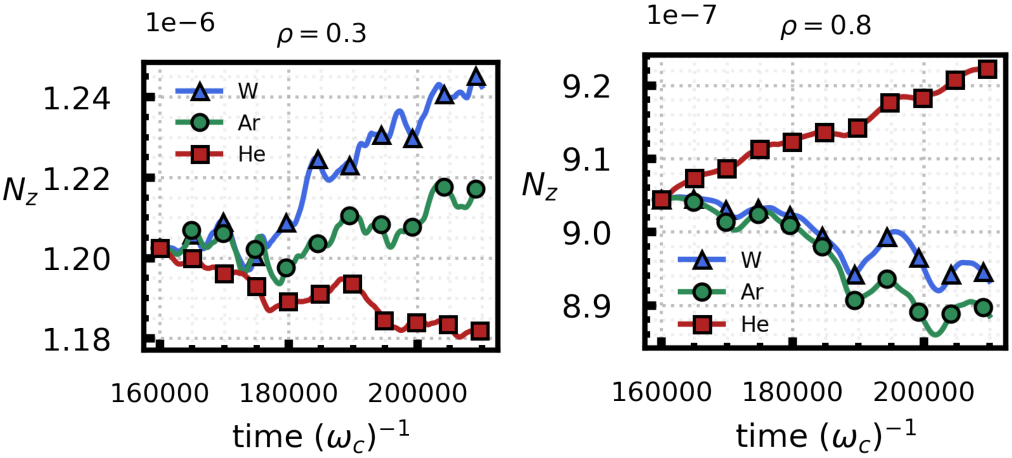

FIGURE 4.3 – Time evolution of impurity density in the core (left) and at the edge (right).

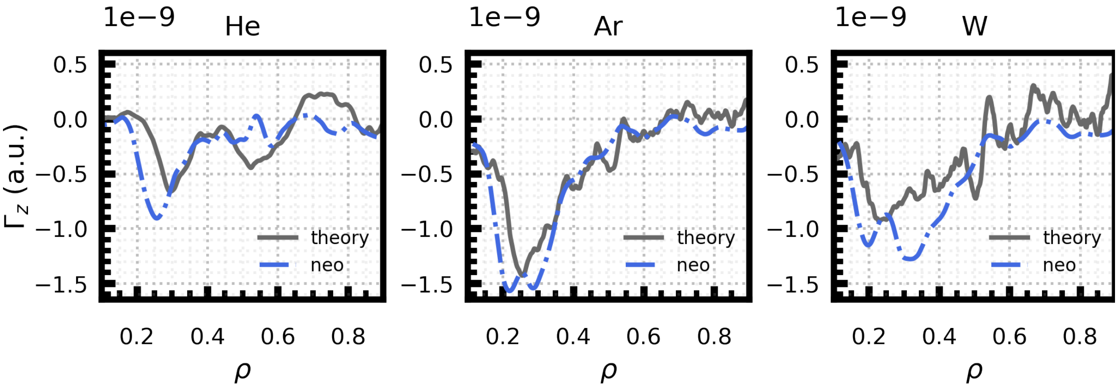

FIGURE 4.4 – Comparison of neoclassical flux between numerical simulations GYSELA (blue dashed line) from Eq.(4.21) and semi-analytical model (grey solid line) from Eq.(4.14) and Eq.(4.15). Every single component in Eq.(4.14, 4.15) was calculated from non-linear GYSELA simulations, for instance density N, temperature T and pressure $P_\perp, P_\parallel$ are computed from the GYSELA distribution function. The difference between two fluxes can be attributed to the assumptions made in Eq.(4.14, 4.15) which are based on purely neoclassical approach, such as Eq.(4.16, 4.17) while our simulations are also in turbulent regime.

our gyrokinetic simulations. The neoclassical flux is directed inward for all impurities due to the inward neoclassical convection driven by main ion density profile. In agreement with our previous results, helium generates a weaker neoclassical flux compared to other impurities. It is further instructive to analyze the neoclassical flux in detail by splitting its components.

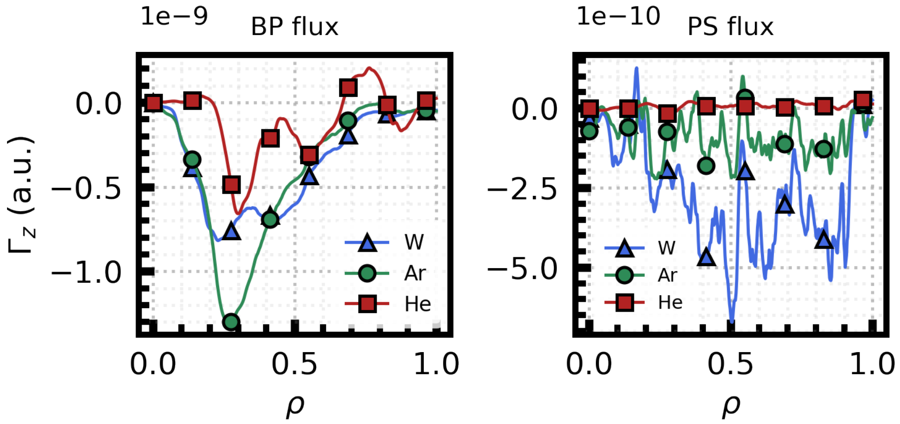

FIGURE 4.5 – Banana-Plateau (BP) flux and Pfirsch-Schlüter (PS) flux for different impurity species, calculated from numerical simulations GYSELA using Eq.(4.14, 4.15).

On Figure 4.5, the radial BP, PS fluxes are calculated from the numerical simulations GYSELA using the analytical formula Eq.(4.14, 4.15). As expected, tungsten produces the most important PS flux compared to other impurities due to its high collisionality while the PS flux coming from helium is almost negligible. For BP fluxes, argon whose collisionality is extended over the plateau region produces a stronger BP flux than for the other species. Moreover, helium in the banana regime starts to generate a BP flux.

4.3.2 Poloidal asymmetry driven by background turbulence

A number of studies have pointed out the inhomogeneity of impurity density over flux surfaces can strongly modify the neoclassical transport (Romanelli and Ottaviani, 1998; Fülöp and Helander, 1999; Angioni et al., 2015) while its impact on turbulent transport seems less significant (Casson et al., 2015). Although there are many factors which can trigger poloidal asymmetry, in this chapter, we restrict ourselves to the poloidal asymmetry driven by turbulence only. The poloidal asymmetries generated by turbulence are expected to be larger for high-Z impurity since the response to the electric potential is Boltzmann-like, thus it is proportional to impurity charge. According to Eq.(4.15), PS flux is mostly driven by poloidal variation of frictional force which is a function of impurity density N_z from Eq.(B.19). Therefore, it is straightforward that PS flux is modified through the poloidal asymmetry and its effect is stronger in case of heavy impurities—tungsten, in this work. This fact is well shown on Figure 4.6 in which the perturbed density $\tilde{N}_z = \frac{N_z - \langle N_z \rangle_\psi}{\langle N_z \rangle_\psi}$ of different impurities are presented on the poloidal section. As expected, tungsten shows the strongest poloidal asymmetry ($\sim 20\%$) while helium presents a very weak asymmetry ($\sim 3\%$). Such asymmetry of

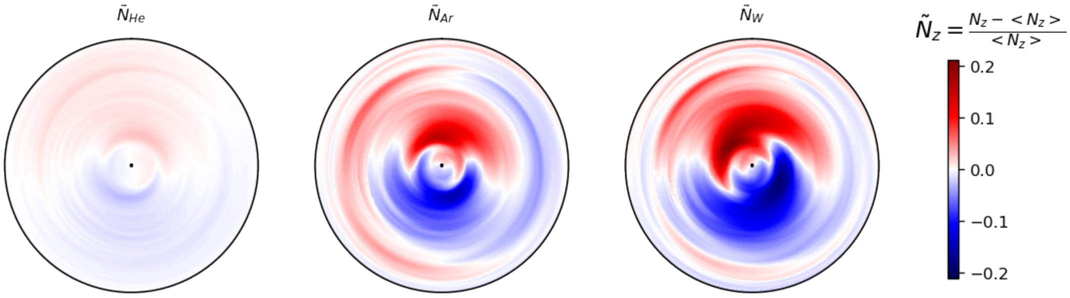

FIGURE 4.6 – Poloidal asymmetries of impurity density given by numerical simulations performed with GYSELA, for helium (left), argon (center), and tungsten (right).

impurity density can be expressed as $N_z(\psi,\theta) = N_z(\psi)[1 + \delta\cos\theta + \Delta\sin\theta]$ where δ and Δ represent *'in-out'* and *'up-down'* asymmetry respectively. According to (Angioni and Helander, 2014), it is usually an *'in-out'* asymmetry which plays an important role on neoclassical transport since the geometrical factor in Eq.(4.15) (corresponding to P_A, P_B in Eq.(4.23)) can be recast as a function of δ and Δ and the *'up-down'* asymmetry Δ appears only as a second order term in impurity flux.

$$\begin{aligned} \frac{\langle B^2\rangle_\psi}{\langle N_z\rangle_\psi}\left[\left\langle\frac{N_z}{B^2}\right\rangle_\psi - \left\langle\frac{B^2}{N_z}\right\rangle_\psi^{-1}\right] &= 2\epsilon(\epsilon+\delta) + \frac{\delta^2+\Delta^2}{2} \\ \frac{\langle B^2\rangle_\psi}{\langle N_z\rangle_\psi}\left[\frac{\langle N_z\rangle}{\langle B^2\rangle_\psi} - \left\langle\frac{B^2}{N_z}\right\rangle_\psi^{-1}\right] &= \epsilon\delta + \frac{\delta^2+\Delta^2}{2} \end{aligned} \tag{4.22}$$

However, poloidal asymmetry driven by turbulence tends to generate an *'up-down'* asymmetry (Fig.4.7) through poloidal convective cells (Donnel et al., 2019c). Such an *'up-down'* asymmetry would be less dramatic than neoclassical 'in-out' asymmetries and their different impact has been already treated in (Fülöp and Helander, 1999).

Poloidal asymmetry affects neoclassical transport, but it can also change the so-called *thermal screening factor* $\mathrm{H}_{\mathrm{neo}}$. As the name suggests, this term related to the main ion temperature profile L_{Ti} prevents impurities from accumulating in the core. Derived from the main ion parallel heat flux in neoclassical theory, the factor is usually equal to $\mathrm{H}_{\mathrm{neo}} \simeq -\frac{1}{2}$ when the main ion is in the banana regime (Hirshman and Sigmar, 1981), but this screening term is also susceptible to be modified by poloidal asymmetry. To clarify this mechanism, it is helpful to rewrite Eq.(4.15) in a different way, as it was

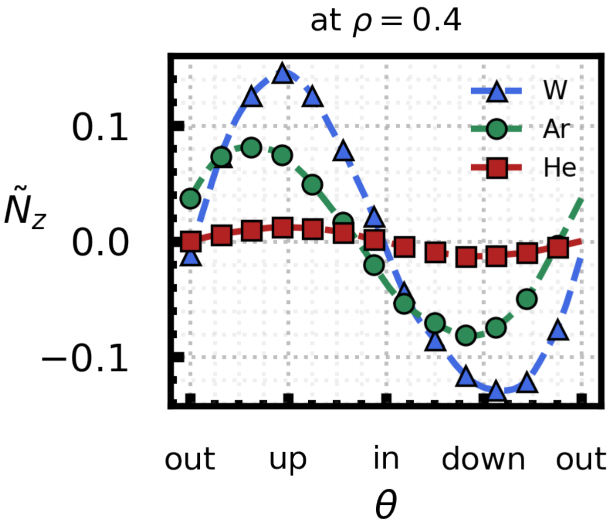

FIGURE 4.7 – Impurity density distribution as a function of the poloidal angle given by the numerical simulations performed with GYSELA.

done in (Angioni et al., 2015) :

$$\begin{aligned} R\langle \Gamma_Z^{\text{neo}} \cdot \nabla\psi \rangle_\psi &\propto \left[-\frac{R}{L_{ni}} - \text{H}_{\text{neo}} \frac{R}{L_{Ti}} + \frac{1}{Z}\frac{R}{L_{nz}} \right] \\ &\propto \left[\left(-\frac{R}{L_{ni}} - \text{H}_{\text{sym}} \frac{R}{L_{Ti}} + \frac{1}{Z}\frac{R}{L_{nz}} \right) P_A - 0.33 P_B f_c \frac{R}{L_{Ti}} \right] \end{aligned} \tag{4.23}$$

where $\text{H}_{\text{neo}} = \text{H}_{\text{sym}} + 0.33\frac{P_B}{P_A} f_c$ with the factor $\text{H}_{\text{sym}} = -\frac{1}{2}$ in the absence of poloidal asymmetries. This factor appears in the expression of $\frac{1}{L_{\psi,i}} = \frac{\partial \ln N_i}{\partial \psi} + \text{H}_{\text{sym}} \frac{\partial \ln T_i}{\partial \psi}$ in Eq.(4.15).

In this equation, the second term corresponds to the thermal screening term and f_c is the fraction of passing particles. The geometrical factors P_A, P_B quantify the impact of poloidal asymmetry, defined as follows :

$$\begin{aligned} P_A &= \frac{1}{2\epsilon^2} \frac{\langle B^2 \rangle_\psi}{\langle N_z \rangle_\psi} \left[\left\langle \frac{N_z}{B^2} \right\rangle_\psi - \left\langle \frac{B^2}{N_z} \right\rangle_\psi^{-1} \right] \\ P_B &= \frac{1}{2\epsilon^2} \frac{\langle B^2 \rangle_\psi}{\langle N_z \rangle_\psi} \left[\frac{\langle N_z \rangle}{\langle B^2 \rangle_\psi} - \left\langle \frac{B^2}{N_z} \right\rangle_\psi^{-1} \right] \end{aligned} \tag{4.24}$$

Eq.(4.23) reveals that the non-uniform distribution of impurities can modify the neoclassical flux or even reduce the temperature screening term by facilitating the accumulation of impurities at the core. From Eq.(4.24), it readily appears that, if the impurity density is uniform over flux surfaces, i.e. if $\langle N_z \rangle = N_z$, then $P_A = 1$ and $P_B = 0$. In this case, standard neoclassical results are recovered. The radial profiles of P_A, P_B for different impurities are presented in Figure 4.8, where the outer regions $\rho < 0.1$ and $\rho > 0.9$ are excluded to mitigate artificial dissipation in buffer region. Although external heating systems are absent in our cases, the background turbulence generates a poloidal asymmetry of density and it is strongly enhanced for W due to its high charge and heavy mass. The impact of poloidal asymmetry on the thermal screening is depicted on Figure 4.9. The theoretical prediction of neoclassical fluxes in two different cases : (i) with the thermal screening without any poloidal assymetry $\mathrm{H_{sym}} = -\frac{1}{2}$ (red solid line) and (ii) without the thermal screening $\mathrm{H_{sym}} = 0$ (green solid line) are compared with the neoclassical flux obtained from GYSELA simulation (blue dashed line). The effect of $\mathrm{H_{sym}}$ on impurity transport can be easily understood by looking at the relative magnitude of each flux. When the thermal screening effect is removed $\mathrm{H_{sym}} = 0$, the neoclassical flux shows a strong inward flux, leading to the strong core accumulation, while the accumulation is mitigated in the case of thermal screening ($\mathrm{H_{sym}} = -\frac{1}{2}$), as expected.

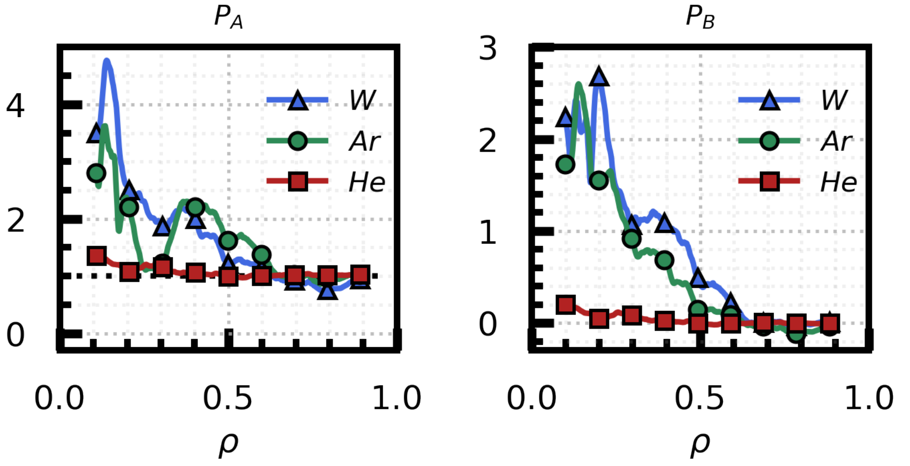

FIGURE 4.8 – The radial profile of geometrical factors P_A (left), P_B (right) without any external heating system.

In overall radius, GYSELA reproduces a value close to the theoretical prediction except in the region $0.1 < \rho < 0.5$. The main reasons of such difference can be summarized as follows. First, the effect of poloidal asymmetries driven by turbulence can reduce the thermal screening effect through the geometrical factor P_B in Eq.(4.23). Second, the term u in Eq.(4.15), linked with the poloidal rotation of the main ion, is calculated in the neoclassical case only, thus the value of k_{neo} in Eq.(4.16) differs from the neoclassical prediction ($k_{\mathrm{neo}} \sim 1.17$) due to the turbulence.

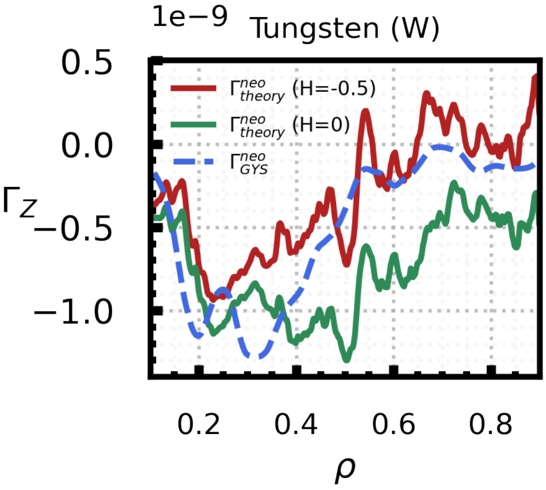

FIGURE 4.9 – Neoclassical impurity flux of tungsten from the theoretical predictions Eq.(4.14,4.15) with two different values of $\mathrm{H_{sym}}$. With the thermal screening $\mathrm{H_{sym}} = -\frac{1}{2}$ (red solid line) and without the thermal screening $\mathrm{H_{sym}} = 0$ (green solid line). For comparison, the neoclassical impurity flux from GYSELA is also depicted (blue dashed line).

4.4 Conclusion

In this chapter, numerical modelling of turbulent and neoclassical transport has been done with various impurities—He, Ar and W—using the full-F gyrokinetic code GYSELA. Our results demonstrate that the main dominant particle flux and its direction depend sensitively on the type of impurities. Most of light impurity (He) transport is due to turbulence while heavy impurity (W) transport is dominated by neoclassical effects. Moreover, the main two driving terms for neoclassical flux—BP, PS fluxes—have been investigated. For He, both BP and PS fluxes are found to be small due to its low collisionality. In contrast, significant inward BP and PS fluxes are generated for Ar and W leading to core accumulation.

In the absence of additional heating system, such as NBI and ICRH, we have also verified that the poloidal asymmetry driven by turbulence can modify the neoclassical particle flux and its impact becomes significant in case of heavy impurities. Furthermore, these strong asymmetries for heavy impurities reduce the thermal screening factor which facilitates the deleterious core accumulation. The neoclassical flux given by our analytical model is shown to be in good agreement with our numerical simulations and GYSELA reproduces the thermal screening factor close to the theoretical prediction $\mathrm{H_{sym}} \simeq -\frac{1}{2}$ in the region where poloidal asymmetries induced by turbulence are small ($\rho > 0.5$).

The overall inward flux for heavy impurities observed in this chapter has already been reported in different tokamaks. To avoid such core accumulation, a proper use of ICRH/ECRH near magnetic axis is necessary. The impact of toroidal rotation on impurity transport is investigated in the next chapter.

Part of this chapter can be also found in (Lim et al., 2021))

Chapitre 5

Effects of toroidal rotation on impurity transport

Contents

5.1 Introduction

During a plasma discharge, toroidal rotation can be intrinsically generated or externally from NBI heating system. It is well known that the centrifugal force driven by toroidal rotation can generate a significant *'in-out'* poloidal asymmetry, which leads to an enhancement of neoclassical transport. In contrast, the impact of such poloidal asymmetry on turbulent transport was found to be much smaller than on neoclassical transport (Casson et al., 2015). However, the presence of a turbulent roto-diffusion, i.e., a radial flux due to the presence of a radial gradient of the toroidal rotation, can play an important role in case of a strongly rotating plasma. Its magnitude even can match the diffusive flux, especially for heavy impurities (Camenen et al., 2009).

A non-negligible impact of strong toroidal rotation on both turbulent and neoclassical impurity transport has already been presented in (Angioni et al., 2014; Casson et al., 2015). The main approach therein was to calculate each transport channel independently ; (i) turbulent transport through the gyrokinetic formulation in the toroidally co-moving frame (GKW) and (ii) neoclassical transport by means of Hinton ordering (Hinton and Wong, 1985), but without considering frictional effects at the lowest order (NEO) (Belli et al., 2014).

In this chapter, as an extension of Chapter 4, the direct impact of toroidal rotation on turbulent and neoclassical impurity transport for tungsten (W), in connection with a poloidal asymmetry, is investigated (Section 5.2) by means of the full-F gyrokinetic code GYSELA (Grandgirard, 2016). To this end, adjustable heat and momentum sources are employed (Sarazin et al., 2011), allowing the self-consistent investigation of both turbulent and neoclassical transports in the laboratory frame including frictional and synergetic effects as well. Section 5.2 outlines the theoretical effects of toroidal rotation on poloidal asymmetries and impurity transport and section 5.3 presents numerical results obtained from nonlinear simulations performed with GYSELA.

5.2 Theoretical approach

In GYSELA, the injection of heat and toroidal momentum can be accomplished by employing adjustable source terms $\mathcal{S}$ in the gyrokinetic Vlasov equation (Sarazin et al., 2011) :

$$\frac{\partial \bar{F}_s}{\partial t} + \frac{1}{B_\parallel^*}\nabla_{\mathbf{z}} \cdot (\dot{\mathbf{z}} B_\parallel^* \bar{F}_s) = \mathcal{C}(\bar{F}_s) + \mathcal{S}_{\text{heat}} + \mathcal{S}_{\text{mom}} \tag{5.1}$$

where $\bar{F}_s$ is the gyro-averaged distribution function for species s, $B_\parallel^* = B + \frac{m_s}{eZ_s} v_\parallel \mathbf{b} \cdot (\nabla \times \mathbf{b})$ is the volume element in gyrokinetic velocity space, $\mathcal{C}(\bar{F}_s)$ is the collision operator and $\mathcal{S}_{\text{heat}}$, $\mathcal{S}_{\text{mom}}$ (defined in Eq.(2.36) and Eq.(2.37)) represent the heat and toroidal momentum sources respectively.

5.2.1 Distribution function with toroidal rigid rotation

According to the neoclassical theory, developed in (Hinton and Wong, 1985; Wong, 1987), at the lowest order in $\delta = \rho_{pi}/L$ where ρ_{pi} is the poloidal ion Larmor radius and L is the radial length scale, the distribution function is Maxwellian, and both the temperature $T_{eq}(\psi)$ and toroidal rotation frequency $\omega(\psi)$ are flux functions, which are constant on magnetic flux surfaces.

$$F_M = N_{eq}(\psi,\theta)\left(\frac{m}{2\pi T_{eq}(\psi)}\right)^{3/2}\exp\left\{-\frac{mu^2}{2T_{eq}(\psi)}\right\} \tag{5.2}$$

with $\boldsymbol{u} = \boldsymbol{V} - \boldsymbol{V}_0$ the velocity in the moving reference frame $\boldsymbol{V}_0$, and $\boldsymbol{V}$ is the velocity of particles in the reference frame. However, the density $N_{eq}(\psi,\theta)$ is not a flux function due to the centrifugal force (Hinton and Wong, 1985).

$$N_{eq}(\psi,\theta) = N_0(\psi)\exp\left\{-\frac{eZ\phi}{T_{eq}(\psi)} + \frac{m\omega^2(R^2 - R_0^2)}{2T_{eq}(\psi)}\right\} \tag{5.3}$$

where e is the positive elementary charge. Inserting the above equation Eq.(5.3) into the Maxwellian function Eq.(5.2) reads :

$$F_M = N_0(\psi)\left(\frac{m}{2\pi T_{eq}(\psi)}\right)^{3/2}\exp\left\{-\frac{H}{T_{eq}(\psi)}\right\} \tag{5.4}$$

where

$$H = \frac{1}{2}mu_\parallel^2 + \mu B + eZ\phi_0(\psi) + eZ\tilde{\phi}_1(\psi,\theta) - \frac{m\omega^2(R^2 - R_0^2)}{2} \tag{5.5}$$

The electric potential on the magnetic surface is approximately equipotential $\phi \simeq \phi_0(\psi)$. In a rotating plasma, however, ions are pushed towards the outboard region due to the centrifugal force. Consequently, an equilibrium electric potential $\tilde{\phi}_1(\psi,\theta)$ is set up to ensure the quasi-neutrality constraint in the presence of centrifugal forces.

$$\tilde{\phi}_1 = \frac{\omega^2}{2}\frac{m_i}{e}\frac{T_e}{T_i + Z_i T_e}(R^2 - R_0^2) \tag{5.6}$$

Therefore, the density distribution in a toroidally rotating plasma can be written as :

$$N_{eq}(\psi,\theta) = N_0(\psi)\exp\left\{-\frac{eZ\phi_0(\psi)}{T_{eq}(\psi)} - \frac{eZ\tilde{\phi}_1(\psi,\theta)}{T_{eq}(\psi)} + \frac{1}{2}\frac{m\omega^2(R^2 - R_0^2)}{T_{eq}(\psi)}\right\} \tag{5.7}$$

Under strong rotation, the centrifugal force tends to push impurities in the outboard region while an induced equilibrium potential $\tilde{\phi}_1$, which varies poloidally, tends to balance the density asymmetry. These effects are enhanced for heavy impurity ions due to both their high-Z and greater mass.

5.2.2 Poloidal asymmetries generated by toroidal rotation

Parallel impurity transport

In the case of high-Z impurities, they are usually placed in the highly collisional regime according to the definition of collisionality. To derive the poloidal variation of the impurity density, first of all, we start from the momentum balance equation in steady state.

$$N_z m_z (\boldsymbol{V}_z \cdot \nabla)\boldsymbol{V}_z + \nabla p_z + \nabla \cdot \pi_z + N_z Ze\nabla\Phi - ZeN_z(\boldsymbol{V}_z \times \boldsymbol{B}) = \boldsymbol{F}_{zi} \tag{5.8}$$

where $\boldsymbol{V}_z$ is the mean flow, π_z is the viscosity tensor and $\boldsymbol{F}_{zi}$ is the frictional force.

In the above equation, the viscosity tensor π_z can often be neglected in a high collisionality limit, and the temperature can be assumed to be a flux function $T(\psi)$ as a consequence of high parallel heat transport. Then, the final expression of parallel impurity dynamic can be written by projecting Eq.(5.8) in the parallel direction :

$$\frac{m_z N_z \omega^2}{2}\nabla_{\parallel} R^2 + N_z Ze\nabla_{\parallel}\Phi + T_z \nabla_{\parallel} N_z = F_{\parallel,zi} \tag{5.9}$$

The first term corresponds to the centrifugal force related to a strong toroidal rotation, the second term is connected to the electrostatic force and the last term is the pressure gradient along the magnetic field. In a rotating plasma, particles are pushed towards the outside due to the centrifugal force and consequently, an additional electric potential is set up to maintain the quasi-neutrality constraint in plasma.

An analytical formula for a non-uniform density distribution can be determined from the parallel impurity transport. The first analytical derivation was done in (Fülöp and Helander, 1999) by including both inertial and frictional terms in Eq.(5.9) for main ions in Banana regime and impurities in Pfirsch-Schlüter regime. Here, we recall the final expression of impurity poloidal asymmetry for the sake of concision. A detailed derivation is also available in Appendix C.

With the following assumptions, such as an axisymmetric magnetic field and a small inverse aspect ratio ($\epsilon \ll 1$), the poloidal asymmetry of impurity density to the lowest order of ϵ can be expressed as $N_z = 1 + N_c \cos\theta + N_s \sin\theta$ where N_s and N_c represents the 'up-down' and 'in-out' asymmetry factors respectively :

$$N_s = 2\epsilon g \frac{1 + (1+\gamma)M_0^2}{1 + (1+\gamma)^2 g^2} \qquad \text{('up-down')} \tag{5.10}$$

$$N_c = 2\epsilon \frac{M_0^2 - (1+\gamma)g^2}{1 + (1+\gamma)^2 g^2} \qquad \text{('in-out')} \tag{5.11}$$

with $M_0^2 = M^2 R_0^2/R^2$. The following dimensionless parameters are defined,

$$M^2 = \frac{m_z \omega^2 R^2}{2T_z}\left(1 - \frac{Zm_i}{m_z}\frac{T_e}{T_e + T_i}\right) \tag{5.12}$$

$$g = -\frac{m_i N_i I}{e\tau_{iz} N_z \langle \boldsymbol{B} \cdot \nabla\theta\rangle}\left(\frac{1}{N_i}\frac{\partial N_i}{\partial\psi} - \frac{1}{2}\frac{1}{T_i}\frac{\partial T_i}{\partial\psi}\right) \tag{5.13}$$

with $\gamma = \frac{eL_\perp \langle B^2\rangle u}{T_i}$ where the poloidal rotation for main ions $u \sim -0.33\frac{If_c}{e\langle B^2\rangle}$ with f_c the fraction of circulating particles.

The first parameter is the modified Mach number, which indicates the impact of toroidal rotation over impurity distribution through M_0^2 in Eq.(5.10, 5.11). The second dimensionless parameter g estimates the steepness of density and temperature gradient profiles for main ions. In the standard neoclassical theory, this parameter is assumed to be small, which corresponds to small frictional force. However, the impact becomes dominant when impurities are localized in the outboard region, especially for high-Z impurities ($g \propto Z^2$) or in the pedestal region.

5.2.3 Neoclassical and turbulent impurity transport in rotating plasma

Turbulent flux

In the case of toroidally rotating plasma, the turbulent flux includes an additional term compared with Eq.(3.10) :

$$\frac{R\Gamma_z}{N_z} = D_z\frac{R}{L_{Nz}} + C_T\frac{R}{L_{Tz}} + C_u u_z' + C_p \tag{5.14}$$

where $u_z' = -R^2\frac{d\omega_z}{dr}\frac{1}{v_{th,z}}$ is the normalized toroidal rotation gradient and the terms in the RHS represent turbulent diffusion, thermo-diffusion, roto-diffusion and curvature pinch respectively .

The first evidence of the roto-diffusion driven by the presence of a radial gradient of the toroidal plasma rotation has been pointed out using a fluid approach (Camenen et al., 2009). Similarly to the mechanisms of momentum pinch (Peeters et al., 2007), the roto-diffusion term is activated by a symmetry breaking mechanism within the toroidal momentum transport. Depending on the direction of the fluctuation propagation, analogously to thermo-diffusion, this term is directed outward (inward) in the case of ITG (TEM) turbulence. The magnitude of the roto-diffusion increases with the ratio of impurity mass to charge, therefore its impact can be significant especially for heavy impurities. It was also shown that the centrifugal effects, associated with toroidal rotation, can have a non-negligible impact on other components (Angioni et al., 2012a), such as thermo-diffusion, curvature pinch, which indicates that the inclusion of toroidal rotation is necessary for the study of impurity transport.

Neoclassical flux

The importance of including poloidal asymmetries in neoclassical impurity transport is now well recognized and experimentally demonstrated. A strong non-uniform distribution in the outboard region can lead to core accumulation (Casson et al., 2015; Angioni et al., 2015). Here, we recall the analytical expression of heavy impurity transport which takes into account such inhomogeneous poloidal density derived in Eq.(4.23).

$$\begin{aligned} R\langle\Gamma_Z^{\text{neo}}\cdot\nabla\psi\rangle_\psi &\propto \left[-\frac{R}{L_{ni}}-\mathrm{H}_{\text{neo}}\frac{R}{L_{Ti}}+\frac{1}{Z}\frac{R}{L_{nz}}\right] \\ &\propto \left[\left(-\frac{R}{L_{ni}}-\mathrm{H}_{\text{sym}}\frac{R}{L_{Ti}}+\frac{1}{Z}\frac{R}{L_{nz}}\right)P_A-0.33P_Bf_c\frac{R}{L_{Ti}}\right] \end{aligned} \tag{5.15}$$

where $H_{\text{neo}} = H_{\text{sym}} + 0.33\frac{P_B}{P_A}f_c$ is the temperature screening coefficient with the factor $H_{\text{sym}} = -\frac{1}{2}$ in the absence of poloidal asymmetries and the geometric factors P_A and P_B (4.24) related to the poloidal asymmetry. A series of recent studies has shed light on the poloidal asymmetry caused by external heating system, such as NBI and ICRH heating, and it was found that both factors P_A and P_B can reach up to 100 in JET tokamak with heating systems. It was also evidenced that enhanced poloidal asymmetry tends to reduce the magnitude of temperature screening coefficient H_{neo} leading to a core accumulation near the magnetic axis (Casson et al., 2020).

5.3 Numerical results

Effects of toroidal rotation on impurity transport can be investigated using the full-F gyrokinetic code GYSELA by means of an additional toroidal momentum source. In general, the centrifugal force driven by toroidal rotation is dominant for heavy impurities, which are often observed to accumulate in the core. Accordingly, tungsten (W) is chosen for our simulations with impurity charge $Z_W = 40$ and mass $A_W = 184$. Impurities are kept in the trace limit ($N_W Z^2 \ll 1$), and thereby their presence does not impact the background turbulence. The initial radial profiles of density and temperature are set to $R/L_{ns} = 2.2$ and $R/L_{Ts} = 6$ for both ions and impurities generating ion temperature gradient (ITG) driven turbulence. According to Eq.(4.19), the main ions are in the Banana regime while tungsten impurities are placed in the collisional Pfirsch-Schlüter regime. Other parameters used for numerical simulations are listed on Table 5.1 as well as the magnetic field profile and security factor.

TABLE 5.1 – Numerical simulations parameters

Parameters	Value
Time step	$\Delta t \omega_{ci} = 16$
Normalized gyroradius	$\rho_* = \rho_i / a = 1/190$
Impurity concentration	$\mathcal{C}_W = 10^{-6}$
Inverse aspect ratio	$\epsilon = a/R_0 = 1/4.4$
Density	$R/L_n = 2.2$
Temperature	$R/L_T = 6$
Magnetic field	$\boldsymbol{B} = \left(\frac{B_0 R_0}{R}\right)\left[\frac{r}{q(r) R_0}\boldsymbol{e}_\theta + \boldsymbol{e}_\varphi\right]$
Safety factor	$q(r) = 1.5 + 1.3 \exp\{[2.5 \log(r/a)]\}$

To save on numerical computation time, each simulation is composed of two different steps : (i) the first stage is only composed of main ions without any momentum source. This part lasts until the background turbulence is sufficiently developed. (ii) In the second step, we inject tungsten impurities with a toroidal momentum source. It should be noted that we apply the momentum source for main ions, so that toroidal rotation is transferred by inter-species collisional effects like it would be in a NBI heating scenario.

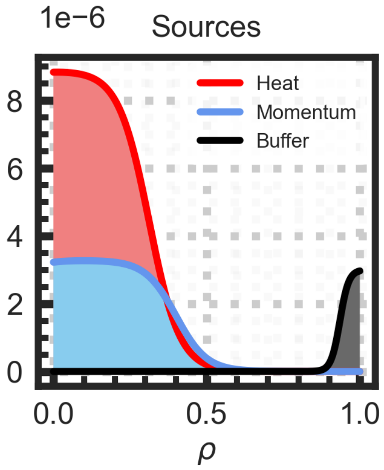

FIGURE 5.1 – Raidal profile of GYSELA sources.

Radial profiles of the applied source terms in GYSELA are displayed in Figure 5.1. The presence of a heat source is inherent to flux driven simulations allowing investigation of different heating power on the energy confinement time. In addition to the heat source, an adjustable momentum source is added to inject toroidal momentum for main ions. It is important to choose an appropriate radial profile for momentum source, since the toroidal velocity saturation time is proportional to ρ_*^{-3}, which makes untractable to get a steady state for our current simulation ($\rho_*^{-1} = 190$). This problem can be overcome by properly choosing the initial toroidal velocity radial profile, similar to the saturated toroidal velocity profile which has already been obtained in (Sarazin et al., 2011).

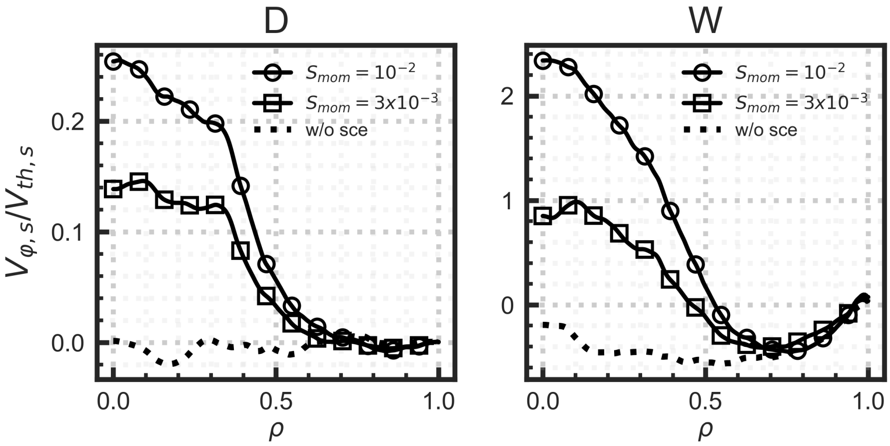

FIGURE 5.2 – Radial toroidal velocity profile averaged over the flux surface for deuterium (D) and tungsten (W) w and w/o momentum source.

Effective injection of toroidal momentum can be verified by comparing radial profiles of toroidal velocity described in Figure 5.2. For deuterium, Mach number $M_s = V_{\varphi,s}/V_{th,s}$ is often found to be small even with additional momentum injection, while it can largely exceed unity for tungsten. Such a high Mach number for tungsten can also be found in experiments. For example, Mach number for deuterium was found to be as high as $M_D \sim 0.7$ in JET operations by means of neutral beam injections (NBI) (de Vries et al., 2008), which indicates that an appropriate treatment of toroidal rotation is necessary for impurity transport modelling.

5.3.1 Enhanced poloidal asymmetry by toroidal rotation

In Figure 5.3, a comparison of poloidally inhomogeneous impurity density $\tilde{N}_W$ obtained from non-linear gyrokinetic simulations are shown for different cases. In the absence of momentum injection (Figure 5.3 left), toroidal velocity of both deuterium and tungsten remains low and the main contribution for poloidal W asymmetry mainly arises from the background turbulence (Donnel et al., 2019c). The effects of centrifugal force become dominant for higher toroidal rotation. For the case with impurity (W) Mach ~ 1, approximately 20% excess (deficit) of W impurities is localized in the outboard (inward) region, and this '*in-out*' asymmetry is found to be amplified for W Mach ~ 2 up to 40%.

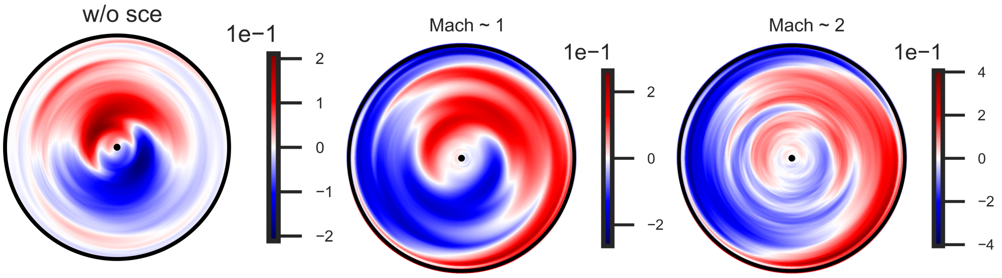

FIGURE 5.3 – Time averaged
2D poloidal section of perturbed W density. (Left) w/o momentum source (center) case with tungsten Mach ~ 1 and (right) case with tungsten Mach ~ 2.

Such enhanced *'in-out'* asymmetry can also be found in the framework of an analytical approach. To this end, the poloidal map of density fluctuations is reconstructed based on two analytical formulas derived in Eq.(5.7), Eq.(5.10, 5.11), and the result extracted from nonlinear GYSELA simulations. The results for the 3 cases are shown respectively from left to right in Figure 5.4. It should be noted that, although there are some discrepancies in terms of amplitudes, the overall *'in-out'* enhanced poloidal asymmetries are found no matter which method of reconstruction is used. Recently, the analytical formula derived from parallel impurity transport in Eq.(5.10, 5.11) has already been compared with experimental data from the C-Mod tokamak, producing results in a qualitative agreement between them (Reinke et al., 2013).

5.3.2 Impurity particle flux

In general, neoclassical impurity transport can be expressed as a function of density, temperature and collisionality : $\Gamma_{neo,W} \propto f(N_i, N_W, T_i, T_W, \nu_z i)$. In contrast to the assumption made by the standard neoclassical theory, a non-uniform distribution of impurity density has to be included for a correct prediction of neoclassical flux. In Figure 5.5, neoclassical W-flux is calculated from a reconstructed density $\tilde{N}_z = \delta \cos\theta + \Delta \sin\theta$, expressed as a function of the δ='in-out' / Δ='up-down' asymmetry parameters respectively. As the case $\delta = \Delta = 0$ represents a uniform impurity

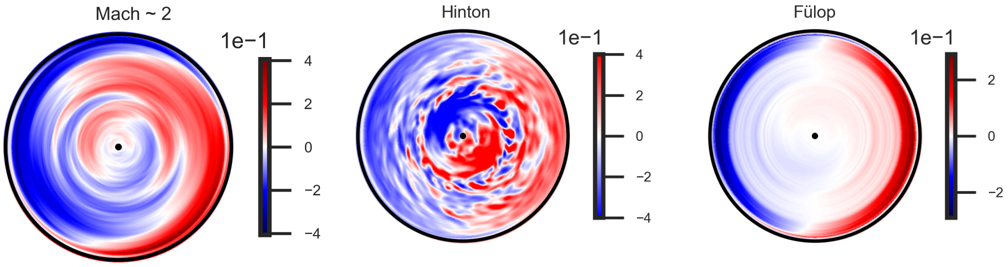

FIGURE 5.4 – (Left) Poloidal asymmetry obtained from nonlinear simulations GYSELA. (Center) Reconstructed impurity density from Eq.(5.7). (Right) Reconstructed impurity density from Eq.(5.10, 5.11).

density, the importance of including poloidal asymmetry can be clearly identified since neoclassical flux is strongly enhanced as δ and Δ increase.

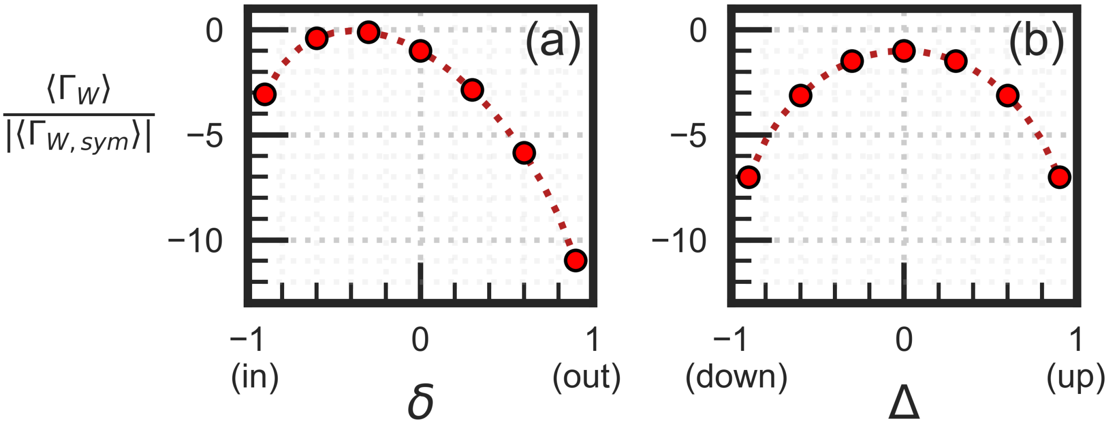

FIGURE 5.5 – Neoclassical W-flux as a function of the δ='in-out', and Δ='up-down' asymmetry parameters. The reconstructed density $\tilde{N}_W = \delta\cos\theta + \Delta\sin\theta$ is used to calculate the neoclassical flux in Eq.(5.15) while other terms, i.e., N_i, T_i, T_W, ν_{zi} are taken from the GYSELA simulations. Flux is normalized to the symmetric case with $\delta = \Delta = 0$.

In line with the previous result, neoclassical and turbulent flux can be directly computed from nonlinear simulations. The following definitions are used for each type of particle transport :

$$< \Gamma_z^{\rm turb} \cdot \nabla\psi >_\psi = \left\langle \int d^3v \bar{F}_z \bar{v}_E^{n\neq 0} \cdot \nabla\psi \right\rangle_\psi \tag{5.16}$$

$$< \Gamma_z^{\rm neo} \cdot \nabla\psi >_\psi = \left\langle \int d^3v \bar{F}_z (v_{D,s} + \bar{v}_E^{n=0}) \cdot \nabla\psi \right\rangle_\psi \tag{5.17}$$

where n is the toroidal mode number.

Consistently with the previous results in Figure 5.4 and 5.5, non-linear simulations with GYSELA reproduce enhanced neoclassical flux as the magnitude of injected momentum source increases, leading to outboard localization of W impurities (Figure 5.6). While strong density inhomogeneity driven by the toroidal rotation has a direct impact on neoclassical transport, turbulent transport is directly linked to the roto-diffusion in Eq.(5.14), which in turn leads to an outward turbulent flux in case of ITG-turbulence. This term, proportional to A/Z where A is the mass number of the impurity, can often match the diffusive part especially in case of heavy impurities (Camenen et al., 2009).

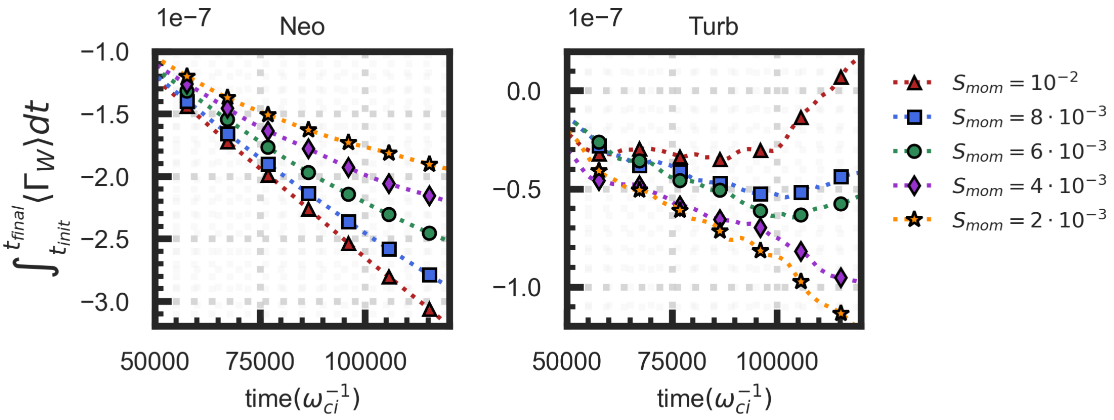

FIGURE 5.6 – W impurity flux averaged over the overall radial position between $\rho = 0.2$ and $\rho = 0.8$ with different magnitudes of the momentum source. (Left) neoclassical flux and (right) turbulent flux.

The central W accumulation in the region between $\rho = 0$ and $\rho = 0.3$ is shown in Figure 5.7 with different Mach numbers. As expected analytically and numerically from the previous cases, a stronger accumulation is found for higher Mach number ($M_W \sim 2$) due to the enhanced poloidal asymmetry by toroidal rotation (Figure 5.3). No significant difference is observed between $t = 0$ and $t = 7 \times 10^4 \omega_{ci} t$, which corresponds to the collisional transfer time of toroidal rotation from deuterium to tungsten. In Chapter 4, the overall W inward flux—mainly from dominant neoclassical flux—has been reported even in the absence of external toroidal rotation. Consistently with those

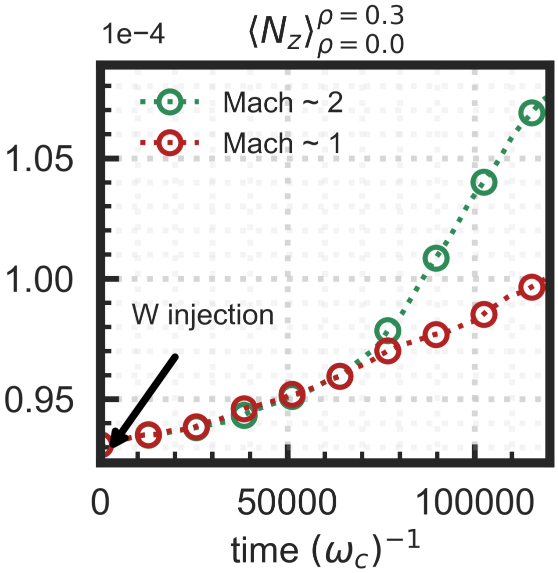

Figure 5.7 – Central W accumulation between $\rho = 0$ and $\rho = 0.3$ is represented for two different Mach numbers (toroidal rotation of the plasma).

results, it is evidenced in Figure 5.7 that a strong toroidal rotation gives rise to an inwardly peaked impurity density profile. Fortunately, it has been reported that a proper use of Ion Cyclotron Resonance Heating (ICRH) / Electron Cyclotron Resonance Heating (ECRH) can be favorable for impurities removal (Dux et al., 2003; Leigheb et al., 2007; Sertoli et al., 2015; Angioni et al., 2017; Shen et al., 2019). ECRH is often considered to be more efficient than ICRH since it causes an increase of heat and main diffusion leading to a flattened main ion density profile, which can reduce neoclassical inward convection.

5.4 Conclusion

In this chapter, we have studied the poloidal asymmetry of impurity density in toroidally rotating plasma and its impact on neoclassical and turbulent transports. For the neoclassical impurity transport, the rotation-induced poloidal asymmetry tends to increase inward impurity particle flux leading to deleterious core W accumulation, while turbulent transport is directed outwards as toroidal rotation increases due to the roto-diffusion term. For our parameters, it was found that the first (neoclassical) effect dominates. Within the framework of non-linear gyrokinetic simulations, numerical results obtained with GYSELA are in qualitative agreement with the analytical description.

The generic inward impurity transport driven by toroidal rotation, mainly from dominant neoclassical transport, is an undesirable result for future fusion scenarios. To avoid this, high power ICRH heating near the magnetic axis has been proposed in order to mitigate W accumulation, since it can reduce impurity density asymmetry but also increase the outward turbulent flux by increasing main ions temperature profile. This aspect will be soon tested within the GYSELA framework using an anisotropic heating source for the main ions.

Chapitre 6

Conclusion

In nuclear fusion, the presence of inevitable impurities is closely related to the operational performance of the fusion reactor. A thorough understanding of impurity transport is, therefore, crucial for the achievement of the project ITER. During a plasma discharge, various impurities can exist at the same time, for instance, Helium (He) ash as a reactant of DT fusion reactions, Argon (Ar) or Nitrogen (N) which can be voluntarily injected to reduce the heat flux loaded on the divertor and heavy impurities like tungsten (W) from the plasma-wall interactions. It is now a well-known fact that a high concentration of heavy (high Z) impurities might lead to complete disruptions of burning plasma by radiating a high fraction of energy, while light (low Z) impurities lead to a dilution of the main DT fuel.

There are three different mechanisms by which impurity transport is generated ; (i) turbulence, (ii) collisional effects, and (iii) MHD instabilities. During this thesis, we restricted ourselves to the electrostatic cases, thereby only the first two main causes are investigated both numerically and theoretically. To this end, two gyrokinetic codes—(i) GYSELA-5D developed in CEA-IRFM and (ii) TERESA-4D developed in IJL—have been used to study impurity transport. Despite the dimensional reduction via gyrokinetic approach from 6D to 5D, a high computational cost of GYSELA precludes a certain type of study, such as the investigation of parametric dependencies. For this reason, the bounce-averaged gyrokinetic code TERESA has been used to complete the studies.

In general, turbulent impurity transport can be separated into two different parts : A *diffusive* part and a *convective* part. For a peaked density profile in tokamaks, the diffusive part always drives outward impurity transport. The convective part, on the other hand, can be directed inward leading to core accumulation according to the nature of the background turbulence and the profile of magnetic curvature. A detailed investigation of the convective part can be fulfilled through the parametric dependencies of each term, such as thermo-diffusion and curvature pinch. For this purpose, the bounce-averaged gyrokinetic code TERESA has been used for this study in case of trapped particle turbulence, and an analytical approach, namely *quasi-linear theory*, has been compared with numerical results giving a qualitatively good agreement between them. It was found that thermo-diffusion is directed inward when trapped electron mode (TEM) turbulence is dominant. In addition to that, a negative sign of curvature pinch has been reproduced by modifying the sign of the precession drift. Although negative magnetic shear could be favorable for the turbulent convective term, low or negative magnetic shear in the core is found to suppress turbulence by triggering transport barriers, which consequently leads to core impurity accumulation due to neoclassical transport.

The overall results obtained using TERESA suggest that, first of all, a proper use of a heating system, such as ICRH, might be useful to induce TEM to ITG turbulence to expel impurities from the core, and also a formation of a negative magnetic shear near the magnetic axis might be beneficial, from the point of view of the turbulent convective term, to prevent impurities from accumulating in the core region. For a more complete and predictive model, however, it would be essential to take into account both neoclassical and turbulent transport effects.

The main transport channel of various impurities differs from species to species according to their mass and charge. For light impurities, such as Helium (He), particles are transported mainly by turbulence while the transport of heavy impurities, such as tungsten (W), are often dominated by neoclassical effects. The full-F gyrokinetic code GYSELA, implemented with a linearized collision operator, allows us to study both turbulent and neoclassical impurity transport in a self-consistent manner. Recently, thanks to the development of diagnostics in tokamaks, poloidal asymmetry of impurity density has renewed interest in impurity transport since it can substantially modify the neoclassical transport. In the absence of external heating systems, poloidal asymmetry is mainly driven by background turbulence and parallel friction. Nonlinear simulations performed in this manuscript have confirmed that GYSELA reproduces a strong turbulent flux for helium while tungsten is primarily dominated by neoclassical flux, which corresponds well to our analytical predictions. Moreover, poloidal asymmetry generated by turbulence was found to be stronger for heavy impurities due to a Boltzmann type response, which leads to a strong modification of the neoclassical transport, especially in the Pfirsch-Schlüter (PS) regime. The overall results agree well with our analytical descriptions, recovering the coefficient of thermal screening factor $H_{\text{GYS}} \sim -0.5$ close to the theoretical prediction except in the region where strong poloidal asymmetries are generated by the turbulence.

Another physical mechanism for poloidally non-uniform impurity density is the toroidal rotation. During tokamak discharge, toroidal rotation can be generated intrinsically or externally by Neutral Beam Injection (NBI) heating. The centrifugal force, in connection with toroidal rotation, pushes heavy impurities toward the wall, generating a strong *'in-out'* poloidal asymmetry. From an analytical standpoint, such enhanced poloidal asymmetry can increase or reduce neoclassical transport by an order of magnitude and even change its direction. Within the framework of nonlinear gyrokinetic simulations, adjustable source terms have been applied to investigate the effects of a strong toroidal rotation. Indeed, nonlinear simulations GYSELA performed with an additional toroidal momentum source showed that, in the case of a strong rotation, the neoclassical flux tends to increase due to an enhanced poloidal asymmetry while turbulent flux is strongly affected by the roto-diffusion, leading to an outward flux in the case of an ion temperature gradient (ITG) turbulence (Figure 6.1). This term becomes dominant, especially for heavy impurities, due to its proportionality to A/Z where A, Z is impurity mass and charge respectively.

In this manuscript, we have studied both turbulent and neoclassical transport in different configurations. The overall results obtained throughout this manuscript imply that heavy impurities are prone to be accumulated in the central region and are very sensitive to external conditions. Fortunately, an additional use of central Ion Cyclotron Resonance Heating (ICRH) / Electron Cyclotron Resonance Heating (ECRH) had shown to avoid impurity accumulation efficiently. Although ICRH can mitigate W core accumulation by reducing the poloidal asymmetry and by increasing the outward turbulent flux, ECRH is often considered to be more efficient since an increased heat and main ion diffusion flatten main ion density profile, which, in turn, strongly reduces neoclassical inward convection for impurities. Applying the additional ICRH / ECRH heating system for impurities in GYSELA remains one of the future works.

Although the current knowledge of impurity transport is comparable to those of ions, there are still a lot of open questions. For instance, in the framework of GYSELA, numerical investigations of the effects of the ICRH heating system, kinetic electrons, and impurity transport in elongated tokamak geometry seem achievable in a foreseeable future, and for instance, the study of impurity transport across a transport barrier (pedestal, steep gradients) is being investigated by means of GYSELA (PhD thesis of G. Lo-Casio). In the long run, an integrated modelling, capable of interpreting experimental observation as well as validating plasma theory against experiments, will be an essential tool of tokamak fusion research. For a current state-of-the-art numerical code, derived from the first principle description, it is out of reach to take into account all the physical processes, such as core transport, edge physics, MHD stability, external heating, and current drive. It is for this reason that a more comprehensive integrated modelling will be key for a reliable prediction of the performance in tokamaks.

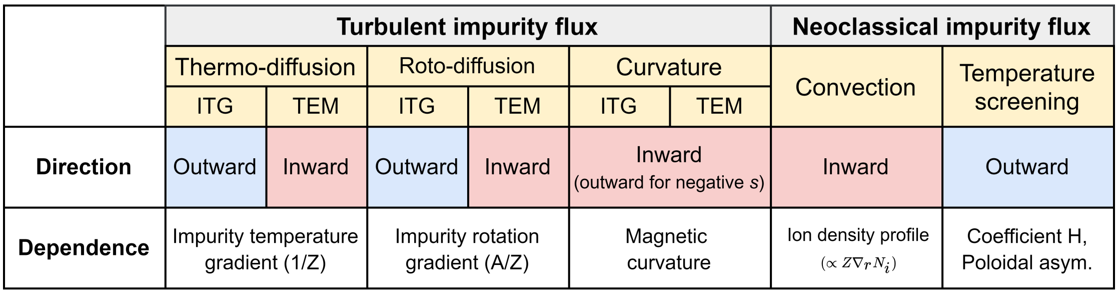

	Turbulent impurity flux						**Neoclassical impurity flux**	
	Thermo-diffusion		Roto-diffusion		Curvature		Convection	Temperature screening
	ITG	TEM	ITG	TEM	ITG	TEM		
Direction	Outward	Inward	Outward	Inward	Inward (outward for negative *s*)		Inward	Outward
Dependence	Impurity temperature gradient (1/Z)		Impurity rotation gradient (A/Z)		Magnetic curvature		Ion density profile ($\propto Z\nabla_r N_i$)	Coefficient H, Poloidal asym.

FIGURE 6.1 – Different directions of convective terms in both turbulent and neoclassical impurity flux.

Annexe A

Quasi-linear impurity transport by fluid approach

In this appendix, the impurity particle flux Γ_Z is derived by a fluid approach of the quasi-linear theory. This approach gives the same results as those presented in Sec.3.2.1 and the presence of diffusive and convective parts are expressed below.
First, the bounce-averaged distribution function F_s satisfies the Vlasov equation Eq.(2.47) :

$$\frac{\partial F_s}{\partial t} - [\mathcal{J}\phi, F_s] + \frac{E\Omega_d}{Z_s}\frac{\partial F_s}{\partial \alpha} = 0 \tag{A.1}$$

The first and second moments of Eq.(A.1) then lead to the time evolution of the density and pressure terms respectively.

$$\frac{\partial N}{\partial t} + \frac{\partial \bar{\phi}}{\partial \psi}\frac{\partial N}{\partial \alpha} - \frac{\partial \bar{\phi}}{\partial \alpha}\frac{\partial N}{\partial \psi} + \frac{3}{2}\frac{\Omega_d}{Z_s}\frac{\partial p}{\partial \alpha} = 0 \tag{A.2}$$

$$\frac{\partial p}{\partial t} + \frac{\partial \bar{\phi}}{\partial \psi}\frac{\partial p}{\partial \alpha} - \frac{\partial \bar{\phi}}{\partial \alpha}\frac{\partial p}{\partial \psi} + \frac{5}{2}\frac{\Omega_d}{Z_s}\frac{\partial}{\partial \alpha}(pT) = 0 \tag{A.3}$$

Here, $\bar{\phi}$ represents the gyro-bounce averaged potential. This notation will be omitted from now for clarity.

Using the linearization in the Fourier space $\tilde{\phi} = \sum_l \phi_l(\psi, t)e^{il\alpha}$ and $\tilde{N}_s = \sum_l N_l(\psi, t)e^{il\alpha}$, Eq.(A.2 A.3) becomes :

$$-i\omega N_l + il\frac{3}{2}\frac{\Omega_d}{Z_s}(T_l N_{eq} + N_l T_{eq}) - il\phi_l\frac{\partial N_{eq}}{\partial \psi} = 0 \tag{A.4}$$

$$(-i\omega T_{eq} + il\frac{5}{2}\frac{\Omega_d}{Z_s}T_{eq}^2)N_l + (-i\omega N_{eq} + il\frac{5\Omega_d}{Z_s}N_{eq}T_{eq})T_l - il\phi_l\frac{\partial p_{eq}}{\partial \psi} = 0 \tag{A.5}$$

where N_{eq}, T_{eq} and p_{eq} are the equilibrium density, temperature and pressure respectively.

After some calculation, Eq.(A.4) and Eq.(A.5) can be rewritten :

$$\begin{aligned} &\frac{2\omega}{3l\Omega_d/Z_s}N_l + \frac{2l}{3\Omega_d/Z_s}\phi_l\frac{\partial N_{eq}}{\partial\psi} = T_l N_{eq} + N_l T_{eq} \\ &(\omega-\omega_T)T_{eq}N_l + l\phi_l\frac{\partial p_{eq}}{\partial\psi} + (\omega-2\omega_T)N_{eq}T_l = 0 \end{aligned} \tag{A.6}$$

Here, we replaced $5l\Omega_d T_{eq}/2Z_s$ by ω_T. By introducing $\kappa_N = -\frac{1}{N_{eq}}\frac{dN_{eq}}{d\psi}$, $\kappa_T = -\frac{1}{T_{eq}}\frac{dT_{eq}}{d\psi}$ the logarithmic density and temperature profile respectively with ψ the dimensionless radial coordinate ($d\psi = -R_0 B_\theta dr$), further arrangement can be recast as :

$$\begin{aligned} &\frac{T_l}{T_{eq}} = \left(\frac{5\omega}{3\omega_T} - 1\right)\frac{N_l}{N_{eq}} + \frac{5l\hat{\phi}}{3\omega_T}\underbrace{\frac{1}{N_{eq}}\frac{\partial N_{eq}}{\partial\psi}}_{\kappa_{n_{eq}}} \\ &(\omega-\omega_T)\frac{N_l}{N_{eq}} + l\phi_l\underbrace{\frac{1}{p_{eq}}\frac{\partial p_{eq}}{\partial\psi}}_{\kappa_{n_{eq}}+\kappa_{T_{eq}}} + (\omega-2\omega_T)\frac{T_l}{T_{eq}} = 0 \end{aligned} \tag{A.7}$$

Combining these equations gives :

$$\left[(\omega-\omega_T)\omega_T + (\omega-2\omega_T)\left(\frac{5\omega}{3}-\omega_T\right)\right]\frac{N_l}{N_{eq}} = \left[(\kappa_{n_{eq}}+\kappa_{T_{eq}})\omega_T + \frac{5}{3}(\omega-2\omega_T)\kappa_{n_{eq}}\right](-l\phi_l) \tag{A.8}$$

Averaging Eq.(A.2) over α gives the impurity particle flux Γ_z according to the continuity equation.

$$\frac{\partial N_s}{\partial t} + \frac{\partial\Gamma_s}{\partial\psi} = \frac{\partial N_s}{\partial t} - \frac{\partial}{\partial\psi}\left\langle\frac{\partial\phi}{\partial\alpha}N_s\right\rangle = 0 \tag{A.9}$$

Now, the particle flux Γ_Z can be written :

$$\Gamma = -\left\langle\frac{\partial\tilde{\phi}}{\partial\alpha}\tilde{N}\right\rangle = -\left\langle\sum_l il\phi e^{il\alpha}\sum_l N_l e^{il\alpha}\right\rangle = i\sum_l lN_l\phi_l^* \tag{A.10}$$

Knowing the relation between the perturbed potential and the density, we insert Eq.(A.8) into Eq.(A.10). After some arrangement, the particle flux in the TERESA model can finally be written as follows :

$$\begin{aligned} \Gamma &= i\sum_l N_{eq}(-l\phi_l)(l\phi_l^*)\frac{(\kappa_{n_{eq}}+\kappa_{T_{eq}})\omega_T + \frac{5}{3}(\omega-2\omega_T)\kappa_{n_{eq}}}{(\omega-\omega_T)\omega_T + (\omega-2\omega_T)(\frac{5}{3}\omega-\omega_T)} \\ &= -i\sum_l\frac{N_{eq}l^2|\phi_l|^2}{(\omega-\omega_T)\omega_T + (\omega-2\omega_T)(\frac{5}{3}\omega-\omega_T)}\left[\frac{1}{3}(5\omega-7\omega_T)\kappa_{nz} + \omega_T\kappa_{Tz} + \frac{5\Omega_d}{2}\frac{\omega-\omega_T}{1+\Omega_d\psi}\right] \end{aligned} \tag{A.11}$$

where we put $N_l = \frac{N_{eq}}{(1+\Omega_d\psi)^{3/2}}$ and $T_l = \frac{T_{eq}}{(1+\Omega_d\psi)}$ for the perturbed density/temperature, so $\kappa_{n_{eq}}, \kappa_{T_{eq}}$ was replaced by $\kappa_{n_{eq}} = \kappa_n + \frac{3\Omega_d}{2(1+\Omega_d\psi)}$ and $\kappa_{T_{eq}} = \kappa_T + \frac{\Omega_d}{(1+\Omega_d\psi)}$. By putting $\omega = \omega_r + i\gamma$ in Eq.(A.11) to take only real part of above equation, and by binding all the terms with respect to κ_n and κ_T separately, the above impurity particle flux Γ_z can be simplified as follows :

$$\frac{\Gamma_z}{N_z} = D_z\kappa_{N_z} + C_T\kappa_{T_z} + C_P \tag{A.12}$$

where the coefficients D_z, C_T and C_P represents impurity turbulent diffusion, thermo-diffusion and curvature pinch respectively.

Annexe B

Perpendicular flux and CGL pressure tensor

The perpendicular part of particle flux consists of three different drift terms :

$$\mathbf{\Gamma}_\perp = N\boldsymbol{v}_\mathrm{E} + N\langle \boldsymbol{v}_\mathrm{D}\rangle - \nabla \times \left[N \left\langle \frac{\mu}{Ze}\boldsymbol{b} \right\rangle \right] \tag{B.1}$$

where the magnetic drift consists of the curvature and ∇B drifts.

$$\boldsymbol{v}_{Ds} = \frac{m_s v_\parallel^2}{ZeB}\mathbf{b} \times \boldsymbol{\kappa} + \frac{\mu}{Ze}\mathbf{b} \times \nabla \ln B \tag{B.2}$$

Here $\boldsymbol{\kappa} = (\mathbf{b}\cdot\nabla)\mathbf{b}$ is the magnetic curvature, which can be expressed otherwise (See Appendix.B.1 hereafter).

$$\boldsymbol{\kappa} = \frac{\nabla_\perp B}{B} + \frac{\mu_0 \nabla \perp P}{B^2} \tag{B.3}$$

Applying an average of the distribution function ($\langle ...\rangle = \frac{1}{N}\int d_3\boldsymbol{v}\bar{F}_z ...$) over Eq.(B.2) leads to :

$$\mathbf{\Gamma}_{\perp\mathrm{D}} = \frac{P_\parallel}{ZeB}\boldsymbol{b} \times \boldsymbol{\kappa} + \frac{P_\perp}{ZeB}\boldsymbol{b} \times \nabla \ln B \tag{B.4}$$

where we used the following relations

$$\begin{aligned} P_\parallel &= \int d^3\boldsymbol{v}\bar{F}mv_\parallel^2 \\ P_\perp &= \int d^3\boldsymbol{v}\bar{F}\mu B \end{aligned} \tag{B.5}$$

$$-\nabla \times \left[N \left\langle \frac{\mu}{Ze}\boldsymbol{b} \right\rangle \right] = \frac{\boldsymbol{B}}{ZeB^2} \times \nabla P_\perp - \frac{P_\perp}{ZeB}\boldsymbol{b} \times \nabla \ln B - \frac{P_\perp}{ZeB}\nabla \times \boldsymbol{b} \tag{B.6}$$

using the following identities $\nabla(AB) = A\nabla B + B\nabla A$ and $\nabla\left(\frac{B}{A}\right) = \frac{A\nabla B - B\nabla A}{A^2}$.

Therefore, Eq.(B.1) can be recast

$$\begin{aligned}\mathbf{\Gamma}_\perp &= N\boldsymbol{v}_\mathrm{E} + (P_\parallel - P_\perp)\frac{1}{ZeB}(\boldsymbol{b}\times\boldsymbol{\kappa}) + \frac{\boldsymbol{B}}{ZeB^2}\times\nabla P_\perp \\ &= N\boldsymbol{v}_\mathrm{E} + \frac{\boldsymbol{B}}{ZeB^2}\times\nabla\cdot\mathbf{\Pi}\end{aligned} \tag{B.7}$$

where we defined

$$\nabla\cdot\mathbf{\Pi} = \nabla P_\perp(P_\parallel - P_\perp)\boldsymbol{\kappa} + \left[(\boldsymbol{B}\cdot\nabla)\left(\frac{P_\parallel - P_\perp)}{B}\right)\right]\boldsymbol{b} \tag{B.8}$$

Then, the radial particle flux can be written as follows :

$$\langle\mathbf{\Gamma}_{\perp z}\cdot\nabla\psi\rangle_\psi = \left\langle\left[\frac{\boldsymbol{B}}{ZeB^2}\times(N_z e\nabla\phi + \nabla\cdot\mathbf{\Pi})\right]\cdot\nabla\psi\right\rangle_\psi \tag{B.9}$$

where the bracket $\langle\ldots\rangle$ corresponds to a flux surface average

$$\langle\mathcal{G}\rangle_\psi = \frac{\int\frac{d\theta d\varphi}{\mathbf{B}\cdot\nabla\theta}\mathcal{G}}{\int\frac{d\theta d\varphi}{\mathbf{B}\cdot\nabla\theta}} \tag{B.10}$$

From the expression of the magnetic field $\boldsymbol{B} = I(\psi)\nabla\varphi + \nabla\varphi\times\nabla\psi$, one can find the useful relationship :

$$\frac{\boldsymbol{B}}{B^2}\times\nabla\psi = \frac{I}{B^2}\boldsymbol{B} - R^2\nabla\varphi \tag{B.11}$$

In steady state ($\partial_t = 0$) and the axisymmetric system ($\partial_\varphi = 0$), Eq.(B.9) can be rewritten

$$\langle\mathbf{\Gamma}_\mathrm{neo}\cdot\nabla\psi\rangle_\psi = -\left\langle\frac{I}{ZeB^2}(N_z e\cdot\nabla\phi + \boldsymbol{B}\cdot\nabla\cdot\mathbf{\Pi})\right\rangle_\psi \tag{B.12}$$

It is still possible to decompose further Eq.(B.12) into 2 parts $\Gamma_\mathrm{neo} = \Gamma_\mathrm{BP} + \Gamma_\mathrm{PS}$ by using the identity (Helander and Sigmar, 2005)

$$\frac{1}{B} = \frac{1}{B} - \frac{B}{\langle B^2\rangle_\psi} + \frac{B}{\langle B^2\rangle_\psi} \tag{B.13}$$

Finally, we obtain the impurity BP, PS flux respectively.

$$\langle\mathbf{\Gamma}_\mathrm{BP}\cdot\nabla\psi\rangle_\psi = -\frac{I}{Ze}\frac{\langle\boldsymbol{B}\cdot\nabla\cdot\mathbf{\Pi}\rangle_\psi}{\langle B^2\rangle_\psi} \tag{B.14}$$

$$\langle\mathbf{\Gamma}_\mathrm{PS}\cdot\nabla\psi\rangle_\psi = -\frac{I}{Ze}\left\langle(Ne\mathbf{b}\cdot\nabla\phi + \mathbf{b}\cdot\nabla\cdot\mathbf{\Pi})\left(\frac{1}{B} - \frac{B}{\langle B^2\rangle_\psi}\right)\right\rangle_\psi \tag{B.15}$$

B.1 Magnetic curvature

The magnetic curvature is defined $\boldsymbol{\kappa} = (\mathbf{b}\cdot\nabla)\mathbf{b}$. By using the vectorial identity $\boldsymbol{A}\times(\nabla\times\boldsymbol{B}) = A\cdot\nabla\boldsymbol{B} - (A\cdot\nabla)\boldsymbol{B}$, we can rewrite the magnetic curvature :

$$\begin{aligned}
\boldsymbol{\kappa} &= (\mathbf{b}\cdot\nabla)\mathbf{b} \\
&= -\mathbf{b}\times(\nabla\times\mathbf{b}) = -\mathbf{b}\times(\nabla\times\boldsymbol{B}/B) \\
&= -\mathbf{b}\times(\nabla(\frac{1}{B})\times\boldsymbol{B}) - \mathbf{b}\times(\nabla\times\boldsymbol{B})/B \\
&= -\mathbf{b}\times(\mathbf{b}\times\nabla\ln B) + \mu_0\boldsymbol{J}\times\boldsymbol{B}/B^2 \\
&= \frac{1}{B}[\nabla - \mathbf{b}(\mathbf{b}\cdot\nabla)]B + \mu_0\boldsymbol{J}\times\boldsymbol{B}/B^2
\end{aligned} \tag{B.16}$$

Defining $\nabla_\perp = \nabla - \mathbf{b}(\mathbf{b}\cdot\nabla) = -\mathbf{b}\times(\mathbf{b}\times\nabla)$ as the gradient perpendicular to $\boldsymbol{B}$, we can then rewrite the above equation as

$$\boldsymbol{\kappa} = \nabla_\perp\ln B + \frac{\mu_0\boldsymbol{J}\times\boldsymbol{B}}{B^2} = \frac{\nabla_\perp B}{B} + \frac{\mu_0\nabla_\perp P}{B^2} \tag{B.17}$$

B.2 Parallel frictional force

In case of heavy impurities in the trace limit, the frictional force $\mathcal{F}_{\parallel zi}$ can be written as a linear function of the parallel velocity $V_{\parallel s}$ and the parallel heat flux $q_{\parallel s}$ (Hirshman and Sigmar, 1981).

$$\mathcal{F}_{\parallel zi} = -N_z m_z \nu_{zi}\Big[V_{\parallel z} - V_{\parallel i} - \frac{3}{5}\frac{1}{1+x_{zi}^2}\frac{q_{\parallel z}}{N_z T_z} + \frac{3}{5}\frac{1}{1+x_{iz}^2}\frac{q_{\parallel i}}{N_i T_i}\Big] \tag{B.18}$$

where $x_{ab} = v_{Tb}/v_{Ta}$
It is worthwhile relating Eq.(4.10) with the frictional force $\mathcal{F}_{\parallel zi}$ in order to show how the poloidal density asymmetry is linked to the impurity flux (For more complete derivation, see Appendix of Donnel et al. (2019a)).

$$\mathcal{F}_{\parallel zi} = m_z\nu_{zi}\left[-N_z\frac{T_i}{eB}\frac{I}{L_\psi} + B(N_z u - K_z)\right] \tag{B.19}$$

where $1/L_\psi = 1/L_{\psi,i} + 1/L_{\psi,z}$ with $1/L_{\psi,i} = \partial_\psi\ln P_i - \frac{3}{2}\partial_\psi\ln T_i$ and $1/L_{\psi,z} = -\frac{1}{T_i Z N_z}\partial_\psi P_{\perp z}$ and u is the value related to the poloidal velocity of the main ions.

Annexe C

Impurity density distribution from the parallel dynamics

In the case of the large aspect ratio ($\epsilon \ll 1$) and for a circular cross section, the magnetic field b [9], the impurity density n and the Mach number M can be expanded in ϵ :

$$b^2 = 1 - 2\epsilon\cos\theta + \mathcal{O}(\epsilon^2) \tag{C.1}$$

$$N = 1 + N_c\cos\theta + N_s\sin\theta + \mathcal{O}(\epsilon^2) \tag{C.2}$$

$$M^2 = M_0^2(1 + 2\epsilon\cos\theta) + \mathcal{O}(\epsilon^2) \tag{C.3}$$

By using the quasi-neutrality constraint and the modified Mach number Eq.(5.12), the initial parallel impurity transport Eq.(5.9) can be expressed as (Fülöp and Helander, 1999) :

$$(1 + \alpha N)\frac{\partial N}{\partial \vartheta} = \mathrm{g}(n - b^2 + \gamma(N - \langle nb^2\rangle)b^2) + N\frac{\partial M^2}{\partial \vartheta} - \left\langle N\frac{\partial M^2}{\partial \vartheta}\right\rangle b^2 \tag{C.4}$$

where we introduced $\alpha = \frac{\langle N_z\rangle Z^2 T_0}{2N_0 T_i}$ with $2N_0/T_0 = N_{e0}/T_e + N_{i0}/T_i$

In order to find the expression for *'up-down'* and *'in-out'* asymmetric parameters derived in Eq.(5.10, 5.11), we insert Eq.(C.1 C.2 C.3) into Eq.(C.4), which writes :

$$\cos\theta\Big(gN_c(1+\gamma) - N_s(1+\alpha) + 2\mathrm{g}\epsilon\Big) + \sin\theta\Big(gN_s(1+\gamma) + N_c(1+\alpha) - 2\epsilon M_0^2\Big) = 0 \tag{C.5}$$

where we have neglected all the higher order terms $\epsilon^2, n_c\epsilon, n_s\epsilon \sim \mathcal{O}(\epsilon^2)$.

---

[9] The normalized magnetic field $b = 1/(1 - \epsilon\cos\theta)$

This last equation should be satisfied with all the different angles θ, therefore each coefficient of $\cos\theta$ and $\sin\theta$ should be equal to zero.

$$gN_c(1+\gamma) - N_s(1+\alpha) + 2\mathrm{g}\epsilon = 0 \tag{C.6}$$

$$gN_s(1+\gamma) + N_c(1+\alpha) - 2\epsilon M_0^2 = 0 \tag{C.7}$$

By arranging both Eq.(C.6, C.7), we can finally obtain the *'up-down'* asymmetry term N_s and *'in-out'* asymmetry term N_c

$$N_c = 2\epsilon\frac{(1+\alpha)M_0^2 - (1+\gamma)g^2}{(1+\alpha)^2 + (1+\gamma)^2 g^2} \qquad \text{('in-out')} \tag{C.8}$$

$$N_s = 2\epsilon\mathrm{g}\frac{(1+\alpha) + (1+\gamma)M_0^2}{(1+\alpha)^2 + (1+\gamma)^2 g^2} \qquad \text{('up-down')} \tag{C.9}$$

In the trace limit of impurities ($N_z Z^2 \ll 1$), these equations can be further simplified since $\alpha \ll 1$:

$$N_c = 2\epsilon\frac{M_0^2 - (1+\gamma)g^2}{1 + (1+\gamma)^2 g^2} \qquad \text{('in-out')} \tag{C.10}$$

$$N_s = 2\epsilon\mathrm{g}\frac{1 + (1+\gamma)M_0^2}{1 + (1+\gamma)^2 g^2} \qquad \text{('up-down')} \tag{C.11}$$

Note that the toroidal rotation causes the impurities to accumulate on the outside of the flux surface, which will enhances the neoclassical impurity transport.

Bibliographie

Abel, I. G. et al. (2008). Linearized model Fokker–Planck collision operators for gyrokinetic simulations. I. Theory. *Phys. Plasmas*, **15** 122509.

Angioni, C. et al. (2007). Particle and impurity transport in the Axial Symmetric Divertor Experiment Upgrade and the Joint European Torus, experimental observations and theoretical understanding. *Phys. Plasmas*, **14** 055905.

Angioni, C. et al. (2012a). Analytic formulae for centrifugal effects on turbulent transport of trace impurities in tokamak plasmas. *Phys. Plasmas*, **19** 122311.

Angioni, C. et al. (2012b). Off-diagonal particle and toroidal momentum transport : a survey of experimental, theoretical and modelling aspects. *Nucl. Fusion*, **52** 114003.

Angioni, C. et al. (2014). Tungsten transport in JET H-mode plasmas in hybrid scenario, experimental observations and modelling. *Nucl. Fusion*, **54** 083028.

Angioni, C. et al. (2015). The impact of poloidal asymmetries on tungsten transport in the core of JET H-mode plasmas. *Phys. Plasmas*, **22** 055902.

Angioni, C. et al. (2017). A comparison of the impact of central ECRH and central ICRH on the tungsten behaviour in ASDEX upgrade H-mode plasmas. *Nucl. Fusion*, **57** 056015.

Angioni, C. and Helander, P. (2014). Neoclassical transport of heavy impurities with poloidally asymmetric density distribution in tokamaks. *Plasma Phys. Control. Fusion*, **56** 124001.

Angioni, C. and Peeters, A. (2006). Direction of impurity pinch and auxiliary heating in tokamak plasmas. *Phys. Rev. Lett.*, **96** 095003.

Belli, E. A. et al. (2012). Full linearized Fokker–Planck collisions in neoclassical transport simulations. *Plasma Phys. Control. Fusion*, **54** 015015.

Belli, E. A. et al. (2014). Pfirsch–Schlüter neoclassical heavy impurity transport in a rotating plasma. *Plasma Phys. Control. Fusion*, **56** 124002.

Bilato, R. et al. (2017). The impact of the ion-cyclotron-resonance location on the poloidal asymmetries of impurity density in an ICRF-heated rotating plasma. *Nucl. Fusion*, **57** 056020.

Bonanomi, N. et al. (2018). Light impurity transport in JET ILW L-mode plasmas. *Nucl. Fusion*, **58** 036009.

Bourdelle, C. et al. (2007). A new gyrokinetic quasilinear transport model applied to particle transport in tokamak plasmas. *Phys. Plasmas*, **14** 112501.

Braginskii, S. I. (1965). Transport processes in a plasma. *Reviews of Plasma Physics*, **1** 205.

Brizard, A. and Hahm, T. S. (2007). Foundations of nonlinear gyrokinetic theory. *Rev. Mod. Phys.*, **79** 421.

Camenen, Y. et al. (2009). Impact of the background toroidal rotation on particle and heat turbulent transport in tokamak plasmas. *Phys. Plasmas*, **16** 012503.

Cartier-Michaud, T. et al. (2014). Staircase temperature profiles and plasma transport self-organisation in a minimum kinetic model of turbulence based on the trapped ion mode instability. *J. Phys. : Conf. Ser.*, **561** 012003.

Casson, F. J. et al. (2015). Theoretical description of heavy impurity transport and its application to the modelling of tungsten in JET and ASDEX upgrade. *Plasma Phys. Control. Fusion*, **57** 014031.

Casson, F. J. et al. (2020). Predictive multi-channel flux-driven modelling to optimise ICRH tungsten control and fusion performance in JET. *Nucl. Fusion*, **60** 066209.

Chew, G. F. et al. (1956). The boltzmann equation and the one-fluid hydromagnetic equations in the absence of particle collisions. *Proc. Roy. Soc. A*, **236** 112.

Connor, J. W. (1973). The neo-classical transport theory of a plasma with multiple ion species. *Plasma Phys.*, **15** 765.

de Vries, P. C. et al. (2008). Scaling of rotation and momentum confinement in JET plasmas. *Nucl. Fusion*, **48** 065006.

de Vries, P. C. et al. (2014). The influence of an ITER-like wall on disruptions at JET. *Phys. Plasmas*, **21** 056101.

Del Sarto, D. and Ghizzo, A. (2017). A Hasegawa–Wakatani and modified Hasegawa–Wakatani turbulence induced by Ion Temperature Gradient instabilities. *Fluids*, **2** 65.

Depret, G. et al. (2000). Trapped-ion driven turbulence in tokamak plasmas. *Plasma Phys. Control. Fusion*, **42** 949.

Donnel, P. et al. (2019a). A multi-species collisional operator for full-F global gyrokinetics codes : Numerical aspects and verification with the GYSELA code. *Comp. Phys. Comm.*, **234** 1.

Donnel, P. et al. (2019b). Neoclassical impurity flux in presence of turbulent generated poloidal asymmetries and pressure anisotropy. *Plasma Phys. Control. Fusion*, **61** 044006.

Donnel, P. et al. (2019c). Turbulent generation of poloidal asymmetries of the electric potential in a tokamak. *Plasma Phys. Control. Fusion*, **61** 044006.

Drouot, T. (2015). *Étude de la turbulence liée aux particules piégées dans les plasmas de fusion*. PhD thesis, Université de Lorraine.

Drouot, T. et al. (2014). A gyro-kinetic model for trapped electron and ion modes. *Eur. Phys. J. D*, **68** 280.

Dubuit, N. et al. (2007). Fluid simulations of turbulent impurity transport. *Phys. Plasmas*, **14** 042301.

Dux, R. et al. (2003). Influence of the heating profile on impurity transport in ASDEX upgrade. *Plasma Phys. Control. Fusion*, **45** 1815.

Estrada-Mila, C. et al. (2005). Gyrokinetic simulations of ion and impurity transport. *Phys. Plasmas*, **12** 022305.

Estève, D. et al. (2018). Self-consistent gyrokinetic modeling of neoclassical and turbulent impurity transport. *Nucl. Fusion*, **58** 036013.

Frojdh, M. et al. (1992). Impurity effects on η_i mode stability and transport. *Nucl. Fusion*, **32** 419.

Fussmann, G. et al. (1991). Impurity transport and neoclassical predictions. *Plasma Phys. Control. Fusion*, **33** 1677.

Futatani, S. et al. (2010). Reversal of impurity pinch velocity in tokamaks plasma with a reversed magnetic shear configuration. *Phys. Rev. Lett.*, **104** 015003.

Fülöp, T. et al. (2010). Impurity transport driven by ion temperature gradient turbulence in tokamak plasmas. *Phys. Plasmas*, **17** 062501.

Fülöp, T. and Helander, P. (1999). Nonlinear neoclassical transport in a rotating impure plasma with large gradients. *Phys. Plasmas*, **6** 3066.

Fülöp, T. and Moradi, S. (2012). Effect of poloidal asymmetry on the impurity density profile in tokamak plasmas. *Phys. Plasmas*, **18** 030703.

Fülöp, T. and Mordai, S. (2006). Effect of poloidal asymmetry on the impurity density profile in tokamak plasmas. *Phys. Plasmas*, **18** 030703.

Fülöp, T. and Weiland, J. (2006). Impurity transport in ITER-like plasmas. *Phys. Plasmas*, **13** 112504.

Galeev, A. A. and Sagdeev, R. Z. (1968). Transport phenomena in a collisionless plasma in a toroidai magnetic system. *Soviet Phys. JETP*, **26** 233.

Garbet, X. et al. (2004). Physics of transport in tokamaks. *Plasma Phys. Control. Fusion*, **46** B557.

Garbet, X. et al. (2010). Gyrokinetic simulations of turbulent transport. *Nucl. Fusion*, **50** 043002.

Giroud, C. et al. (2013). Impact of nitrogen seeding on confinement and power load control of a high-triangularity JET ELMy H-mode plasma with a metal wall. *Nucl. Fusion*, **53** 113025.

Goldstein, H. (1980). *Classical mechanics, 2nd. ed.* Addison-Wesley.

Goniche, M. et al. (2017). Ion cyclotron resonance heating for tungsten control in various JET H-mode scenarios. *Plasma Phys. Control. Fusion*, **59** 055001.

Grandgirard, V. (2016). The GYSELA project : A semi-lagrangian code addressing gyrokinetic full-F global simulations of flux driven tokamak plasmas. HDR thesis, Université de Strasbourg.

Grandgirard, V. et al. (2016). A 5d gyrokinetic full-F global semi-lagrangian code for flux-driven ion turbulence simulations. *Comp. Phys. Comm.*, **207** 35.

Gravier, E. et al. (2019). Diffusive impurity transport driven by trapped particle turbulence in tokamak plasmas. *Phys. Plasmas*, **26** 082306.

Guillevic, A. et al. (in prep.). Particle dynamics in a turbulent electric field.

Guirlet, R. et al. (2006). Parametric dependences of impurity transport in tokamaks. *Plasma Phys. Control. Fusion*, **48** B63.

Hazeltine, R. D. and Meiss, J. D. (2013). *Plasma Confinement.* Courier Corporation.

Hein, T. and Angioni, C. (2010). Electromagnetic effects on trace impurity transport in tokamak plasmas. *Phys. Plasmas*, **17** 012307.

Helander, P. (1998). Neoclassical transport in a rotating impure plasma. *Phys. Plasmas*, **5** 1209.

Helander, P. and Sigmar, D. J. (2005). *Collisional Transport in Magnetized Plasmas*. Cambridge : Cambridge University Press.

Hinton, F. L. and Wong, K. (1985). Neoclassical ion transport in rotating axisymmetric plasmas. *Phys. Plasmas*, **28** 3082.

Hinton, T. L. and Hazeltine, R. D. (1976). Theory of plasma transport in toroidal confinement systems. *Rev. Mod. Phys.*, **48** 239.

Hirshman, S. P. and Sigmar, D. J. (1981). Neoclassical transport of impurities in tokamak plasmas. *Nucl. Fusion*, **21** 1079.

Houlberg, W. A. et al. (1997). Bootstrap current and neoclassical transport in tokamaks of arbitrary collisionality and aspect ratio. *Phys. Plasmas*, **4** 3230.

Ida, K. et al. (1989). Impurity behaviour in PBX L- and H-mode plasmas. *Nucl. Fusion*, **29** 231.

Idouakass, M. et al. (2018). Impurity density gradient influence on trapped particle modes. *Phys. Plasmas*, **25** 062307.

Ingesson, L. C. et al. (2000). Comparison of basis functions in soft x-ray tomography and observation of poloidal asymmetries in impurity density. *Plasma Phys. Control. Fusion*, **42** 161.

IPCC (2007). Working group 1 : The physical science basis. *Intergovernmental Panel on Climate Change*, **4** 15.

ITER Physics Expert Group, C. et al. (1999). Chapter 2 : Plasma confinement and transport. *Nucl. Fusion*, **39** 2175.

Joffrin, E. et al. (2019). Overview of the JET preparation for deuterium–tritium operation with the ITER like-wall. *Nucl. Fusion*, **59** 112021.

Kadomtsev, B. B. and Pogutse, O. P. (1970). *Reviews of Plasma Physics : Turbulence in Toroidal Systems*, volume **5** p.249. Springer, Boston, MA.

Kallenbach, A. et al. (2013). Impurity seeding for tokamak power exhaust : from present devices via ITER to DEMO. *Plasma Phys. Control. Fusion*, **55** 124041.

Kappatou, A. et al. (2019). Understanding helium transport : experimental and theoretical investigations of low-Z impurity transport at ASDEX upgrade. *Nucl. Fusion*, **59** 056014.

Kazakov, Y. O. et al. (2012). Poloidal asymmetries due to ion cyclotron resonance heating. *Plasma Phys. Control. Fusion*, **54** 105010.

Komm, M. et al. (2019). Divertor impurity seeding experiments at the compass tokamak. *Nucl. Fusion*, **59** 106035.

Kubo, R. (1963). Stochastic Liouville equations. *J. Math. Phys.*, **4** 174.

Lee, W. W. (1983). Gyrokinetic approach in particle simulation. *Phys. Fluids*, **26** 556.

Leigheb, M. et al. (2007). Molybdenum transport in high density FTU plasmas with strong radio frequency electron heating. *Plasma Phys. Control. Fusion*, **49** 1897.

Lerche, E. et al. (2016). Optimization of ICRH for core impurity control in JET-ILW. *Nucl. Fusion*, **56** 036022.

Lesur, M. et al. (2020). Validity limits of the passive treatment of impurities in gyrokinetic tokamak simulations. *Nucl. Fusion*, **60** 036016.

Lim, K. et al. (2020). Impurity pinch generated by trapped particle driven turbulence. *Plasma Phys. Control. Fusion*, **62** 095018.

Lim, K. et al. (2021). Gyrokinetic modelling of light to heavy impurity transport in tokamaks. *Nucl. Fusion*, **61** 046037.

Lin, Z. et al. (1999). Effects of collisional zonal flow damping on turbulent transport. *Phys. Rev. Lett.*, **83** 3645.

Loarte, A. et al. (2015). Tungsten impurity transport experiments in alcator c-mod to address high priority research and development for iter. *Phys. Plasmas*, **22** 056117.

Maget, P. et al. (2020). Natural poloidal asymmetry and neoclassical transport of impurities in tokamak plasmas. *Plasma Phys. Control. Fusion*, **62** 025001.

Manas, P. et al. (2015). Enhanced stabilisation of trapped electron modes by collisional energy scattering in tokamaks. *Phys. Plasmas*, **22** 062302.

Manas, P. et al. (2020). Light impurity transport in tokamaks : on the impact of neutral beam fast ions. *Nucl. Fusion*, **60** 056005.

Medina, J. et al. (2018). Radial density and heat fluxes description in the velocity space : Nonlinear simulations and quasi-linear calculations. *Phys. Plasmas*, **25** 122304.

Meyer, H. et al. (2019). Overview of physics studies on asdex upgrade. *Nucl. Fusion*, **59** 112014.

Mollen, A. et al. (2012). Effect of poloidal asymmetries on impurity peaking in tokamaks. *Phys. Plasmas*, **19** 052307.

Mollen, A. et al. (2013). Impurity transport in trapped electron mode driven turbulence. *Phys. Plasmas*, **20** 032310.

Moradi, S. et al. (2012). Impurity transport due to electromagnetic drift wave turbulence. *Phys. Plasmas*, **19** 032301.

Noether, E. (1971). Invariant variation problems. *Transport Theory and Statistical Physics*, **1**, 186-207.

Nordman, H. et al. (2008). Influence of the radio frequency ponderomotive force on anomalous impurity transport in tokamaks. *Phys. Plasmas*, **15** 042316.

Odstrcil, T. et al. (2016). Optimized tomography methods for plasma emissivity reconstruction at the ASDEX Upgrade tokamak. *Rev. Sci. Inst.*, **87** 123505.

Park, H. K. et al. (2019). Overview of KSTAR research progress and future plans toward ITER and K-DEMO. *Nucl. Fusion*, **59** 112020.

Pasini, D. et al. (1992). Measurements of impurity transport in JET. *Plasma Phys. Control. Fusion*, **34** 677.

Peeters, A. G. et al. (2007). Toroidal momentum pinch velocity due to the coriolis drift effect on small scale instabilities in a toroidal plasma. *Phys. Rev. Lett.*, **98** 265003.

Pusztai, I. et al. (2013). Turbulent transport of impurities and their effect on energy confinement. *Plasma Phys. Control. Fusion*, **55** 074012.

Pütterich, T. et al. (2010). Calculation and experimental test of the cooling factor of tungsten. *Nucl. Fusion*, **50** 025012.

Pütterich, T. et al. (2013). Observations on the W-transport in the core plasma of JET and ASDEX upgrade. *Plasma Phys. Control. Fusion*, **55** 124036.

Ran, L. B. et al. (1989). Impurity accumulation in plasma regimes with high energy confinement. *J. Nucl. Mat.*, **162-4** 14.

Reinke, M. L. et al. (2012). Poloidal variation of high-Z impurity density due to hydrogen minority ion cyclotron resonance heating on Alcator C-mod. *Plasma Phys. Control. Fusion*, **54** 045004.

Reinke, M. L. et al. (2013). Parallel transport studies of high-Z impurities in the core of Alcator C-Mod plasmas. *Phys. Plasmas*, **20** 056109.

Rice, J. E. et al. (2000). Impurity toroidal rotation and transport in Alcator C-mod ohmic high confinement mode plasmas. *Phys. Plasmas*, **7** 1825.

Romanelli, M. and Ottaviani, M. (1998). Effects of density asymmetries on heavy impurity transport in a rotating tokamak plasma. *Plasma Phys. Control. Fusion*, **40** 1767.

Rutherford, P. H. (1973). Impurity transport in the Pfirsch-Schlüter regime. *Plasma Phys.*, **15** 765.

Sarazin, Y. et al. (2005). Kinetic features of interchange turbulence. *Plasma Phys. Control. Fusion*, **47** 1817.

Sarazin, Y. et al. (2011). Predictions on heat transport and plasma rotation from global gyrokinetic simulations. *Nucl. Fusion*, **51** 103023.

Schweinzer, J. et al. (2011). Confinement of 'improved H-modes' in the all-tungsten ASDEX Upgrade with nitrogen seeding. *Nucl. Fusion*, **51** 113003.

Sertoli, M. et al. (2015). Modification of impurity transport in the presence of saturated (m,n) = (1,1) MHD activity at ASDEX upgrade. *Plasma Phys. Control. Fusion*, **57** 075004.

Shen, Y. et al. (2019). Suppression of molybdenum impurity accumulation in the core using on-axis electron cyclotron resonance heating in EAST. *Phys. Plasmas*, **26** 032507.

Skyman, A. et al. (2014). Effects of the equilibrium model on impurity transport in tokamaks. *Nucl. Fusion*, **54** 013009.

Sonnendrücker, E. et al. (1999). The Semi-Lagrangian method for the numerical resolution of the Vlasov equation. *J. Comput. Phys.*, **149** 201.

Tanabe, T. (2017). *Tritium : Fuel of Fusion Reactors*. Springer Japan.

Terry, J. L. et al. (1978). Observation of poloidal asymmetry in impurity-ion emission due to ∇B drifts. *Phys. Rev. Lett.*, **40** 350.

Tokar, M. Z. et al. (1997). Nature of high-Z impurity accumulation in tokamaks. *Nucl. Fusion*, **37** 1691.

Vernay, T. et al. (2012). Synergy between ion temperature gradient turbulence and neoclassical processes in global gyrokinetic particle-in-cell simulations. *Phys. Plasmas*, **19** 042310.

Weiland, J. et al. (1989). Diffusive particle and heat pinch effects in toroidal plasmas. *Nucl. Fusion*, **29** 1810.

Wesson, J. A. (1997). Poloidal distribution of impurities in a rotating tokamak plasma. *Nucl. Fusion*, **37** 577.

Wong, S. (1987). Transport of impure plasma with arbitrary toroidal rotation. *Phys. Fluids*, **30** 818.

Xu, G. S. et al. (2020). Divertor impurity seeding with a new feedback control scheme for maintaining good core confinement in grassy-ELM H-mode regime with tungsten monoblock divertor in EAST. *Nucl. Fusion*, **60** 086001.

Résumé

Dans un plasma de fusion, la présence d'impuretés est inévitable. Une compréhension fine du transport des impuretés s'avère être cruciale dans le cadre du projet ITER. Dans ce travail, deux codes gyrocinétiques - GYSELA-5D et TERESA-4D - ont été utilisés pour étudier le transport des impuretés. Les transports turbulent et néoclassique ont été pris en compte, permettant de mettre en évidence les vitesses de pincement des impuretés dues aux particules piégées, l'influence de la masse des impuretés sur l'asymétrie poloïdale de leur densité, et l'incidence de cette asymétrie sur le transport, et enfin les effets de la rotation toroïdale du plasma sur le transport des impuretés. Les résultats obtenus grâce à des simulations gyrocinétiques non-linéaires indiquent que les impuretés lourdes ont tendance à s'accumuler dans la région centrale, mais cette tendance peut-être inversée grâce au chauffage externe.

Mots-clés: Fusion, Transport d'impuretés, Gyrocinétique, Transport turbulent, Transport néoclassique.

Abstract

In a fusion plasma, the presence of impurities is inevitable. A thorough understanding of impurity transport is crucial for the achievement of the project ITER. In this work two gyrokinetic codes—GYSELA-5D and TERESA-4D—have been used to study impurity transport. Both turbulent and neoclassical impurity transport have been considered to address impurity pinch caused by trapped particle driven turbulence, as well as the transport of light to heavy impurities and the impact of the poloidal asymmetry of the impurity density on neoclassical transport, and finally the effects of a toroidal rotation on impurity transport. The overall results obtained from nonlinear gyrokinetic simulations imply that heavy impurities tend to be accumulated in the core plasma. However, this accumulation should be avoided by using external heating of the plasma.

Keywords: Fusion, Impurity transport, Gyrokinetics, Turbulent transport, Neoclassical transport.